

This is a repository copy of *Heusler alloys for spintronic devices: review on recent development and future perspectives*.

White Rose Research Online URL for this paper:

<https://eprints.whiterose.ac.uk/163876/>

Version: Published Version

---

**Article:**

Elphick, Kelvin, Frost, William James orcid.org/0000-0001-5249-1006, Samiepour, Marjan et al. (4 more authors) (2021) Heusler alloys for spintronic devices: review on recent development and future perspectives. *Science and Technology of Advanced Materials*. pp. 235-271. ISSN 1468-6996

<https://doi.org/10.1080/14686996.2020.1812364>

---

**Reuse**

This article is distributed under the terms of the Creative Commons Attribution (CC BY) licence. This licence allows you to distribute, remix, tweak, and build upon the work, even commercially, as long as you credit the authors for the original work. More information and the full terms of the licence here:

<https://creativecommons.org/licenses/>

**Takedown**

If you consider content in White Rose Research Online to be in breach of UK law, please notify us by emailing [eprints@whiterose.ac.uk](mailto:eprints@whiterose.ac.uk) including the URL of the record and the reason for the withdrawal request.



## Heusler alloys for spintronic devices: review on recent development and future perspectives

Kelvin Elphick, William Frost, Marjan Samiepour, Takahide Kubota, Koki Takanashi, Hiroaki Sukegawa, Seiji Mitani & Atsufumi Hirohata

To cite this article: Kelvin Elphick, William Frost, Marjan Samiepour, Takahide Kubota, Koki Takanashi, Hiroaki Sukegawa, Seiji Mitani & Atsufumi Hirohata (2021) Heusler alloys for spintronic devices: review on recent development and future perspectives, Science and Technology of Advanced Materials, 22:1, 235-271, DOI: [10.1080/14686996.2020.1812364](https://doi.org/10.1080/14686996.2020.1812364)

To link to this article: <https://doi.org/10.1080/14686996.2020.1812364>



© 2021 The Author(s). Published by National Institute for Materials Science in partnership with Taylor & Francis Group.



Published online: 29 Mar 2021.



Submit your article to this journal [↗](#)



Article views: 2140




View related articles [↗](#)



View Crossmark data [↗](#)

# Heusler alloys for spintronic devices: review on recent development and future perspectives

Kelvin Elphick<sup>a</sup>, William Frost<sup>a</sup>, Marjan Samiepour<sup>a,b</sup>, Takahide Kubota<sup>c,d</sup>, Koki Takanashi<sup>c,d,e</sup>, Hiroaki Sukegawa<sup>f</sup>, Seiji Mitani<sup>f,g</sup> and Atsufumi Hirohata<sup>g</sup> 

<sup>a</sup>Department of Electronic Engineering, University of York, York, UK;

<sup>b</sup>Seagate Technology, 1 Disc Drive, Springtown Industrial Estate, Londonderry, Northern Ireland;

<sup>c</sup>Institute for Materials Research, Tohoku University, Sendai, Japan;

<sup>d</sup>Center for Spintronics Research Network, Tohoku University, Sendai, Japan;

<sup>e</sup>Center for Science and Innovation in Spintronics, Core Research Cluster, Tohoku University, Sendai, Japan;

<sup>f</sup>Research Center for Magnetic and Spintronic Materials, National Institute for Materials Science, Tsukuba, Japan;

<sup>g</sup>Graduate School of Pure and Applied Sciences, University of Tsukuba, Tsukuba, Japan

## ABSTRACT

Heusler alloys are theoretically predicted to become half-metals at room temperature (RT). The advantages of using these alloys are good lattice matching with major substrates, high Curie temperature above RT and intermetallic controllability for spin density of states at the Fermi energy level. The alloys are categorised into half- and full-Heusler alloys depending upon the crystalline structures, each being discussed both experimentally and theoretically. Fundamental properties of ferromagnetic Heusler alloys are described. Both structural and magnetic characterisations on an atomic scale are typically carried out in order to prove the half-metallicity at RT. Atomic ordering in the films is directly observed by X-ray diffraction and is also indirectly probed via the temperature dependence of electrical resistivity. Element specific magnetic moments and spin polarisation of the Heusler alloy films are directly measured using X-ray magnetic circular dichroism and Andreev reflection, respectively. By employing these ferromagnetic alloy films in a spintronic device, efficient spin injection into a non-magnetic material and large magnetoresistance are also discussed. Fundamental properties of antiferromagnetic Heusler alloys are then described. Both structural and magnetic characterisations on an atomic scale are shown. Atomic ordering in the Heusler alloy films is indirectly measured by the temperature dependence of electrical resistivity. Antiferromagnetic configurations are directly imaged by X-ray magnetic linear dichroism and polarised neutron reflection. The applications of the antiferromagnetic Heusler alloy films are also explained. The other non-magnetic Heusler alloys are listed. A brief summary is provided at the end of this review.

## ARTICLE HISTORY

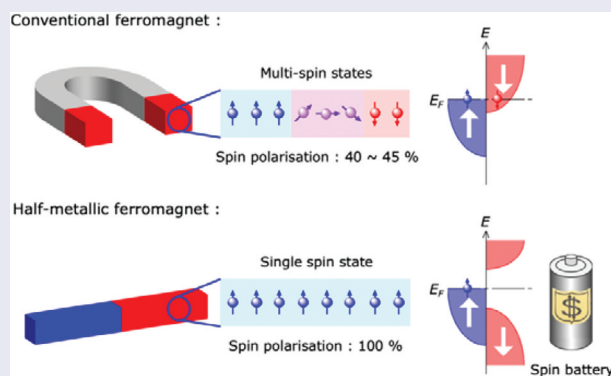
Received 16 April 2020

Revised 17 August 2020

Accepted 17 August 2020

## KEYWORDS



Heusler alloy; half-metallic ferromagnet; spin polarisation; magnetic moment; atomic disorder; curie temperature; minority bandgap; antiferromagnet; spin gapless semiconductor



## 1. Introduction

Spintronics has been initiated by the discovery of giant magnetoresistance (GMR) by Fert et al. [1] and Grünberg et al. [2] independently. A GMR device consists of a sandwich structure of a ferromagnet (FM)/non-magnet (NM)/FM multilayer, where an external magnetic field can align the FM

magnetisations in parallel to achieve a low-resistance state as compared with a high-resistance state with antiparallel magnetisations without a field application. The first-generation spintronic devices are based on magnetoresistive (MR) junctions, which have been used very widely [3,4], e.g., a read head in a hard disk drive (HDD) [5] and a cell in a magnetic random

**CONTACT** Atsufumi Hirohata  [atsufumi.hirohata@york.ac.uk](mailto:atsufumi.hirohata@york.ac.uk)  Department of Electronics Engineering, University of York, York, YO10 5DD, United Kingdom of Great Britain and Northern Ireland

© 2021 The Author(s). Published by National Institute for Materials Science in partnership with Taylor & Francis Group.

This is an Open Access article distributed under the terms of the Creative Commons Attribution License (<http://creativecommons.org/licenses/by/4.0/>), which permits unrestricted use, distribution, and reproduction in any medium, provided the original work is properly cited.

access memory (MRAM) [6]. The critical measure of efficient magnetic transport in these devices is an MR ratio, which is defined by

$$\text{MR ratio} = \Delta R/R = (R_{AP} - R_P)/R_P, \tag{1}$$

where  $R_P$  and  $R_{AP}$  represent the resistance measured for parallel and antiparallel configurations of the ferromagnet magnetisations, respectively. The MR ratio determines the signal-to-noise ratio of these devices, which directly corresponds to the miniaturisation of them. To date, the maximum GMR ratio in the current-in-plane (CIP) geometry has been reported to be 65% at 300 K in a  $[\text{Co} (0.8)/\text{Cu} (0.83)]_{60}$  (thickness in nm) junction [7].

Similar MR changes have been demonstrated in a magnetic tunnel junction (MTJ) by replacing an NM layer with an oxide tunnelling barrier in a GMR junction [8]. Tunnelling magnetoresistance (TMR) at room temperature (RT) has then been achieved by Miyazaki and Tezuka [9] and by Moodera et al. [10] independently. Since then, the TMR ratio has been improved very rapidly to 81% in MTJ consisting of  $\text{Co}_{0.4}\text{Fe}_{0.4}\text{B}_{0.2}$  (3)/Al (0.6)- $\text{O}_x$ / $\text{Co}_{0.4}\text{Fe}_{0.4}\text{B}_{0.2}$  (2.5) (thickness in nm) at RT [11]. By replacing amorphous  $\text{AlO}_x$  with epitaxial MgO, theoreticians have predicted over 1,000% TMR ratios due to coherent tunnelling via the  $\Delta_1$  band matched at an Fe/MgO interface [12,13]. Here, the TMR ratio can be defined as [8]

$$\text{TMR ratio} = 2P_1P_2/(1-P_1P_2), \tag{2}$$

where  $P_{1(2)}$  are effective spin polarisation of a ferromagnetic layer 1(2), respectively. For the coherent tunnelling,  $P_{1(2)}$  can be 100%, leading to the TMR ratio of infinity. Experimentally, giant TMR ratios have been reported by Parkin [14] and Yuasa [15] independently. Accordingly, a TMR ratio as large as 604% has been achieved in MTJ consisting of  $\text{Co}_{0.2}\text{Fe}_{0.6}\text{B}_{0.2}$  (6)/MgO (2.1)/ $\text{Co}_{0.2}\text{Fe}_{0.6}\text{B}_{0.2}$  (4) (thickness in nm) at RT [16]. Such a drastic increase in the TMR ratio has increased the areal density of HDD by almost four times over the last decade, for example [3].

As shown in Figure 1 for 1 Gbit MRAM, the junction cell diameter (fabrication rule) should be <65 nm with a resistance area product (RA) <30  $\Omega\cdot\mu\text{m}^2$  and an MR ratio >100% [18]. For 10 Gbit MRAM, the cell diameter should be reduced to be <20 nm with RA < 3.5  $\Omega\cdot\mu\text{m}^2$  and an MR ratio >100%. Here, low RA is required to satisfy the impedance matching [19] and low power consumption (<100 fJ/bit). A standard MRAM architecture commercially employed is one MRAM cell with a transistor attached, where a large MR ratio (>150%) is essential to maintain a signal-to-noise ratio allowing for a read-out signal voltage to be detected by a small-current application. In order to achieve these requirements, the intensive investigation

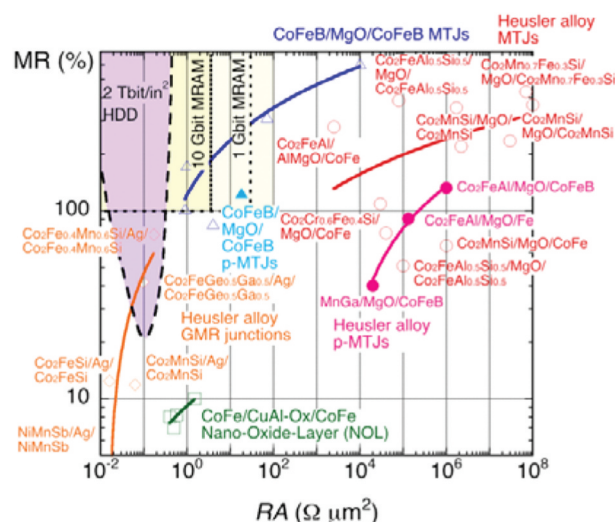


**Figure 1.** Relationship between a MR ratio and RA of MTJs with CoFeB/MgO/CoFeB (blue triangles), nano-oxide layers (NOL, green squares) and Heusler alloys (red circles) with in-plane (open symbols) and perpendicular magnetic anisotropy (closed symbols) together with that of GMR junctions with Heusler alloys (orange rhombus). The target requirements for 2 Tbit/in<sup>2</sup> HDD read heads as well as 1 and 10 Gbit MRAM applications are shown as purple and yellow shaded regions, respectively. Reprinted with permission from Hirohata et al. [17]. Copyright 2018. MDPI AG.

has been carried out on the CoFeB/MgO/CoFeB junctions. In-plane CoFeB/MgO/CoFeB MTJs have successfully satisfied the requirement for 10 Gbit MRAM by achieving RA = 0.9  $\Omega\cdot\mu\text{m}^2$  and TMR = 102% at RT [20] as shown as open triangles with a blue fit in Figure 1. For further miniaturisation of the MRAM cells and the corresponding increase in the density, a perpendicularly magnetised MTJ (p-MTJ) has been investigated to achieve the requirement for 1 Gbit MRAM with RA = 18  $\Omega\cdot\mu\text{m}^2$  and TMR = 124% at RT [21]. Further improvement has been made to satisfy 10 Gbit MRAM target [22], with satisfying a TMR ratio >100% and RA ~ 2  $\Omega\cdot\mu\text{m}^2$ . These MTJs under development are expected to replace the current-generation 256 Mbit MRAM with perpendicular magnetic anisotropy produced by Everspin [23]. Samsung shipped their new MRAM with a 28-nm fabrication rule for embedded-memory evaluation in March 2019 [24].

For a 2 Tbit/in<sup>2</sup> HDD application, on the other hand, MTJ cannot be used as the requirement for RA is almost one order of magnitude smaller than that for 10 Gbit MRAM [25]. One attempt is a nano-oxide layer (NOL) developed by Toshiba, which restricts a current path perpendicular to a GMR stack by oxidising a part of the NM Cu or Al spacer layer [26]. A  $\text{Co}_{0.5}\text{Fe}_{0.5}$  (2.5)/Al-NOL/ $\text{Co}_{0.5}\text{Fe}_{0.5}$  (2.5) junction has demonstrated RA = 0.5 ~ 1.5  $\Omega\cdot\mu\text{m}^2$  and MR = 7 ~ 10% at RT. These values are below the requirement for the 2 Tbit/in<sup>2</sup> HDD, and hence further improvement in these junctions is crucial.

For further improvement in the MR junctions to meet the requirements beyond 10 Gbit MRAM and 2 Tbit/in<sup>2</sup> HDD, a half-metallic ferromagnet (HMF) needs to be developed to achieve 100% spin polarisation at the Fermi energy level ( $E_F$ ) at RT [27], leading to an infinite MR ratio using Eq. (1). The half-metallicity is induced by the formation of a bandgap  $\delta$  only in one of the electron-spin bands in density of states (DOS) as schematically shown in Figure 2. There are four major types of HMFs theoretically proposed and experimentally demonstrated to date; (1) oxide compounds (e.g., rutile CrO<sub>2</sub> [28] and spinel Fe<sub>3</sub>O<sub>4</sub> [29]); (2) perovskites (e.g., (La,Sr)MnO<sub>3</sub> [30]); and, (3) magnetic semiconductors, including Zincblende compounds (e.g., EuO and EuS [31], (Ga,Mn)As [32] and CrAs [33]) and (4) Heusler alloys (e.g., NiMnSb [34]). Among these HMFs, magnetic semiconductors have been reported to show 100% spin polarisation in a film form due to their Zeeman splitting in two spin bands. However, their Curie temperatures ( $T_C$ ) are still below RT [35]. Low-temperature Andreev reflection measurements have confirmed that both rutile CrO<sub>2</sub> and perovskite La<sub>0.7</sub>Sr<sub>0.3</sub>MnO<sub>3</sub> compounds possess almost 100% spin polarisation [36]; however, no experimental report has been proved the half-metallicity at RT to date. The Heusler alloys exhibit the half-metallicity at RT in a bulk form but not in an *ex situ* film form [37–39] but in an *in situ* film, (93 + 7/-11)% [40]. Therefore, the Heusler alloy films can be the most promising candidate for the RT half-metallicity due to their lattice constant matching with major substrates, high  $T_C$  and large  $\delta$  at  $E_F$  in general as detailed in the following sections.

## 2. Heusler alloys

In order to employ the Heusler alloy films in spintronic devices, both advantages and disadvantages need to be considered as listed in Figure 3. Both structural and magnetic properties of the Heusler alloys can be controlled by the substitution of constituent elements of the

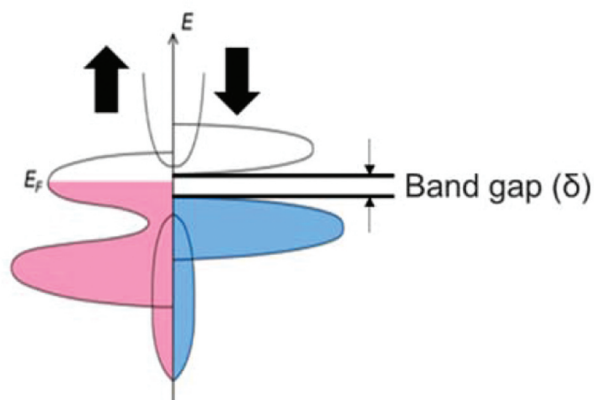


Figure 2. Schematic diagram of spin DOS for a HMF.

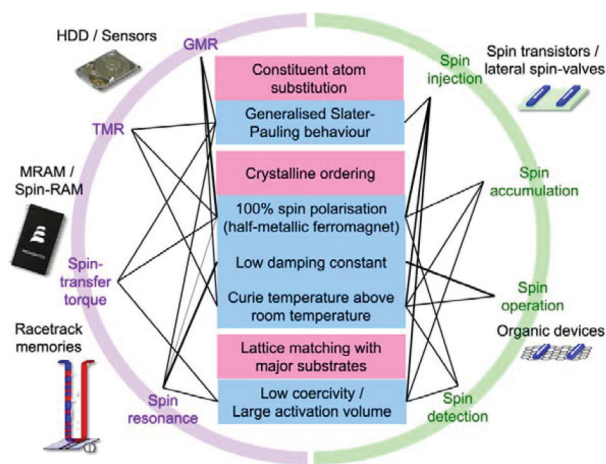
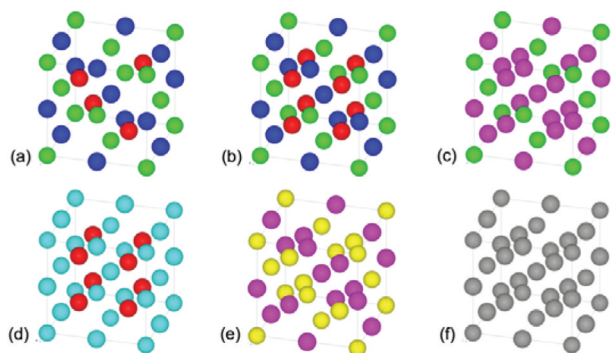


Figure 3. List of advantages and disadvantages of the Heusler-alloy usage in spintronic devices [41]. The width of the links represents the importance. Reprinted with permission from Hirohata et al. [17]. Copyright 2016.

alloy as detailed in the following sections. For example, the total spin magnetic moments, and the corresponding saturation magnetisation, can be precisely controlled by atomic substitution. Such controllability is useful for spin injection to minimise a stray field for the applications of an HDD read head, an MRAM cell and a magnetic racetrack memory, for instance. These properties also depend on the crystalline ordering of the Heusler alloys. For the half-metallicity, low damping constants and high Curie temperature, the perfect crystalline ordering needs to be achieved. Any departure from theoretical prediction on these properties can be attributed to disordering of the alloys. These magnetic properties are important for spin injection, accumulation, operation and detection in spintronic devices. Both structural and magnetic properties of the Heusler alloys are also depend on the lattice matching with substrates and seed layers. A low coercivity and large activation volume can be achieved by removing strain induced by lattice mismatch between them. These magnetic properties are again important for spin transport in devices.

### 2.1. Crystalline structures

Since the initial discovery of ferromagnetism in a ternary Cu<sub>2</sub>MnAl alloy, consisting of non-magnetic (NM) elements, by Heusler in 1903 [42], the Heusler alloys have been investigated intensively for various applications, including spintronic devices [37–39,41], magnetic refrigeration [43] and shape memory [44]. The Heusler alloys are categorised into two distinct groups by their crystalline structures; (1) half Heusler alloys with the form of XYZ in the C1<sub>b</sub> structure and (2) full Heusler alloys with the form of X<sub>2</sub>YZ in the L2<sub>1</sub> structure as schematically drawn in Figure 4(a,b), respectively. Here, X and Y atoms are transition metals, while Z is either a semiconductor or an NM



**Figure 4.** Crystalline structures of both (a) half- and (b) full-Heusler alloys;  $C1_b$  and  $L2_1$  structures, respectively. Atomically disordered structures, (c)  $D0_3$ , (d)  $B2$ , (e)  $B32a$  and (f)  $A2$ , are also shown. Data taken from Refs. [38,45,46].

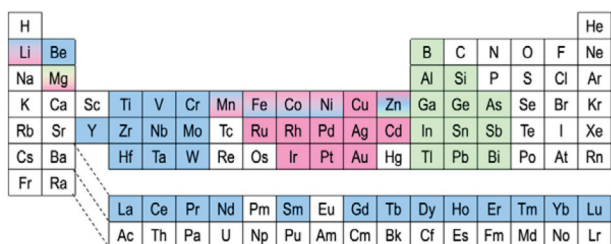


**Figure 5.** Periodic table showing typical X (blue colour), Y (pink colour) and Z (green colour) elements in Heusler compounds. Data are taken from Refs. [38,45,46].

metal [see Figure 5] [34,45]. The unit cell of the  $L2_1$  structure consists of four face-centred cubic (fcc) sublattices, while that of the  $C1_b$  structure is formed by removing one of the X sites. In the Heusler alloys, the half-metallicity is known to be fragile against atomic disorder. For the  $L2_1$  structure, when the Y and Z atoms replace their sites (Y-Z disorder) and eventually occupy their sites absolutely at random, the alloy transforms into the  $B2$  structure [see Figure 4(c)]. Similarly, the X-Y disorder occurs to lead to the  $D0_3$  structure as shown in Figure 4(d). The mixture of X-Y and X-Z disorder forms the  $B32a$  structure [see Figure 4(e)]. In addition, X-Y and X-Z disorder finally forms the  $A2$  structure as shown in Figure 4(f).

Recent studies propose the other classes of Heusler-alloy family, such as inverse [47,48] and equiatomic quaternary Heusler alloys [49,50]. The form of inverse Heusler alloys can be described as  $XYXZ$  for which one of X atom in the  $L2_1$  structure replaces with Y atom. Similarly, the form of equiatomic quaternary Heusler alloy can be described as  $XX'YZ$  for which one of X atom in the  $L2_1$  structure changes to the 4th element,  $X'$ . Interestingly, some of inverse Heusler alloys and equiatomic quaternary Heusler alloys also exhibit half-metallic electronic structure as well as electronic structure of spin gapless semiconductor (see Section 9.2).

Due to the complicated crystalline structures of the Heusler alloys as described above, they require very high temperature (typically >1000 K in the bulk form and

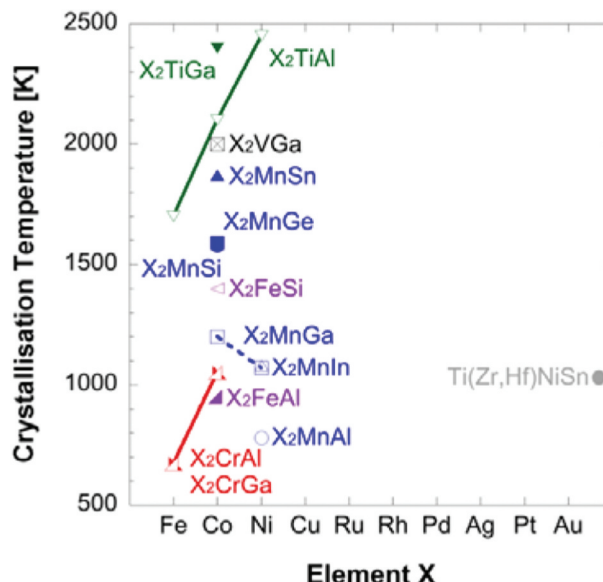


**Figure 6.** Crystalline ordering temperature of full-Heusler bulk alloys with respect to the element X. Experimental data are taken from Refs. [37,55,56].

>650 K in the thin-film form) for their crystalline ordering as shown in Figure 6 [51]. This fact hinders the use of Heusler alloy films to be used in spintronic devices. Recently, layer-by-layer crystallisation has been reported along the Heusler alloy (110) plane to reduce the crystallisation energy, resulting in the annealing temperature, by over 50% [52]. A similar crystallisation process has been demonstrated at a higher temperature to uniformly crystallise the Heusler alloy films [53]. Further reduction has been achieved using a W(110) seed layer, allowing over 80%  $B2$  ordering by annealing at 355 K for 2 min [54]. Such layer-by-layer crystallisation can open a way for the implementation of a Heusler alloy film into spintronic devices.

Most of crystallised Heusler alloys possess their lattice constants within the range of those of major substrates, clearly indicating the possibilities of epitaxial growth. Co-based full Heusler alloys especially hold excellent match with both GaAs(001) and MgO(001) substrates. The lattice constant can be precisely engineered to a required value by substituting a constituent element of the Heusler alloy X with a different atom as indicated as lines in Figure 7, and also by substituting the other elements Y or Z with the other atoms as categorised in Figure 7 with retaining the element X (e.g.,  $Co_2(Cr,Fe)Al$ ). Such a crystallographical engineering approach is a powerful method to control the spin DOS in a unit cell to achieve robust half-metallicity at RT.

### 2.2. Magnetic properties

The Curie temperature  $T_C$  of the Heusler alloys falls typically within the range between 200 and 1200 K as shown in Figure 8.  $T_C$  can also be further tuned to be well above RT by the atomic substitution as described

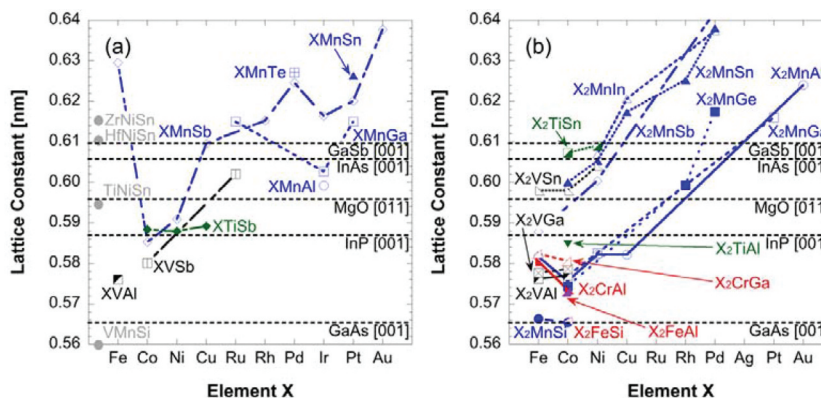


**Figure 7.** Lattice constant distribution of both (a) half- and (b) full-Heusler bulk alloys with respect to the element X. Experimental data are used from Refs. [41,45,57,58] and calculated data are taken from Refs. [59,60,61]. Lattice constants of major substrates are also shown as references.

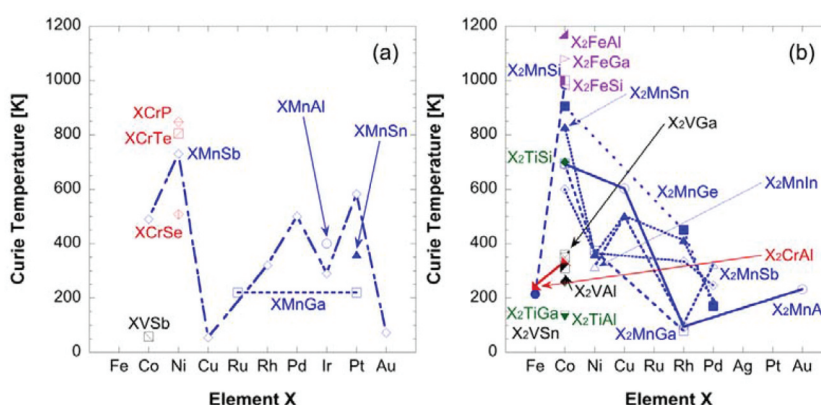


**Figure 8.** Curie temperature distribution of both (a) half- and (b) full-Heusler bulk alloys with respect to the element X. Experimental data are used from Refs. [41,45,57,58,61,62,66] and calculated data are taken from Refs. [63–64].

in the previous section, achieving required spontaneous magnetisation at RT for the applications.

The robustness of the half-metallicity depends on the size and definition of the bandgap  $\delta$  formed in one electron-spin band in the vicinity of Fermi energy level  $E_F$ .  $\delta$  is formed by the strong  $d$ -band hybridisation between the two transition metals of X and Y, according to *ab initio* calculations [67]. Typically,  $\delta$  of 0.4 ~ 0.8 eV is expected to be formed at 0 K [38]. At a finite temperature, however, the bandgap becomes smaller and the edge definition of  $\delta$  becomes broader.  $\delta$  has been measured by detecting photon absorption

of circularly polarised infrared light with energy corresponding to  $\delta$  [64,68].

The origin of  $\delta$  in the Heusler alloys is attributed to the strong  $d$ -band hybridisation of the two elements X and Y. According to the calculations by Galanakis et al. [69], the local DOS in the vicinity of  $E_F$  is dominated by the  $d$ -states, forming an energy gap between the higher degenerate of bonding hybridised states in the valence band and the lower degenerate of antibonding states in the conduction band. For the half-Heusler alloys [Figure 9 (a)], the gap is formed between the hybridised

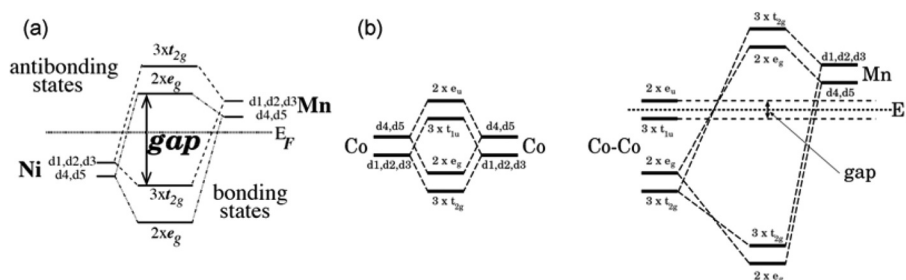


**Figure 9.** Schematic illustrations of the origin of the minority bandgap in (a) half- and (b) full-Heusler alloys (NiMnZ and  $\text{Co}_2\text{MnZ}$  as examples, respectively).  $d_1, d_2, d_3, d_4$  and  $d_5$  represent  $d_{xy}, d_{yz}, d_{zx}, d_z^2$  and  $d_{x^2-y^2}$  orbitals, respectively. Reprinted with permission from Galanakis et al. [69]. Copyright 2006. The Institute of Physics Publishing.

states of the elements X and Y, *i.e.*, between the three-fold degenerate ( $t_{2g}$ ) in the bonding states and the two-fold degenerate ( $e_g$ ) in the antibonding states. Therefore, most of the half-Heusler alloys possess an indirect bandgap between the valence band minimum at the  $\Gamma$  point and the conduction maximum at the X point. For the full Heusler alloys, on the other hand, the  $d$ -band hybridisation between the elements X plays a very important role, although these atoms occupy the second-nearest neighbour sites [see Figure 4(b)]. As shown in Figure 9(b), the X–X hybridisation initially forms both bonding and antibonding states for both  $t_{2g}$  and  $e_g$ . The two bonding states among these four X–X orbitals then hybridise with the Y degenerates, developing both bonding and antibonding degenerates with a very large gap in between. The two X–X antibonding states, however, cannot couple with the Y degenerates, maintaining the small gap across  $E_F$ , which defines the bandgap for the full-Heusler alloys. This can provide either a direct bandgap at the  $\Gamma$  point or an indirect bandgap between the  $\Gamma$  and X points.

In the Heusler alloys, total spin magnetic moments per formula unit (f.u.)  $M_t$  have been reported to follow the generalised Slater-Pauling curve by Galanakis et al., which is represented as  $M_t = Z_t - 18$  (half-Heusler) and  $Z_t - 24$  (full-Heusler), where  $Z_t$  is the total number of valence band electrons as shown in Figure 10 [67,69]. This behaviour enables us to preferentially control the magnetic properties, the spin DOS at  $E_F$  in particular, continuously by substituting the Y atoms with the other transition metals as listed in Figure 5. Even though there are almost 3,000 possible combinations to form ternary Heusler alloys, there are about a few tens of alloys reported to become the HMFs according to theoretical calculations to date [see Tables 1 and 2]. For example, a  $\text{Co}_2\text{CrAl}$  alloy has been theoretically calculated to become a HMF [70]; however,  $T_C$  has been reported to be around RT

(334 K) for bulk [71]. In order to increase  $T_C$ , the substitution of the Cr atoms with the Fe atoms has been successfully reported experimentally [72,73], proving the spin engineering by crystallographical manipulation.

### 3. Ferromagnetic Heusler alloys

#### 3.1. Half-Heusler alloy films

Since the pioneering theoretical prediction on the half-metallicity of a NiMnSb half-Heusler alloy [34], this alloy has been intensively investigated to confirm its half-metallicity experimentally. As listed in Table 1, the magnetic moment per formula unit and the band-gap  $\delta$  are calculated as  $3.99 \mu_B/\text{f.u.}$  and  $0.5 \text{ eV}$  [69], respectively. The corresponding spin polarisation is calculated to be 99.3% [75]. For a bulk single crystal, the NiMnSb alloy has indeed been measured to show almost 100% spin polarisation at  $E_F$  by means of spin-polarised positron-annihilation [76,77]. Both ultra-high vacuum (UHV) co-sputtering [78] and molecular beam epitaxy (MBE) [79] techniques are employed to grow epitaxial films, which are characterised mostly by X-ray diffraction (XRD) and magnetocrystalline anisotropy measurements. However, the spin polarisation is found to be only 28% at 0.4 K estimated from TMR [79]. For the NiMnSb film grown in a similar manner, the surface spin polarisation  $P$  is measured to be only ~58% [36]. This large departure from the bulk property can be explained by the presence of the atomic disorder at the empty sites [80].  $\delta$  for the minority spins at  $E_F$  is reported to vanish with an atomic disorder of more than 7%. In addition, the surface state is very fragile due to the reduced symmetry and the surface reconstruction [81,82]. On the contrary, epitaxial NiMnSb (100) films grown on Mo(100) buffers on MgO(111) substrates have shown  $(67 \pm 9)$  to 100% spin polarisation at the MnSb terminated surface, which is much higher than that of 50% for polycrystalline samples measured by angle-resolved X-ray photoemission [83]. A study on epitaxial NiMnSb(001) growth on MgO(001) has also been performed with using a V(001) buffer layer by Turban et al. [84]. They find the Stransky-Krastanov growth mode under the optimised growth temperature of 620 K. The corresponding magnetic moment is estimated to be  $(3.9 \pm 0.2) \mu_B/\text{f.u.}$ , which agrees almost perfectly with the calculations [34,69].

Epitaxial NiMnSb(001) growth on GaAs(001) has been studied systematically by van Roy et al. [85]. The films are grown at RT (300 K) to avoid interfacial  $\text{Mn}_2\text{As}$  mixing between NiMnSb and GaAs, which may introduce a magnetically dead layer. The lattice constant is slightly enhanced to  $0.5904 \sim 0.5909 \text{ nm}$  as compared with the bulk value ( $0.5903 \text{ nm}$ ) due to the small lattice mismatch with GaAs. Stoichiometric epitaxial NiMnSb films are also grown on GaAs(111)B [86]. These results

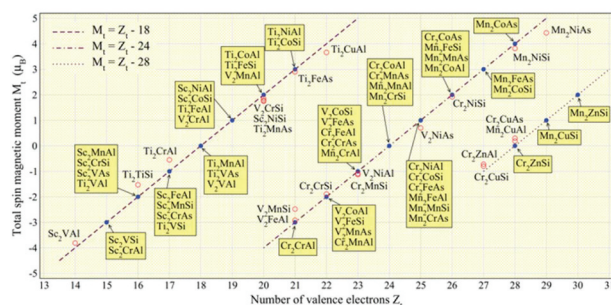


**Figure 10.** Total spin magnetic moments per unit cell ( $M_t/\text{f.u.}$ ) as a function of the total number of valence electrons in the unit cell for major Heusler alloys. The lines represent three different forms of the generalised Slater-Pauling curves. Reprinted with permission from Skaftouros et al. [74]. Copyright 2006. The American Physical Society.



**Table 1.** List of major magnetic properties of half-metallic half-Heusler alloys. Italic and roman letters correspond to calculated and experimental values, respectively. \* indicates calculated total magnetic moments per formula unit, while the others are calculated spin magnetic moments per formula unit.

Half Heusler alloys	Magnetic moment [ $\mu_B$ /f.u.]		$\delta$ [eV]	$T_C$ [K]	$P$ [%]	Refs.
	Calculation	Experiment				
NiMnSb	4.00 [34]	3.85 (bulk) [45,88]	0.5 [69]	900 ~ 1112 [100]	99.3 [82]	[78,79,82,85–87,90–95]
	3.9910 [75]	3.6 (poly) [89]	0.5 [83]	730 (bulk) [45]	58 ± 2 [36]	
	3.991 [69]*	3.9 ± 0.2 [84]	0.55 [61]		~ 44 [89]	
	3.96 [70,87]	4.01 ± 0.02 [87,90]			~ 100 [76,77]	
PtMnSb	4.00 [34]	4.14 (bulk) [45]		582 (bulk) [45]		[92,96]
	3.997 [69]*	3.97 (bulk) [88]				[99]
FeMnSb	1.930 [97]* [69]*		0.436 [60]		99.3 [75]	
	2.000 [98]					
CoMnSb	2.949 [67]* [69]*	4.0 (bulk) [45]	~ 1 [69]	671 ~ 815 [100]	99.0 [75]	[88]
	3.000 [99]	3.00 [61]		490 (bulk) [45]		
CoTiSb			0.95 [101]			
			0.82 [69]			
			1.03 [102]			
NiTiSb	0.0 [101]		0.14 [69]	330 (bulk) [70]		
FeVSb			0.36 [69]			
			0.38 [63]			
CoZrSb			0.83 [69]			

**Table 2.** List of major magnetic properties of full-Heusler alloys. Italic and roman letters correspond to calculated and experimental values, respectively. \* indicates calculated total magnetic moments per formula unit, while the others are calculated spin magnetic moments per formula unit. Spin-polarisation values with † and †† are estimated at RT and 2 K, respectively, by using Jullière’s formula [8]. Several non-half-metallic full Heusler alloys are also shown in brackets as references.

Full Heusler alloys	Magnetic moment [ $\mu_B$ /f.u.]		$\delta$ [eV]	$T_C$ [K]	$P$ [%]	Refs.
	Calculation	Experiment				
Co <sub>2</sub> MnAl	4.09 [106]	4.01 (bulk) [45]	0.306 [109]	693 (bulk) [45]	42 [110]†	[112]
	4.10 [107]				58 [111]†	[113]
	3.970 [67]				60 [62]	[114]
	4.020 [108]					
	4.036 [69,97] *					
Co <sub>2</sub> MnSi	5.00 [106]	5.07 (bulk) [45]	0.419 [109]	740 ~ 857 [100]	54 ± 3 [117]	[114]
	4.96 [115]	5.10 ± 0.04 (bulk) [116]	0.81 [121]	985 (bulk) [45]	35 [122]†	
	4.940 [67]	4.95 ± 0.25 [117]		690 [57]	89 [122]††	
	5.0 [116]	4.7 [118]		900 [62]	56 [62]	
	5.008 [69,97] *	5.0 [119]				
		5.1 [120]				
Co <sub>2</sub> MnGa	4.14 [106]	4.05 (bulk) [45]		694 (bulk) [45]	~ 50 [123]	[124]
	4.21 [107]			700 [62]	60 [62]	
	3.72 [115]					
	4.058 [67]					
Co <sub>2</sub> MnGe	5.00 [106]	5.11 (bulk) [45]	0.210 [109]	905 (bulk) [45]	58 [62]	[105]
	4.84 [115]	4.93 (bulk) [125]	~ 0.5 [106]	900 [62]		[126]
	4.941 [67]	5.1 [104]				
	5.0 [120]					
	5.012 [69,97] *					
Co <sub>2</sub> MnSn	5.03 [106]	5.08 (bulk) [45]	0.174 [109]	829 (bulk) [45]	60 [62]	[114]
	4.78 [115]			800 [62]		
	4.984 [67]					
	5.0 [116,120]					
	5.043 [108]					
	5.089 [69,97] *					
Co <sub>2</sub> CrAl	2.99 [106]	1.55 (bulk) [45]	0.18 [87]	334 (bulk) [45]	~ 100 [87]	[131]
	2.955 [67]	1.5 ~ 3 [129]	0.75 [127]	330 [130]	~97 [131]	[132]
	3.007 [108]	0.53 [130]	0.18 [128]	600 [62]	~98 [128]	[133]
	3.0 [87]				16 [132]†	[134]
	2.999 [69] *				62 [62]	[135]
	2.96 ~ 3.01 [127]					
	2.970 [128]					
Co <sub>2</sub> Cr <sub>0.6</sub> Fe <sub>0.4</sub> Al	3.7 [131]	3.4 (bulk) [136]	~ 0.4 [127]	750 (bulk) [136]	~ 90 [141]	
		3.65 (bulk) [137]		665 ± 2 (bulk) [137]	~ 95 [128]	
		2.04 [73]			18 [73]†	
		3.5 [129]			25 [137]†	
		3.1 [132]			29 [132]†	
		3.2 (RT) (bulk) [138]				
		3.49 (bulk) [139]				
		3.3 [140]				
		2.26 (RT) [38]				

(Continued)

**Table 2.** (Continued).

Full Heusler alloys	Magnetic moment [ $\mu_B$ /f.u.]		$\delta$ [eV]	$T_C$ [K]	$P$ [%]	Refs.
	Calculation	Experiment				
(Co <sub>2</sub> FeAl)	4.996 [106]	4.9 [129]	0.1 [127]	1170 (bulk) [61]	~ 30 [141]	[131]
	4.98 [107]	4.8 [130]			46 [132]†	[132]
	4.98 [67]	5.29 [139]			59 [62]	[135]
	4.996 [69]*					
	4.811 [128]					
Co <sub>2</sub> CrGa	3.01 [106]	3.01 (bulk) [141]		495 (bulk) [141]	95 [141]	
Co <sub>2</sub> FeSi	5.28 [142]	0.35 [142]		1109 [143]	16 [145]	[150]
	5.48 [143]	0.10 [143]		1100 [144]	57 ± 1 [147]	[151]
	6.0 [144]	~ 0.15 [144]		1100 [62]	42 [148]	[153]
	5.97 ± 0.05 [144]				74 [148]	[154]
	6.00 [145]				60 [62]	[155]
	5.5 [146]					
	5.73 [147]					
	4.36 ± 0.55 [148]					
	5.56 [148]					
	4.8 [149]					
Co <sub>2</sub> FeGa				1100 [62]	58 [62]	
Co <sub>2</sub> FeGe				1000 [62]	58 [62]	
Co <sub>2</sub> NiGa		3.21 (bulk) [45]		670 [57]		
Co <sub>2</sub> TiAl	1.00 [156]		0.438 [156]	135 (bulk) [157]		
				126 [66]		
Co <sub>2</sub> TiSi	2.00 [156]		0.800 [156]			
			0.62 [143]			
			0.64 [157]			
Co <sub>2</sub> TiGa	1.00 [156]		0.157 [156]			
Co <sub>2</sub> TiGe	2.00 [156]		0.602 [156]			
Co <sub>2</sub> TiSn	1.85 [115]	1.93 (bulk) [45]	0.478 [156]	359 [115]	57 [62]	
	1.784 [67]	1.92 (bulk) [158]	0.0123 [159]	359 (bulk) [45]		
	2.00 [156]			~ 350 (bulk) [159]		
	1.68 [158]			364 [62]		
Co <sub>2</sub> VAl					48 [62]	
Co <sub>2</sub> VSi	3 [[143]		0.68 [143]	566 [[143]		
Co <sub>2</sub> ZrAl				194 [66]		
Co <sub>2</sub> ZrSn	1.64 [158]	1.64 (bulk) [158]				
Co <sub>2</sub> NbSn	1.08 [158]	0.94 (bulk) [158]				
(Co <sub>2</sub> TiSb)	1.73 [156]		0.567 [156]			
Co <sub>2</sub> FeGa	5.15 [115]			> 1100 [115]		
(Ni <sub>2</sub> MnAl)				~ 350 [160]		
(Ni <sub>2</sub> MnGa)				~ 320 [161]		[164]
				~ 350 [162]		
				~ 340 [163]		
(Ni <sub>2</sub> MnGe)				~ 320 [163,165,166]		
(Ni <sub>2</sub> MnIn)				~ 170 (B2) [166]		
				318 (L2 <sub>1</sub> and B2) [167]	34 [167]††	[168]
				320 ~ 323 [66]		
(Ni <sub>2</sub> MnSb)				334 [66]		
(Ni <sub>2</sub> MnSn)				344 [66]		
(Cr <sub>2</sub> MnP)	0.102			240		[169]
(Cr <sub>2</sub> MnAs)	0.096			250		[169]
Cr <sub>2</sub> MnSb	0.036			342		[169]
(Cr <sub>2</sub> MnBi)	-0.011			320		[169]
(Fe <sub>2</sub> VAl)					56 [62]	
(Pd <sub>2</sub> MnSb)				247 [66]		
(Pd <sub>2</sub> MnSn)				189 [66]		

clearly indicate that the presence of the vacancy sites in the half-Heusler alloy [see Figure 4(a)] does not contradict high chemical ordering under precisely controlled deposition. They also find that these films contain very small point defect concentrations: 1.1% Mn planer defects appear in a 1 nm thick region in the vicinity of the NiMnSb/GaAs:B interface, which agrees very well with calculations that the half-metallicity can be recovered within less than 6 atomic planes ( $\leq 0.7$  nm) [91]. For the NiMnSb interfaces, the lattice mismatch is calculated to induce strain: 2% lattice expansion reduces  $\delta$  by 0.25 eV, while 2% lattice compression increases  $\delta$  by 0.5 eV [88], and the -2 to +3% lattice expansion maintains the half-metallicity [87].

Besides the possible disappearance of the half-metallicity due to the atomic disorder and the interfacial mixing, which can be overcome by the optimised growth as mentioned above, the surface spin polarisation is calculated with respect to the interfaces, the crystalline orientations and the terminated lattice planes. For the NiMnSb(001) surfaces, the Ni-terminated surface compresses the distance between the topmost Ni atoms and the subsurface MnSb layers by 10% ( $P = 42\%$ ), while the MnSb-terminated surface reduces the distance between the topmost Mn and the subsurface Ni layers by 3.5% and expands that between the topmost Sb and the subsurface Ni layers by 7.3% ( $P = 84\%$ ) [94]. The NiMnSb(111) surfaces, on the

other hand, show much larger surface deformation: The Ni-terminated surface shows 23% and 18% reduction in the Ni-Sb and Ni-Mn distances, respectively, reducing the corresponding  $P$  significantly. For the case of a NiMnSb/InP interface, the Mn surface is calculated to increase the spin moment up to  $4.0 \mu_B$ , inducing the corresponding spin polarisation of about 74%, while the Ni/P interface reduces the spin polarisation down to 39% for the first two interfacial layers [95].

Similar argument can be applied for the other half-Heusler alloy films. PtMnSb films are deposited on  $Al_2O_3(0001)$  [96,99] and  $MgO(001)$  [103] by sputtering to form spin-valve structures, showing <1% giant magnetoresistance (GMR) at RT. This small GMR ratio may also be due to the empty site disorder at the interfaces. Calculations suggest the decrease in the surface spin polarisation depends on the terminated layers;  $P \sim 46\%$  and  $22\%$  for the MnSb and Pt termination, respectively, [92]. The other half-Heusler alloy of CoMnSb shows a similar decrease in the surface spin polarisation and the bandgap by the strain: +2% and -2% lattice deformation shifts  $\delta$  by -0.8 eV and +0.9 eV, respectively [94].

### 3.2. Full-Heusler alloy films

#### 3.2.1. Co-based full-Heusler alloys

(i)  $Co_2MnZ$ . A pioneering work on the growth of full-Heusler-alloy films has been carried out for a  $Co_2MnGe/GaAs(001)$  hybrid structure by Ambrose et al. [104]. They obtain an epitaxial  $Co_2MnGe$  film with a slightly enhanced lattice constant as compared with bulk. The magnetic moment is estimated to be  $5.1 \mu_B/f.u.$ , which almost perfectly agrees with the bulk value [see Table 2]. For this alloy, calculations suggest that the strong reduction in the magnetic moment may occur near the  $Co_2MnGe/GaAs$  interface due to the Co-As and Co-Ga bonding [105].

Consequently, systematic search has been widely performed over  $Co_2Mn$ -based full Heusler alloys to realise the half-metallicity at RT;  $Co_2MnAl$  [110–114],  $Co_2MnSi$  [115–117,118–120,122],  $Co_2MnGa$  [123,124] and  $Co_2MnSn$  [114]. For  $Co_2MnAl$ , an epitaxial film has been grown on a Cr buffer layer by UHV sputtering with the crystalline relationship of  $Co_2MnAl(001)[110]||Cr(001)[110]||MgO(001)[100]$  but with the  $B2$  structure [112]. For  $Co_2MnSi$ , the  $L2_1$  structure has been deposited using both UHV dc magnetron sputtering [117,118,120,122] and MBE techniques [119]. Some of these films are used as electrodes in MTJ and recently show large TMR ratios at low temperature, which is discussed in Sec. 4.3.

Calculations imply that the strain induced in the unit cell can control the half-metallicity in the  $Co_2MnZ$  alloys as similarly discussed for the half-Heusler alloys in Sec. 3.1. For  $Co_2MnSi$  for example,

the lattice compression of 4% increases  $\delta$  by 23%, and a similar behaviour is expected for the other alloys [121]. Calculations also show that  $\pm 2\%$  change in the lattice constant preserves the half-metallicity in the  $Co_2MnZ$  alloys [69].

(ii)  $Co_2(Cr,Fe)Al$ . Block et al. have presented large negative magnetoresistance (MR) at RT in a quaternary full Heusler  $Co_2Cr_{0.6}Fe_{0.4}Al$  alloy [136], which firmly proves the controllability of the spin DOS of the Heusler alloys by substituting their constituent elements. They report -30% MR at RT for a pressed powder compact, which acts as a series of MTJs. As a result, a great amount of attempts has been made to utilise this alloy system to achieve a large MR ratio at RT due to the half-metallicity [73,129,132,137]. However, an epitaxial film is deposited on a  $MgO(001)$  substrate with the crystalline relationship of  $Co_2Cr_{0.6}Fe_{0.4}Al(001)[100]||MgO(001)[110]$ , showing only 2% GMR at RT (4% at 15 K) [129].

The influence of the atomic disorder on the half-metallicity for the  $Co_2Cr_{1-x}Fe_xAl$  full Heusler alloys has also been systematically studied by Shirai et al. using first principles calculations [131,132,141]. In the  $Co_2CrAl$  alloys, the atomic disorder between Cr and Al, which eventually deforms the crystalline structure from  $L2_1$  into  $B2$  at a disorder level of 0.5, maintains the very high spin-polarisation  $P$  of 97% for  $L2_1$  and 93% for  $B2$  [131]. The Co-Cr type disorder, however, destroys the half-metallicity rapidly:  $P$  falls to zero at a disorder level of 0.4 and the magnetic moment  $M_t$  reduces down to  $2.0 \mu_B/f.u.$  at the full disorder. For the Fe substitution  $x$  with Cr,  $P$  is calculated to stay above 90% up to  $x = 0.35$ . Similarly, in the  $Co_2Cr_{1-x}Fe_xAl$  alloys, the CrFe-Al type disorder preserves both  $P$  and  $M_t$  to be above 80% and  $3.7 \mu_B/f.u.$ , respectively, up to the disorder level of 0.5, while the Co-CrFe disorder eliminates  $P$  at the disorder level of 0.3 [132]. These findings may explain the decrease in the estimated  $M_t$  in the earlier study [73].

Strain also affects the half-metallicity in the  $Co_2CrAl$  alloy according to calculations [72].  $P$  stays  $\sim 100\%$  in the lattice strain range between -1 to +3%, and is even higher than 90% under +10% strain.  $\delta$  is also robust against the strain and can be maximised under +3% strain.  $P$  also remains  $\sim 100\%$  against the tetragonal distortion in the range of  $\pm 2\%$ , which is a great advantage for the epitaxial growth study on major substrates.

Experimentally, stoichiometric epitaxial  $Co_2Cr_{1-x}Fe_xAl$  films are directly grown on a  $GaAs(001)$  substrates using three-source co-evaporation with an ultrahigh vacuum (UHV) MBE technique, resulting in polycrystalline  $Co_2CrAl/GaAs$  and epitaxial  $L2_1 Co_2FeAl(001)/GaAs(001)$  hybrid structures [130]. The  $Co_2FeAl$  film grown at 673 K forms an almost perfect  $L2_1$  structure for the thickness above 7.5 nm, of which

crystalline relationship is  $\text{Co}_2\text{FeAl}(001)\langle 110 \rangle \parallel \text{GaAs}(001)\langle 110 \rangle$  with showing strong uniaxial anisotropy along the  $[1-10]$  direction with a magnetic moment of  $4.8 \mu_B/\text{f.u.}$  Even though the TMR ratio for this film is only 9% at RT, the growth condition for this Heusler alloy system has been successfully optimised. For intermediate states, e.g.,  $x = 0.4$ , the  $A2$  structure appears below the thickness of 1.2 nm [2 monolayers (MLs)], followed by the formation of the  $B2$  and then the  $L2_1$  structures above 2.0 nm (3.5 MLs).

### 3.2.2. Ni-based full-Heusler alloys

Even though  $\text{Ni}_2\text{MnZ}$  alloys are not predicted to become HMFs by calculations, detailed studies on epitaxial growth on GaAs and InAs have been reported by Palmström [57]. By employing a  $\text{Sc}_{0.3}\text{Er}_{0.7}\text{As}$  buffer layer on GaAs(001), both  $\text{Ni}_2\text{MnAl}$  [160] and  $\text{Ni}_2\text{MnGa}$  [161–164] films are epitaxially grown. Although  $\text{Ni}_2\text{MnGa}$  films are also epitaxially grown directly on GaAs(001) with the crystalline relationship of  $\text{Ni}_2\text{MnGa}(001)[100][010] \parallel \text{GaAs}(001)[100][010]$ , no strong in-plane magnetocrystalline anisotropy is observed in their magnetisation curves [164].  $\text{Ni}_2\text{MnGe}(001)/\text{GaAs}(001)$  [163,165] and  $\text{Ni}_2\text{MnIn}(001)/\text{InAs}(001)$  [166] hybrid structures are additionally fabricated for evaluation. Their interfaces are reported to be very sensitive to the growth temperature: Interfacial mixture occurs at the growth temperature of 373 K, while a large number of planer defects are formed at 433 K for  $\text{Ni}_2\text{MnGe}/\text{GaAs}$  [163]. All these films are slightly tetragonally elongated along the plane normal as compared with the bulk values due to the minor lattice mismatch with the semiconductor substrates, and eventually the  $\text{Ni}_2\text{MnIn}$  film on InAs transforms into the  $B2$  structure. First principles calculations demonstrate that a broad energy minimum of tetragonal  $\text{Ni}_2\text{MnGa}$  can explain stable pseudomorphic growth of  $\text{Ni}_2\text{MnGa}$  on GaAs despite a nominal 3% lattice mismatch [161]. An antiferromagnetic (AF) phase of the Ni-based full-Heusler alloys is discussed in Sec. 5.2.

## 4. Major characterisations techniques of ferromagnetic Heusler alloys

### 4.1. X-ray diffraction

For the structural analysis on the Heusler alloys, XRD is the most commonly used technique. XRD analysis predominantly focuses on both superlattice peaks, (111) and (200), and the principal peak (220). The appearance of all three peaks corresponds to the formation of the  $C1_b$  or  $L2_1$  structures in the Heusler-alloy films, while the disappearance of the (111) peak represents the formation of the  $B2$  structure and the disappearance of the two superlattice peaks indicates the formation of the  $A2$  structure for the full-Heusler alloys. For the  $L2_1$

structure of the  $X_2YZ$  full-Heusler alloys, the structure amplitudes of the XRD (111), (200) and (220) peaks are given by  $F(111) = 4 |f_Y - f_Z|$ ,  $F(200) = 4 |2f_X - (f_Y + f_Z)|$  and  $F(220) = 4 |2f_X + (f_Y + f_Z)|$ , respectively, where  $f_M$  ( $M = X, Y$  and  $Z$ ) are the average scattering factors for the  $M$  atoms [162]. The principal reflection (220) satisfies the relationship  $(h + k + l)/2 = 2n$  ( $h, k$  and  $l$ : Miller indices, and  $n$ : an integer number), and is not affected by the atomic disorder. When the disorder occurs absolutely randomly among the  $M$  atoms, the magnitude of the first two superlattice peaks are reduced by the factor  $S^2$ , where  $S$  is the degree of long range ordering described with the number of the  $X$  atoms on the  $L2_1$ -ordered  $X$  sites  $n_X$  as  $S = \{n_X - n_X(A2)\} / \{n_X(L2_1) - n_X(A2)\}$  ( $S = 1$  for the  $L2_1$  structure). When the  $Y$ - $Z$  disorder occurs, the second superlattice peak (200) with  $(h + k + l)/2 = 2n + 1$  is not affected, while the first peak with  $h, k$  and  $l$  are all odd is reduced by a factor of  $(1-2a)S^2$ , where  $a$  is a disorder parameter defined as the fraction of the  $Y$  atoms occupying the  $Z$  sites ( $a = 0.5$  for the  $B2$  structure). By applying the structure amplitudes  $F(hkl)$ , the XRD peak intensity  $I(hkl)$  can be calculated as follows:  $I(hkl) = |F(hkl)|^2 p \{(1 + \cos^2 2\theta)/\sin^2 \theta \cos \theta\}$  ( $p$ : multiplicity factor) [171]. For the polycrystalline  $\text{Co}_2\text{CrAl}$  alloy for instance, the peak intensity ratio normalised by the principal (220) reflection is calculated to be  $I(111):I(200):I(220) = 5:6:100$ , while it is  $7:5:100$  for the polycrystalline  $\text{Co}_2\text{FeAl}$  alloy [130]. Comparison of these calculated values with experimental observations provides a measure of the atomic ordering in the Heusler alloy samples, however, cannot be applied directly to the epitaxial films.

Takamura et al. demonstrated a quantitative analysis method of atomic disorders in  $\text{Co}_2\text{FeSi}$  Heusler alloy using XRD. It is capable to evaluate all the atomic disorders for the exchanges  $X, Y$  and  $Z$  atoms in full-Heusler  $X_2YZ$ . Such technique relies on the use of different atomic scattering factors ( $f_{\text{Co}}$  and  $f_{\text{Fe}}$ ) of Co and Fe for Co  $K\alpha$  source. Hence, superlattice diffraction intensities for Co  $K\alpha$  can reflect the  $D0_3$  disorder [172]. A physical model proposed by Niculescu et al. was used so that the disorder parameters can be expressed in terms of  $\alpha, \beta$  and  $\gamma$ . These parameters represent the quantitative disorder of  $B2$  (atom mixing between Fe and Si),  $A2$  (atom mixing between Co and Si) and  $D0_3$  (atom mixing between Co and Fe) disorder, respectively [173].

### 4.2. Cross-sectional transmission electron microscopy

Gabor et al. studied the correlation between the structural, electronic and magnetic properties of  $\text{Co}_2\text{FeAl}_{0.5}\text{Si}_{0.5}$  epitaxial films [174]. Cross-sectional transmission electron microscopy (TEM) was employed to determine the crystalline structures of the films. Bright field

images show that the sample has homogeneous roughness and thickness. Single-crystalline *B2* structure is confirmed by the selected area diffraction pattern. In 2006, Sakuraba et al. illustrated the correction between the crystallinity of Heusler alloy films and the TMR ratios [111]. Epitaxial and polycrystalline  $\text{Co}_2\text{MnAl}$  films were imaged using bright field cross-sectional TEM. It is important to mention that the interfacial roughness between the  $\text{Co}_2\text{MnAl}$  and  $\text{AlO}$  is greatly reduced for the epitaxial  $\text{Co}_2\text{MnAl}$  film. Electron diffraction patterns show the disordered *B2*. Temperature-dependant MR measurements were also performed from 10 to 300 K. In general, epitaxial  $\text{Co}_2\text{MnAl}$  shows about 15% higher MR ratio than the polycrystalline  $\text{Co}_2\text{MnAl}$ , confirming the importance of the crystalline ordering on the spin polarisation and the corresponding MR ratios. Yamada et al. demonstrated the interface crystallinity of  $\text{Co}_2\text{FeSi}$  as a function of growth temperature [175]. Two-dimensional epitaxial structure is observed at the growth temperature of 333, 403 and 473 K. However, at 403 and 473 K single-crystal phases are observed using cross-sectional TEM. Nanobeam diffraction confirms the phases may be  $\text{CsCl}$ - and/or  $\text{CaF}_2$ -type silicides such as nonmagnetic  $\text{CoSi}$ ,  $\text{FeSi}$  and/or  $\text{CoSi}_2$  [176].

These studies demonstrated structural characterisation on Heusler thin film samples using a cross-sectional TEM method. It also reveals the chemical distributions and crystalline ordering of the Heusler alloy films. However, some Heusler alloys form multiple phases instead of a single ordering structure, and their ratio is difficult to estimate.

### 4.3. Electrical resistivity

As the other macroscopic measure to assess the half-metallicity, electrical resistivity is commonly measured as a function of temperature,  $\rho(T)$ . In general, the temperature dependence of the resistivity can be written as  $\rho(T) = \rho(4\text{ K}) + c T^m$ , where  $m$  is an exponent factor. In a conventional FM metal, since one-magnon scattering (or electron-electron scattering) dominates

the resistivity at low temperature,  $m$  becomes 2 theoretically [177]. For HMF, due to the 100% spin polarisation, the one-magnon scattering is suppressed by the factor of  $\exp(-\delta/k_B T)$  ( $\delta$  is energy bandgap for the minority spins at  $E_F$  and  $k_B$  is Boltzmann constant), leading to typically  $m = 1.5$  at low temperature. At a finite temperature, spin fluctuation activates the minority band and unconventional one-magnon scattering starts to happen, which is described as  $m = 3$ .

Experimentally,  $\rho(T)$  of an epitaxial  $\text{NiMnSb}$  film follows a  $T^{1.55}$  law below 100 K as listed in Table 3, which clearly indicates the absence of spin-flip electron diffusion due to the half-metallicity [84]. For the full-Heusler alloys, on the other hand,  $\rho(T)$  is observed to be almost constant at low temperature, while  $m$  is measured to be  $m = 1.5$  and  $(1.2 \pm 0.1)$  at a finite temperature below RT in single-crystal  $\text{Co}_2\text{MnGe}$  [104] and polycrystalline  $\text{Co}_2\text{MnGa}$  films [124], respectively.  $\text{Co}_2\text{CrAl}$  bulk similarly shows  $m = 3.15$  at low temperature but 1.33 above 35 K [134]. Epitaxial  $\text{Co}_2\text{FeAl}$  films show  $m = 2.6$  below 50 K but 1.3 above 100 K [129], and  $m = 4.2$  below 30 K but 1.5 above 115 K [130]. For  $\text{Co}_2\text{MnSi}$  films [117], a relationship of  $\rho(T) = T^2 + T^{4.5}$  is reported, which may consist of an electron-electron scattering term  $T^2$  and a two-magnon scattering term  $T^{4.5}$ . Such a departure from the ideal law observed in the full-Heusler alloys, especially at low temperature, is mainly attributed to the presence of grain boundaries in the films, for the case of the polycrystalline films in particular [116].

The residual resistivity ratio (RRR),  $\rho(300\text{ K})/\rho(4\text{ K})$ , can also be used to characterise the bulk properties of the half-metallic films. For  $\text{Co}_2\text{MnGa}$  [124] and  $\text{Co}_2\text{CrAl}$  [130], the normalised resistivity  $\rho(T)/\rho(4\text{ K})$  has been reported to decrease monotonically with increasing  $T$ , providing RRR to be less than 1, which is common for a highly resistive material, such as an intrinsic semiconductor. For most of the Heusler films, RRR is obtained to be approximately 1.3, e.g., 1.28 for a single-crystal  $\text{Co}_2\text{MnGe}$  film [104] and 1.3 for epitaxial  $L2_1$   $\text{Co}_2\text{FeAl}$  film [130], which is much smaller than that observed for a  $\text{Co}_2\text{MnSi}$  bulk single crystal (6.5)

**Table 3.** List of exponent factors in the temperature dependence of the electrical resistivity  $\rho(T) = \rho(4\text{ K}) + c T^m$  for both half- and full-Heusler alloys. The residual resistivities (RRR)  $\rho(T)/\rho(4\text{ K})$  are also shown.

	$m$ at low temperature	$m$ at high temperature	RRR	Refs.
Theory	1.5 (HMF) 2.0 (conventional FM)	3.0 (non-rigid band) 4.5 (rigid band)		[177]
$\text{NiMnSb}$	1.55 (< 100 K)			epi- $C1_b$ -MBE film/V seed/MgO(001) sub. [84]
$\text{Co}_2\text{MnGe}$	0 (< 50 K)	$\sim 1.5$ (> 50 K)	$\sim 1.28$	epi- $B2$ -MBE film/GaAs(001) sub. [101]
$\text{Co}_2\text{MnGa}$	0 (< 100 K) 2.1 (< 60 K)	$(1.2 \pm 0.1)$ (> 200 K) 1.31	1.15 ~ 1.7 2.47	poly- $(B2)$ -MBE film/GaAs(001) sub. [124] Bulk [178]
$\text{Co}_2\text{Cr}_{0.6}\text{Fe}_{0.4}\text{Al}$	2.6 (< 50 K)	1.3 (> 100 K)		epi- $(B2)$ -sputtered film/MgO(001) sub. [129]
$\text{Co}_2\text{CrAl}$	3.15 (< 35 K)	1.33 (> 35 K)	1.1 < 1	$L2_1$ -bulk [134] poly- $B2$ -MBE film/GaAs(001) sub, [130]
$\text{Co}_2\text{FeAl}$	2.6 (< 50 K) 4.2 (< 30 K)	1.3 (> 100 K) 1.5 (> 115 K)	1.3	epi- $(B2)$ -sputtered film/MgO(001) sub. [129] epi- $L2_1$ -MBE film/GaAs(001) sub. [130]
$\text{Co}_2\text{MnSi}$		2.22 (> 75 K) 4.5 (> 100 K)	6.5 1.367 1.41	single-crystal bulk [116] $L2_1$ -bulk [179] poly- $L2_1$ -sputtered film/ $a$ - $\text{Al}_2\text{O}_3$ (0001) sub. [117]
$\text{Co}_2\text{FeSi}$	2 (< 100 K) 3.5 (< 70 K)	1.65 (> 70 K)	1.5	epi- $L2_1$ -sputtered film/MgO(001) sub. and $\text{Al}_2\text{O}_3$ (11-20) sub. [149]
$\text{Co}_2\text{TiAl}$	2 (< 100 K)		4.2	$L2_1$ -bulk [157]

[116] and for  $\text{Co}_2\text{TiAl}$  bulk (4.2) [157]. Since a very large RRR is reported for the bulk single crystal due to the improvement of the crystallinity of the alloy at low temperature, small RRRs for the Heusler films may indicate the stable crystallinity against temperature change. By comparing RRR with the  $\rho(T)$ , an epitaxial Heusler alloy film without grain boundaries is expected to show the ideal  $\rho(T)$  behaviour.

#### 4.4. X-ray magnetic circular dichroism

As a direct method to estimate the element specific magnetic moments per atom, X-ray magnetic circular dichroism (XMCD) has been exploited. XMCD measurements are performed at the  $L_2$  and  $L_3$  absorption edges of the constituent elements of the Heusler alloys, which represent the X-ray-induced excitation from the  $2p_{1/2}$  and  $2p_{3/2}$  core levels into the valence  $d$  states, respectively [180]. A magnetic field is applied perpendicular to the sample films, realising the magnetisation of the samples to be aligned parallel (or antiparallel) to the incident circularly polarised X-rays. These two configurations provide the corresponding X-ray absorption spectra, both of which are measured by the total electron yield method, revealing the difference in the population between up and down spin electrons. The difference in absorption cross-sections represents the XMCD signals as a result. Since the orbital part of the atomic wavefunction interacts with the circularly polarised X-rays [181], which indirectly interact with the spins of the atoms through the spin-orbit interaction [182], non-zero XMCD signals can be observed in the vicinity of the  $L_2$  and  $L_3$  edges. By applying the sum rules [181–183] after relevant background subtraction, element specific spin magnetic moments per atom  $m_{\text{spin}}$  are estimated as listed in Table 4.

##### (i) Bulk properties

For NiMnSb [84],  $\text{Co}_2\text{MnGa}$  [124],  $\text{Co}_2\text{MnSi}$  [149] and  $\text{Co}_2\text{FeSi}$  [196],  $m_{\text{spin}}$  for both Co and Y atoms show good agreement with theoretical calculations as listed in Table 4. On the contrary, for  $\text{Co}_2(\text{Cr,Fe})\text{Al}$ ,  $m_{\text{spin}}$  for Co maintains the good agreement, while that for Y (Cr and Fe) decreases significantly as compared with the calculations. For the latter cases, the enhancement in  $m_{\text{orb}}$  is reported in general. It should be emphasised that the  $m_{\text{orb}}$  for Co in the epitaxial films is observed to be twice as large as the calculation [130]. Similar enhancement in  $m_{\text{orb}}$  for Co has also been reported in a  $\text{Co}_2\text{MnGe}$  bulk sample [125]. Such enhancement in  $m_{\text{orb}}$  for the transition metals X and Y suggests that the spin-orbit coupling in the Heusler alloys are very strong and may be the main reason to induce the half-metallicity.

##### (ii) Heusler alloy/tunnel barrier interfaces

Because the XMCD measurement is sensitive to the surface of the sample, typically probing within 10 nm from the surface, the measurement always suffers from the overlap of the surface signals with the bulk signals. For films, the asymmetry and dislocation in the vicinity of the interfaces between the Heusler alloy layers and the capping layers, which are usually deposited to prevent oxidation, reduce  $m_{\text{spin}}$ . The samples can be capped with 3 ~ 4 nm oxide layers to mimic the interface between a FM Heusler alloy layer and an oxide tunnelling barrier. In 20 nm  $\text{Co}_2\text{Cr}_{0.6}\text{Fe}_{0.4}\text{Al}$  with a 3 nm MgO epitaxial capping layer, the X-ray absorption spectroscopy (XAS) spectra for both Cr and Fe possess minor splits in the peaks, corresponding to the oxidation of these elements [130]. For Co, on the other hand, no peak splitting is observed and the spin moment per atom is estimated to be  $1.09 \mu_B$ , which almost agrees with the calculated value ( $0.96 \mu_B$ ) [138]. For 20 nm  $\text{Co}_2\text{FeAl}$  with a 4 nm cap, the spin moment per Co atom also show more than 80% of the calculated value, while that of Fe only satisfy less than 50% of the calculation [135]. These results suggest that the epitaxial  $L2_1 \text{Co}_2\text{Cr}_{1-x}\text{Fe}_x\text{Al}$  films suffer from element selective oxidation at the interface with an oxide tunnel barrier and selective atomic disorder for Fe and Al, resulting in the decrease in the spin magnetic moments for Cr and Fe.

An epitaxial  $L2_1 \text{Co}_2\text{Cr}_{0.6}\text{Fe}_{0.4}\text{Al}$  film has been prepared onto  $\text{Al}_2\text{O}_3(11-20)$  and  $\text{MgO}(001)$  substrates with an Fe buffer layer by sputtering [192]. For both cases, the spin moment for Co only shows about 15% decrease as compared with the theoretical calculations [144], while that for Cr and Fe shows almost 90% and 30% decrease. This decrease is also attributed to the atomic disorder between Co and Cr/Fe atoms.

Elmers et al. have reported the orbital magnetic moment per spin,  $r = m_{\text{orb}}/(m_{\text{spin}} + m_{\text{dipole}})$ , to be  $(0.14 \pm 0.02)$  for Co and  $(0.06 \pm 0.02)$  for Fe in the  $\text{Co}_2\text{FeAl}$  bulk samples [138,139]. For the  $L2_1$  epitaxial  $\text{Co}_2\text{FeAl}$  films, by neglecting the magnetic dipole term,  $m_{\text{dipole}}$ ,  $r$  is estimated to be  $(0.098 \pm 0.007)$  and  $(0.069 \pm 0.005)$  for Co and Fe, respectively [135]. These values imply that Co does not show any enhancement in  $m_{\text{orb}}$ , while Fe shows similar enhancement as the bulk. Even so, it should be emphasised that  $m_{\text{orb}}$  for Co in the epitaxial films is observed to be twice as large as the calculation (see Table 4). Similar enhancement in  $m_{\text{orb}}$  for Co has been reported in a  $\text{Co}_2\text{MnGe}$  bulk sample [125]. Such enhancement in  $m_{\text{orb}}$  for the transition metals X and Y suggests that the spin-orbit coupling in the Heusler alloys are very strong and maybe the main reason to induce the half-metallicity. For sputtered  $\text{Co}_2\text{MnAl}$  film with the atomically disordered B2 structure, the Gilbert damping constant is found to be small by ferromagnetic

**Table 4.** List of element-specific magnetic moments per atom for both half- and full-Heusler alloys.

Heusler alloys		Total magnetic moment [ $\mu_B$ /f.u.]	X [ $\mu_B$ /atom]		Y [ $\mu_B$ /atom]		Refs.
			$m_{spin}$	$m_{orb}$	$m_{spin}$	$M_{orb}$	
NiMnSb	Exp. (f)	$3.9 \pm 0.2$	0.2		3.0		epi-C1 <sub>B</sub> -MBE film/V seed/MgO(001) sub. [84]
	Calc.	3.991	0.245	0.015	3.720	0.027	[88]
Co <sub>2</sub> MnGe	Exp. (b)	4.93 (RT)	~ 0.05	0.70	3.40	~ 0.03	poly-bulk [125]
	Exp. (b)	5.004 (RT)	0.975		~ 0.044		L <sub>21</sub> -bulk [184]
			1.04		2.44		[185]
Co <sub>2</sub> MnGa	Exp. (b)	3.01	0.52				L <sub>21</sub> -bulk [45]
	Exp. (b)	3.2					L <sub>21</sub> -poly-bulk [186]
	Exp. (b)	2.5					Poly (50 nm grains) [187]
	Exp. (f)		$0.534 \pm 0.050$		$0.175 \pm 0.016$		(1.5 ~ 1.7) nm Al/5.3 nm epi-L <sub>21</sub> -MBE-Co <sub>1.95</sub> Mn <sub>0.98</sub> Ga <sub>1</sub> /GaAs(001), Co <sub>2</sub> MnGa/GaAs interface [188]
			$0.470 \pm 0.051$		$0.34 \pm 0.036$		(1.5 ~ 1.7) nm Al/9.7 nm epi-L <sub>21</sub> -MBE-Co <sub>1.95</sub> Mn <sub>0.98</sub> Ga <sub>1</sub> /GaAs(001), Co <sub>2</sub> MnGa bulk [189]
	Calc.		2.91		0.65		[189]
Co <sub>2</sub> MnSi	Exp. (f)	4.7 (10 K)	$1.20 \pm 0.05$		~ 2.6		[84]
		5.1 (RT)	$1.20 \pm 0.05$	0.10 ± 0.02	~ 2.6	0.04 ± 0.02	epi-L <sub>21</sub> -PLD film/GaAs(001) sub. [119]
		4.7 (10 K)	1.1		1.7		1.4 nm Al-O/100 nm (011)-textured-sputtered Co <sub>2</sub> MnSi/Vbuffer/(SiO <sub>2</sub> )/Si sub. [190]
		4.8 (4 K)	1.07	0.04	2.46	0.05	epi-L <sub>21</sub> -sputtered film/MgO(001) sub. [149]
		4.8 (4 K)	1.13	0.14	2.47	0.10	epi-L <sub>21</sub> -sputtered film/Al <sub>2</sub> O <sub>3</sub> (11-20) sub. [149]
	Calc.	5.008	0.994	0.029	3.022	0.017	[88]
			1.021		2.971		[67]
		4.998 ~ 5.000	$1.08 \sim 1.158$		2.725 ~ 3.096		[191]
Co <sub>2</sub> Cr <sub>0.6</sub> Fe <sub>0.4</sub> Al	Exp. (b)	3.49 (5 K)	0.96	0.12	Cr: 0.40 Fe: 2.37	Cr: 0.04 Fe: 0.33	L <sub>21</sub> -bulk [138,139]
			0.86	0.04	Cr: 0.4 Fe: 2.17	Cr: 0.0 Fe: 0.09	L <sub>21</sub> -bulk [192]
		3.4 (5 K)	~ 1.2	~ 0.12	Cr: ~ 0.4 Fe: ~ 2.6	Cr: ~ 0.035 Fe: ~ 0.18	L <sub>21</sub> -bulk [144]
	Exp. (f)	2.26 (RT)	$1.09 \pm 0.11$	$0.038 \pm 0.004$	Cr: - Fe: -	Cr: - Fe: -	3 nm MgO/20 nm epi-L <sub>21</sub> -MBE film/GaAs(001) sub. [38]
			0.72	0.09	Cr: 0.2 Fe: 1.90	Cr: 0.04 Fe: 0.10	epi-L <sub>21</sub> -sputtered film/Fe buffer/MgO(001) sub. [192]
			0.74	0.08	Cr: 0.1 Fe: 1.90	Cr: 0.01 Fe: 0.10	epi-L <sub>21</sub> -sputtered film/Al <sub>2</sub> O <sub>3</sub> (11-20) sub. [192]
	Calc.		0.96		Cr: 1.52 Fe: 2.77		L <sub>21</sub> -bulk [192,196]
		3.56	0.86	0.042	Cr: 1.47 Fe: 2.59	Cr: 0.005 Fe: 0.082	[144]

(Continued)

Table 4. (Continued).

Heusler alloys	Total magnetic moment [ $\mu_B$ /f.u.]	X [ $\mu_B$ /atom]		Y [ $\mu_B$ /atom]		Refs.
		$m_{\text{spin}}$	$m_{\text{orb}}$	$m_{\text{spin}}$	$M_{\text{orb}}$	
$\text{Co}_2\text{Cr}_{0.623}\text{Fe}_{0.375}\text{Al}$	3.68 3.8 1.4 ~ 2.1 4.8 (5 K)	0.764 ~ 0.0923	0.021 ~ 0.048	Cr: 1.244 ~ 0.1537 Fe: 2.469 ~ 2.787	Cr: 0.001 ~ 0.0010 Fe: 0.028 ~ 0.083	[128] [193] [193]
$\text{Co}_2\text{FeAl}$	4.254 4.996 5.97 ± 0.05 5.33	0.91 ± 0.04 1.21 0.75 1.094 1.2 ± 0.1	0.089 ± 0.003 0.16 0.042 0.045	1.29 ± 0.05 1.83 2.70 2.753 2.0 ± 0.1	0.089 ± 0.005 0.24 0.070 0.060	4 nm $\text{SiO}_2/20$ nm epi- $L_{2_1}$ -MBE film/ $\text{GaAs}(001)$ sub. [130,135] Thin film on $\text{MgO}(001)$ [194] Thin film on $\text{MgO}(001)$ [195] [196] poly- $L_{2_1}$ -bulk [158] Bulk [197]
$\text{Co}_2\text{FeSi}$	56.2 ± 0.5 6.00	1.25	0.12	2.5	0.1	70 nm epi- $L_{2_1}$ -sputtered $\text{Co}_2\text{FeSi}(110)/\text{Al}_2\text{O}_3(11-20)$ sub. [196] $\text{Co}_2\text{FeSi}/\text{GaAs}(001)$ [154] [144]
$\text{Co}_2\text{TiSn}$ (bulk)	1.92 1.68	0.87 ± 0.02 0.90	0.09 ± 0.02	3.30		poly- $L_{2_1}$ -bulk [158] [158]
$\text{Co}_2\text{ZrSn}$ (bulk)	1.64 1.64	0.70 ± 0.01 0.88	0.012 ± 0.01			poly- $L_{2_1}$ -bulk [158] [158]
$\text{Co}_2\text{NbSn}$ (bulk)	0.94 1.08	0.38 ± 0.01 0.43	0.09 ± 0.01			poly- $L_{2_1}$ -bulk [158] [158]

resonance (FMR) measurement (see more details in Sec. 4.8), indeed indicating weak spin-orbit interaction for the disordered phases [113]. The large spin-orbit interaction in the Heusler alloys has also been suggested from a large AMR effect observed in polycrystalline  $\text{Co}_2\text{MnGa}$  film, as large as 6% at RT (8% at 1.6 K) [124].

(iii) Heusler alloy/substrate interfaces

Total (spin and orbital) moments of  $L_{2_1}$   $\text{Co}_2\text{MnGa}$  films epitaxially grown on  $\text{GaAs}(001)$  by MBE has been systematically investigated to specifically observe the difference between the bulk and interface regions [189]. They have maintained almost the same thickness for their capping layers (1.5 ~ 1.7 nm) for these samples with changing the Heusler layer thickness to be 5.3, 7.6 and 9.7 nm. For the first sample, they observe that the total moments for Co are less than 20% of the calculation (and also observation for bulk), while that for Mn is less than one-third of the calculation and bulk. For the last sample, on the other hand, they find slight recovery in the Mn total moment up to over 50% of the calculation and bulk. A similar tendency has also been found in off-stoichiometric samples. These results strongly suggest the presence of a magnetic dead layer in the Heusler alloy films near the  $\text{GaAs}$  interface.

Epitaxial  $L_{2_1}$  sputtered  $\text{Co}_2\text{FeSi}(110)$  on an  $\text{Al}_2\text{O}_3(11-20)$  substrate has been investigated by XMCD to reveal the thickness dependence of the element-specific magnetic moments [192]. They observe approximately 80% of the calculated spin moments for both Co and Fe atoms with the film thickness larger than 10 nm. In the vicinity of the  $\text{Al}_2\text{O}_3$  interface, a 0.8 nm thick magnetic dead layer is also found to be formed at RT.

4.5. Andreev reflection

Soulen et al. have first applied Andreev reflection to measure the spin-polarisation  $P$  of FM materials [36], and afterwards, this technique has been widely used to measure  $P$  of the Heusler alloys as listed in Tables 1 and Tables 2. This technique is based on the spectroscopic measurement in an FM/insulator/superconductor tunnelling junction developed by Tedrow and Meservey [198]. For the Andreev reflection, a superconducting point contact is used instead of a superconducting film, which allows to achieve spin-polarised electron injection into an FM film with forming a coherent pair with an oppositely spin-polarised electron in FM, while reflecting an Andreev hole back to the superconductor. This process occurs in addition to the conventional ohmic response at the interface. HMF with  $P = 100\%$ , however, cannot offer the coherent pair when the majority spin is injected from the point contact due to the absence of the



minority spins at  $E_F$ . Although this is a very powerful technique to measure  $P$  directly, the estimated  $P$  typically reflects the spin DOS in the vicinity of the surface.

Shigeta et al. have reported the spin polarisation of  $\text{Ru}_{2-x}\text{Fe}_x\text{CrSi}$  Heusler alloys using the Andreev reflection [199]. Apart from determination of the spin polarisation, it also shows the structural ordering of  $\text{RuFeCrSi}$  depends on the Fe and Ru content. For  $0.1 \leq x < 1.8$ , the  $L2_1$  ordering is confirmed, whilst for  $x = 1.8$ , the crystalline structure becomes  $B2$  [200,201]. The spin polarisation of  $x = 1.5$  and  $1.7$  is measured to be  $P = 53$  and  $52\%$ , respectively. Shigeta et al. also determined the spin polarisation of  $\text{Co}_2\text{FeSi}$ , which is integrated with superconductor NbN on a MgO substrate. The average spin polarisation of  $\text{Co}_2\text{FeSi}$  is reported to be  $(52 \pm 2)\%$ . Similar study on the other Co-based Heusler alloy, bulk  $\text{Co}_2\text{FeGa}$  with the  $L2_1$  ordering, is reported by Zhang et al. [178]. XRD measurement is undertaken for the bulk sample. The spin polarisation is measured to be  $P = 59\%$ . Recent study has also reported spin polarisation of  $(54 \pm 2)\%$  at clean  $\text{Co}_2\text{FeSi}/\text{Nb}$  interface in CPP-GMR-type junctions [202].

#### 4.6. Bandgap measurements

Resolving the true bandgap of the half-metallic Heusler alloys was long a significant challenge due to the spin-dependent nature of the gap. The gap could only be estimated by Andreev reflection (see Section 4.5), which are limited by the interfacial quality. Alhuwaymel et al. successfully showed a new technique for determining the spin bandgap using circularly polarised infrared (IR) radiation [68]. By sweeping the IR energy spectrum with an applied magnetic field both anti- and parallel to the polarisation of the radiation, the minority and majority bands can be probed independently. An absorption peak will be observed in only one orientation as the spin-polarised electrons which were excited by this radiation were absorbed by the bandgap of the Heusler alloy, in this case the full-Heusler alloys  $\text{Co}_2\text{FeSi}$  [68] and  $\text{Co}_2\text{FeAl}_{0.5}\text{Si}_{0.5}$  [203], with values of  $\sim 94$  and  $\sim 110$  meV were found, respectively.

Similarly, light absorption spectroscopy has been used by Schmitt et al. on thermoelectric materials such as  $\text{ZrNiSn}$  half-Heusler alloys [204]. By varying the composition, such as via Sc-doping the semi-conducting nature of the minority band can be switched from  $p$ - to  $n$ -type and the resulting bandgap observed. This highlighted several discrepancies with *ab initio* calculations due to hole/electron contributions, where a value of  $0.13$  eV compared to the theoretical value of  $0.5$  eV. These discrepancies are also in

observed in the method of Alhuwaymel et al., as well as the work of Aliev et al. [205], suggesting that there is much to be done in the true determination of half-metallic bandgaps.

#### 4.7. Gilbert damping constant

Gilbert damping constant  $\alpha$  is the friction coefficient of magnetisation motion, which affects the switching speed of magnetisation reversal process. From a technological point of view, small  $\alpha$  is required to reduce the switching current density  $J_c$  for the current-induced magnetisation switching process, because  $J_c$  is proportional to  $\alpha$  [206]. According to the torque-correlation model proposed by Kambersky [207],  $\alpha$  is proportional to the density of states, DOS, at  $E_F$ . Therefore, it is expected that half-metallic materials which have an energy gap in one spin channel exhibit relatively small  $\alpha$ . In experiments,  $\alpha$  can be evaluated using ferromagnetic resonance (FMR) [208], or time-resolved magneto-optical Kerr effect (TR-MOKE) [209]. Table 5 is a summary of reported values of  $\alpha$  in experiments for Heusler alloys. Many of those presented relatively small  $\alpha$  of less than  $0.01$ . Mizukami et al. discussed correlation between the calculated DOS and the experimentally determined relaxation frequency  $G$  ( $= \gamma\alpha M_s$ , where  $\gamma$  and  $M_s$  are gyromagnetic ratio and saturation magnetisation, respectively) for  $\text{Co}_2\text{FeAl}$  films with changing the degree of order for the  $B2$  phase,  $S_{B2}$ :  $G$  and the number of DOS at  $E_F$  exhibited similar trend on  $S_{B2}$  suggesting that the Gilbert damping is small half-metallic materials for which DOS is small at the  $E_F$  [210]. Similar discussion has been done for other compositions such as  $\text{CoFeGe}_{0.5}$  [211],  $\text{Co}_2(\text{Fe},\text{Mn})\text{Si}$  [212],  $\text{Co}_2\text{Mn}(\text{Al},\text{Si})$  [212],  $\text{Co}_2\text{MnSi}$  [213],  $\text{CoFeMnSi}$  [214] and so on. Recently, quite small  $\alpha$  of less than  $0.001$  has been experimentally demonstrated for  $\text{Co}_2\text{MnSi}$  films

**Table 5.** List of Gilbert damping constant  $\alpha$  reported for Heusler alloy films.

Material	Structure	Thickness (nm)	$\alpha$	Method	Reference
$\text{Co}_2\text{MnSi}$	$L2_1$	30	0.005	FMR	[212,218]
		5	0.03		
$\text{Co}_{1.9}\text{Mn}_{1.1}\text{Si}$	$L2_1$	30	0.002	TR-MOKE	[219]
		30	0.0007	FMR	[213]
		10	0.0007	FMR	[215]
$\text{Co}_2\text{FeSi}$	$L2_1$	30	0.022	FMR	[212,218]
		3	0.02		[220]
		20	0.0018	FMR	[221]
		20	0.0012	FMR	[221]
$\text{Fe}_2\text{CoSi}$	$L2_1$	20	0.0019	FMR	[221]
$\text{Co}_2\text{Fe}_{0.4}\text{Mn}_{0.6}\text{Si}$	$L2_1$	30	0.004	FMR	[212,218]
		3	0.013		[220]
$\text{CoFeGe}_{0.5}$	$B2$	50	0.0025	FMR	[211]
$\text{Co}_2\text{FeAl}$	$L2_1$	50	0.001	FMR	[210]
		140	0.005	FMR	[222]
		50	0.003	FMR	[223]
		$B2$ and $A2$	1	$\sim 0.015$	TR-MOKE
$\text{Ni}_2\text{MnSn}$	$L2_1$	40	0.0075	FMR	[225]
$\text{CoFeMnSi}$	$L2_1$	10	0.0027	FMR	[214]

[213,215], which is done by improving the degree of  $L2_1$  order possibly resulting in the improvement of the half-metallic property. The small  $\alpha$  of the Heusler alloy films is suitable for reducing  $J_c$  of the current-induced magnetisation switching phenomena as well as for applying to a channel layer of spin-wave propagation experiments [216,217].

#### 4.8. Nuclear magnetic resonance

Nuclear magnetic resonance (NMR) is based on the interaction between the spin of a nucleus with the surrounding fields, such as external magnetic field, neighbouring nuclei, surrounding electrons of the nucleus, and surrounding electrons of neighbouring atoms [226,227]. NMR is a good probe to characterise the local information of Heusler alloys. Because the shape of resonance spectrum is sensitive to the change of hyperfine field reflecting the local environment. Chemical degree of order as well as the chemical composition can be quantitatively evaluated using NMR: *e.g.*, Wurmehl et al. carried out an NMR study on  $\text{Co}_2\text{Mn}_{1-x}\text{Fe}_x\text{Si}$  Heusler alloys with several Fe composition  $x$  in the bulk samples, and quantitatively evaluated the chemical ordering especially focusing on the distribution of Fe-Mn atoms using spin-echo NMR of  $^{55}\text{Mn}$  nuclei [228]. The chemical ordering between Fe and Mn is not easy to characterise using, *e.g.*, laboratory X-rays because the atomic numbers of those are close each other, thus NMR is useful for characterising Heusler alloys which often consists of atoms with similar atomic numbers. For further detail of NMR study on Heusler alloys, review articles are found in refs. [229,230].

#### 4.9. Mössbauer spectroscopy

Mössbauer spectroscopy is a spectroscopic technique on resonant absorption of  $\gamma$ -ray by nuclei in solids, which provides information of local electronic states of the material. Experimental studies on Heusler alloys using Mössbauer spectroscopy have been reported since 1960's, in which bulk samples containing Sn or Fe, *e.g.*,  $\text{Co}_2\text{MnSn}$  [231],  $\text{Fe}_3\text{Sn}$  [232], were selected, because  $^{57}\text{Fe}$  and  $^{119}\text{Sn}$  isotopes are suitable for NMR measurements in laboratories. Heusler alloys of films forms have been also studied using Mössbauer spectroscopy in the last decade, which revealed local magnetic properties of ternary- and quarterly-Heusler alloy films quantitatively [233–235]. Mössbauer spectroscopy can be also applied for studies of interfaces in layered film samples, which is useful for optimisation of spintronic devices, because magnetic properties at the interface sensitively affect the spin-dependent transport in MTJs or CPP-GMR junctions. Tanaka et al. fabricated layered film samples consisting of a  $\text{MgO}/\text{Co}_2\text{FeGe}$  structure for MTJ application, using

molecular beam epitaxy technique. They controlled the metallic termination layer at the interface: Co-termination or  $^{57}\text{Fe}$ -Ge termination, and discussed hyperfine-field distribution at the  $^{57}\text{Fe}$  sites [236]. Similar study has also been done for metallic-layered films consisting of a  $\text{Co}_2\text{FeGe}/\text{Ag}$  structure for CPP-GMR junctions. The dependence on the deposition temperature of  $\text{Co}_2\text{FeGe}$  layer was discussed for the degree of order at the  $\text{Co}_2\text{FeGe}/\text{Ag}$  interface, which is consistent with the CPP-GMR ratios using similar sample structures [237]. Review articles of Refs. [230,238] are to be referred for further detailed studies on Heusler alloys using Mössbauer spectroscopy.

### 5. Applications of ferromagnetic Heusler alloys

#### 5.1. Spin injection

In order to achieve highly efficient spin injection from an FM film into a semiconductor or an NM metal, two distinct approaches have been proposed theoretically; spin injection from FM with almost 100% spin polarisation, such as HMF and DMS, in a diffusive regime [19], and that through a tunnel barrier in a ballistic regime [239]. For the former case, the Heusler alloy is one of the best candidates due to their good lattice matching with major semiconductors and their high  $T_C$  as discussed above. Diffusive spin injection holds a key to realise the spin-polarised three-terminal devices, such as a spin-polarised field-effect transistor [240] and a lateral spin-valve [241] at RT.

A  $\text{NiMnSb}(111)/\text{CdS}(111)$  interface is suggested to suppress the spin-flip electron transport at  $E_F$  [94], indicating the possible use of the  $\text{NiMnSb}$  film as a spin-filter to inject a spin-polarised electron current into the semiconductor. A similar effect is expected even for the electron transport in the (110) orientation in a non-half-metallic  $\text{Ni}_2\text{MnIn}/\text{InAs}$  interface, resulting in  $P \sim 80\%$  [168]. At this interface, only the electron spins within an energy of  $k_B T \approx 1/40$  eV at  $E_F$  in  $\text{Ni}_2\text{MnIn}$  are travelled into  $\text{InAs}$ .  $E_F$  must be close to the conduction band of  $\text{InAs}$  for the spins to fill these unoccupied states. Since the conduction minimum occurs at the  $\Gamma$  point, the transmittances for the minority spins are calculated to depend on the crystalline directions; 0.75, 0.82 and 0.99 for the [100], [110] and [111] directions, respectively. For the majority spins, on the other hand, the transmittances are calculated to be 0.19, 0.19 and 0.39 for the corresponding directions, respectively, since large spin-orbit scattering is expected at the interface to change the in-plane momentum to match an available state in  $\text{InAs}$ .

For the case of the  $\text{Co}_2\text{CrAl}/\text{III-V}$  semiconductor interfaces, the half-metallicity is calculated to be preserved for certain interfacial combinations. For  $\text{Co}_2\text{CrAl}/\text{GaAs}$  interfaces, the half-metallicity is preserved for the  $\text{Co}/\text{As}$  interface on the  $\text{GaAs}(001)$  surface and

for Al/As on GaAs(110), while it is demolished for CrAl/As on GaAs(001) [132]. For Co<sub>2</sub>CrAl/InP interfaces, the Cr spin moment is calculated to be enhanced for both the CrAl/In and CrAl/P interfaces ( $P \sim 63\%$  and  $65\%$ , respectively), while it is decreased for both the Co/In and Co/P interfaces ( $P \sim 56\%$  and  $\sim 74\%$ , respectively), even though the Cr spin moment is almost the same as the bulk value for both cases [133].

Experimentally, spin injection has been reported in a Co<sub>2.4</sub>Mn<sub>1.6</sub>Ga/InGaAs quantum well (QW) structure [123]. Although  $P$  is measured to be  $\sim 50\%$  by the Andreev reflection, the injected electron spin polarisation is estimated to be  $13\%$  at  $5\text{ K}$ , which is smaller than that for an Fe/InAs QW. It is therefore essential to fabricate a sharp Heusler alloy/semiconductor interface with a relevant band matching as theoretically proposed in order to achieve highly efficient spin injection.

In a lateral spin-valve structure, Co<sub>2</sub>FeSi has been used as an FM injector into Cu, achieving  $27\%$  spin injection efficiency [242]. This is the highest efficiency reported to date based on the optimised fabrication technique.

## 5.2. Anisotropic magnetoresistance effect

A recent theoretical work predicts that a sign of an anisotropic magnetoresistance (AMR) ratio of half-metallic materials is negative [243]. An AMR ratio effect has been systematically investigated in Co<sub>2</sub>MnZ and Co<sub>2</sub>FeZ ( $Z = \text{Al, Si, Ge and Ga}$ ) epitaxial films [244]. The sign of an AMR ratio is negative when the total valence electron number is between  $28.2$  and  $30.3$ , while that is positive when the total valence electron number is below  $28.2$  and above  $30.3$ . These findings indicate that  $E_F$  overlaps with the valence or conduction band edges of half-metallic gap with the valence electron number to be either  $\sim 28.2$  or  $30.3$ , respectively. Half-Heusler NiMnSb epitaxial films also show a negative AMR ratio [245,246]. Recently, a further study has been achieved by Sato et al. on epitaxial Co<sub>*x*</sub>(Mn<sub>0.44</sub>Ga<sub>0.56</sub>)<sub>100-*x*</sub> thin films. The Co composition of  $x$  was controlled between  $47.4$  and  $52.6$  at%. The corresponding AMR ratios were measured by changing the electric current relative to the magnetic field directions between  $5$  and  $300\text{ K}$ . The results show that the sign of the AMR ratios changes according to the current directions. The maximum AMR ratio is obtained at  $x = 49.7$  at% [247]. AMR can be used as a way to optimise a composition of half-metallic Heusler alloys for the RT half-metallicity. The magnitude of the negative AMR ratio gradually increases with shifting  $E_F$  away from the gap edges.

## 5.3. Giant magnetoresistive junctions

### 5.3.1. In-plane magnetic anisotropy

(i) *Half-Heusler alloys.* GMR junctions with FM Heusler alloy films have been studied over the last

decades to achieve the requirement for the next-generation magnetic storage and memory [248] as shown in Figure 1. Both current-in-plane (CIP) and current-perpendicular-to-the-plane (CPP) GMR have been investigated with [NiMnSb/Cu]<sub>10</sub>, [NiMnSb/Cu]<sub>10</sub>, NiMnSb/Cu/Ni<sub>0.80</sub>Fe<sub>0.20</sub> (or NiMnSb/FeMn) and NiMnSb/Cu/Ni<sub>0.80</sub>Fe<sub>0.20</sub> (or NiMnSb/FeMn) [249,250]. The former multilayers show a CPP-GMR ratio of  $4.5\%$  at  $4.2\text{ K}$ . The latter spin-valves show a CPP-GMR ratio of  $7.2\%$  at  $4.2\text{ K}$ .

Similar progress can be found for the GMR junctions with the half-Heusler alloy films. PtMnSb films are deposited on Al<sub>2</sub>O<sub>3</sub>(0001) by sputtering to form a spin-valve structure, PtMnSb(111)/CuMnSb(111)/PtMnSb(111)/MnFe, showing  $0.47\%$  GMR at RT [96]. This small GMR ratio may be due to the empty site disorder and interfacial defects. As discussed in Sec. 3.1, the terminations and crystalline directions of the Heusler alloy films can control the effective spin polarisation, which needs to be optimised in a junction. Recently, a CPP-GMR ratio of  $8\%$  at RT ( $21\%$  at  $4\text{ K}$ ) has been reported in fully epitaxial NiMnSb (20)/Ag (5)/NiMnSb (7) (thickness in nm) junctions with the (001) orientation [246]. The junctions achieve  $RA = (26 \pm 1) \times 10^{-3} \Omega \cdot \mu\text{m}^2$ . By repeating two sets of epitaxial GMR junctions, consisting of NiMnSb (9)/Ag (5)/NiMnSb (3)/Ag (5)/NiMnSb (9) (thickness in nm), further increase in the CPP-GMR ratio up to  $11\%$  ( $41\%$  at  $4\text{ K}$ ) has been reported by using a dual spacer [251]. Here,  $RA$  is found to be reduced to  $3.9 \times 10^{-3} \Omega \cdot \mu\text{m}^2$ , which is favourable for device applications as mentioned above.

(ii) *Full-Heusler alloys.* In 2001, a GMR junction, consisting of Co<sub>2</sub>MnGe (6)/V (1.6)/Co<sub>2</sub>MnGe (3)/Fe (0.3)/ZnSe (50)/GaAs(001) (thickness in nm) have been fabricated and measured along the two [110] directions [252]. The corresponding GMR ratio is measured to be less than  $1\%$ . Since then, a series of GMR junctions have been designed and evaluated, especially utilising an epitaxial film to achieve high crystalline ordering. Epitaxial films are typically deposited on a MgO(001) substrate with the crystalline relationship Co<sub>2</sub>Cr<sub>0.6</sub>Fe<sub>0.4</sub>Al(001)[100]||MgO(001)[110] or a Ag seed layer. For a CIP configuration, a multilayer of a [Co<sub>2</sub>Cr<sub>0.6</sub>Fe<sub>0.4</sub>Al (10)/Cu (2.5)/Fe<sub>0.1</sub>Co<sub>0.9</sub> (8.1)] stack (thickness in nm) has been used with showing only  $2\%$  GMR at RT ( $4\%$  at  $15\text{ K}$ ) [129]. Co-Fe-Al has then been used to show up to  $3.3\%$  CPP-GMR ratio at RT [253,254], followed by Co<sub>2</sub>MnSi with a Cr spacer with the CPP-GMR ratio of  $2.4\%$  and  $RA$  of  $19 \times 10^{-3} \Omega \cdot \mu\text{m}^2$  [255]. By replacing the Cr spacer with Cu to minimise the interfacial atomic diffusion and mixing, the CPP-GMR ratio is increased to  $8.6\%$  at RT ( $30.7\%$  at  $6\text{ K}$ ) [256]. In parallel, the Ag spacer has been commonly used, achieving a CPP-GMR ratio

of 6.9 (14)% at RT (6 K) using  $\text{Co}_2\text{FeAl}_{0.5}\text{Si}_{0.5}/\text{Ag}/\text{Co}_2\text{FeAl}_{0.5}\text{Si}_{0.5}$  [257]. Further enhancement has been reported for a CPP configuration, e.g.,  $\text{Co}_2\text{MnSi}$  (8.8)/Ag (5)/ $\text{Co}_2\text{MnSi}$  (8.8) (thickness in nm) with a GMR ratio and RA of 28.8% and  $3.1 \times 10^{-2} \Omega \cdot \mu\text{m}^2$  at RT, respectively [258], and  $\text{Co}_2\text{FeAl}_{0.5}\text{Si}_{0.5}$  (2.5)/Ag (5)/ $\text{Co}_2\text{FeAl}_{0.5}\text{Si}_{0.5}$  (2.5) (thickness in nm) with a GMR ratio and RA to be 34% (80% at 14 K) and  $1.5 \times 10^{-2} \Omega \cdot \mu\text{m}^2$  at 290 K, respectively [259].

In 2011, a large CPP-GMR ratio of 42% has been reported using  $\text{Co}_2\text{FeGe}_{0.5}\text{Ga}_{0.5}/\text{Ag}/\text{Co}_2\text{FeGe}_{0.5}\text{Ga}_{0.5}$  junctions [260], followed by the increase to 59.6 (200)% at RT (10 K) with a AgZn spacer [261]. Theoretically, a larger GMR ratios are expected, e.g., 90% and ~60% for  $L_{21}$ - and  $B2$ - $\text{Co}_2\text{MnAl}/\text{Ag}/\text{Co}_2\text{MnAl}$  junctions, respectively [262]. A  $\text{Co}_2\text{Fe}_{0.4}\text{Mn}_{0.6}\text{Si}/\text{Ag}/\text{Co}_2\text{Fe}_{0.4}\text{Mn}_{0.6}\text{Si}$  junction with the  $L_{21}$  ordering shows further increase in the CPP-GMR ratio of 74.8% with RA of  $(67.6 \sim 369.2) \times 10^{-3} \Omega \cdot \mu\text{m}^2$ .  $\text{Co}_2\text{Fe}_{0.4}\text{Mn}_{0.6}\text{Si}/\text{Ag}/\text{Co}_2\text{Fe}_{0.4}\text{Mn}_{0.6}\text{Si}$  shows a 58 (184)% GMR ratio at RT (30 K) [263,264]. Further improvement has been achieved by sandwiching the Ag spacer with NiAl as  $\text{Co}_2\text{Fe}(\text{Ga}_{0.5}\text{Ge}_{0.5})/\text{NiAl}/\text{Ag}/\text{NiAl}/\text{Co}_2\text{Fe}(\text{Ga}_{0.5}\text{Ge}_{0.5})$ , showing the GMR ratio of 82 (285)% at RT (10 K) and RA of  $4 \times 10^{-2} \Omega \cdot \mu\text{m}^2$  [265]. This is the largest GMR ratio reported to date, indicating that further improvement in the GMR should be achievable by controlling the interfacial smoothness without atomic defects in the junction to meet the roadmap produced by the IEEE Magnetics Society [39].

**(iii) Alternative spacers.** A  $L_{12}$   $\text{Ag}_3\text{Mg}$  spacer has been used in a CPP-GMR junction with epitaxial  $\text{Co}_2\text{Fe}_{0.4}\text{Mn}_{0.6}\text{Si}$  Heusler alloy films with <3% lattice matching [266]. The maximum RA and the GMR ratio are reported to be  $25 \times 10^{-3} \Omega \cdot \mu\text{m}^2$  and 63%, respectively, at RT. A review on CPP-GMR junctions with Heusler alloys can be found in Ref [267]. The counterpart approach from MTJ is described in Section 5.4.1(iii). Further reduction in RA has been achieved with In-Zn-O and 0.2 ~ 0.6 nm thick Ag insertion, which is similar to nano-oxide layer (NOL) structures demonstrated by Toshiba [268], showing RA ~ 0.1  $\Omega \cdot \mu\text{m}^2$  and an MR ratio of 32% [269].

### 5.3.2. Perpendicular magnetic anisotropy

Since the discovery of the perpendicular magnetic anisotropy (PMA) at an Fe/MgO interface [16,270–271], MgO layer insertion has been widely used to induce PMA, which is, however, not applicable for a GMR junction. Mn-based binary Heusler alloys are alternative choices [272]. Recently, a body-centred cubic (bcc) seed layer has been used to minimise the interfacial mixing with fcc Heusler alloy layer [273]. For a bcc vanadium seed layer, X-ray analysis shows that 25-nm-thick vanadium introduces a strong (110) orientation in the  $\text{Co}_2\text{FeSi}$

**Table 6.** List of measured saturation magnetisation ( $M_S$ ) and perpendicular magnetic anisotropy (PMA) for major Heusler alloys.

Heusler Alloys	$M_S$ (emu/cm <sup>3</sup> )	PMA (erg/cm <sup>3</sup> )	Refs.
$\text{Mn}_3\text{Ga}$	500	$1.5 \times 10^7$	[274]
$\text{Mn}_{2.5}\text{Ga}$	250	$1.2 \times 10^7$	[275]
$\text{Co}_2\text{FeAl}/\text{MgO}$	1000	$(2 \sim 3) \times 10^6$	[276]
	1100	$3.1 \times 10^6$	[277]
$\text{Co}_2\text{FeAl}/\text{MgAl}_2\text{O}_4$	731	$1.9 \times 10^6$	[278]
	1200	$4.2 \times 10^6$	[279]
$\text{V}/\text{Co}_2\text{FeSi}$	700	$1.75 \times 10^3$	[273]
$\text{W}/\text{WO}_3/\text{Co}_2\text{FeSi}$	400	$4.00 \times 10^3$	[280]
$\text{W}/\text{Co}_2\text{FeSi}$	600	–	[281]

Heusler alloy. The  $B2$ -texture of the  $\text{Co}_2\text{FeSi}$  is found to match that of the vanadium proving that the texture is defined by the seed layer. Reduction of the  $\text{Co}_2\text{FeSi}$  thickness is found to result in a reduction in the strength of the in-plane anisotropy, as expected from the cubic nature. Since the perpendicular magnetic anisotropy (PMA) is induced at the interface between  $\text{Co}_2\text{FeSi}$  and V, a second vanadium interface is added and found to increase the observed PMA. Further reduction in the thickness of the  $\text{Co}_2\text{FeSi}$  layer lead to an increase in the PMA where 4-nm-thick  $\text{Co}_2\text{FeSi}$  exhibited a strong PMA (see Table 6).

For further improvement in PMA, tungsten is selected due to the lower bulk resistivity of  $5.6 \times 10^{-6} \Omega \cdot \text{cm}$  [282], which is almost a half of that of vanadium ( $1.9 \times 10^{-5} \Omega \cdot \text{cm}$ ) [283]. High-temperature growth at 673 K is applied for tungsten, providing the (110) surface orientation as well [280,281]. The magnetisation of the  $\text{W}/\text{Co}_2\text{FeSi}$  sample is measured to be 400  $\text{emu}/\text{cm}^3$  with the perpendicular anisotropy of  $8 \times 10^5 \text{ erg}/\text{cm}^3$  as summarised in Table 6. Since the crystalline plane induced by the bcc seed layers is (110), which is a favourable orientation to promote the layer-by-layer crystallisation, low-temperature crystallisation has been demonstrated with PMA [281]. Samples consisting of  $\text{W}(10)/\text{Co}_2\text{FeAl}_{0.5}\text{Si}_{0.5}(12.5)/\text{W}(1.2)/\text{Co}_2\text{FeAl}_{0.5}\text{Si}_{0.5}(2.5)/\text{Ta}(2)$  (thickness in nm) have been deposited at 355 K for 2 min.  $M_S$  reaches ~1060  $\text{emu}/\text{cm}^3$ , which is almost 85% of the theoretically predicted value, and it is ideal for device implementation due to the low-temperature crystallisation. A GMR junction with an Ag spacer unfortunately shows only 0.03% at RT, which requires further optimisation for device implementation.

## 5.4. Magnetic tunnel junctions

### 5.4.1. In-plane magnetic anisotropy

As shown in Figure 11(a), TMR ratios have not been increased over 10 years since the report by Ikeda et al. with coherent tunnelling using a MgO barrier [16]. Great efforts have hence been devoted for the increase in the TMR ratios with half-metallic Heusler alloy films as detailed below.

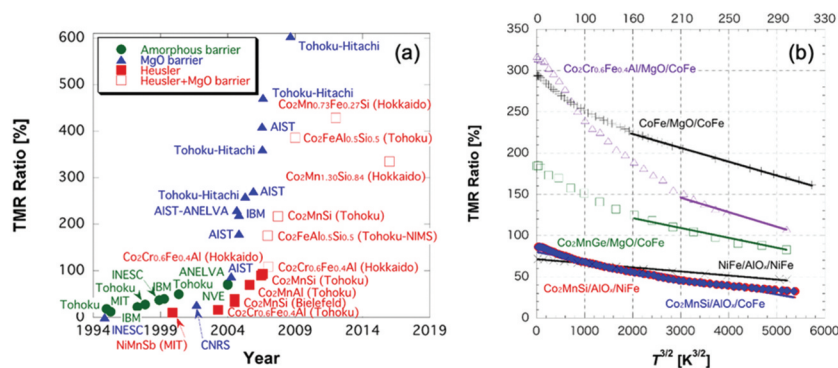


**Figure 11.** (a) Recent progress in TMR ratios with different junctions. (b) Temperature dependence of TMR ratios for MTJs with Co-based full Heusler alloy films. Experimental data are taken from Refs. [292] for Co<sub>2</sub>MnGe/MgO/CoFe, [293], for Co<sub>2</sub>Cr<sub>0.6</sub>Fe<sub>0.4</sub>Al/MgO/CoFe, [118] for Co<sub>2</sub>MnSi/Al-O/CoFe, [148] for Co<sub>2</sub>MnSi/Al-O/NiFe, [294] for Co<sub>2</sub>MnSi/Al-O/CoFe and Co<sub>2</sub>MnSi/MgO/CoFe, [290] for Co<sub>2</sub>FeAl<sub>0.5</sub>Si<sub>0.5</sub>/MgO/Co<sub>2</sub>FeAl<sub>0.5</sub>Si<sub>0.5</sub> and [295] for Co<sub>2</sub>Mn<sub>1.30</sub>Si<sub>0.84</sub>/MgO/Co<sub>2</sub>Mn<sub>1.30</sub>Si<sub>0.84</sub> as well as NiFe/Al-O/NiFe, [14] for CoFe/MgO/CoFe and [296] for CoFeB/MgO/CoFe.

**(i) Half-Heusler alloys** An epitaxial half Heusler NiMnSb film has been first used as an electrode in MTJ, showing 9% TMR at RT [77]. Apart from this pioneering work, very few studies were performed on MTJ with half-Heusler alloys.

**(ii) Full-Heusler alloys**

**(a) Co<sub>2</sub>(Cr,Fe)Z** An epitaxial full Heusler Co<sub>2</sub>FeAl film with the L<sub>21</sub> structure is also applied for MTJ but shows only 9% TMR at RT [130]. The small TMR ratios may be caused by the selective oxidation at the interface between the Heusler films and the oxide barriers according to XMCD measurements [38]. Recently, an epitaxial L<sub>21</sub> Co<sub>2</sub>Cr<sub>0.6</sub>Fe<sub>0.4</sub>Al film sputtered onto a MgO(001) substrate has been adopted for a fully epitaxial MTJ with the structure of Co<sub>2</sub>Cr<sub>0.6</sub>Fe<sub>0.4</sub>Al/MgO/CoFe, showing 42% at RT (74% at 55 K) [140]. Even though this film possesses the epitaxial relationship Co<sub>2</sub>Cr<sub>0.6</sub>Fe<sub>0.4</sub>Al(001)[100]||MgO(001)[110], the magnetic moment is estimated to be 3.3 μ<sub>B</sub>/f.u., which is smaller than the calculation (3.7 μ<sub>B</sub>/f.u.) [141]. This indicates that the film contains an atomically disordered phase, which may also be suggested from the decrease in the TMR ratios below 55 K. Further optimisation results in the TMR ratio to become 109% at RT and 317% at 4 K with RA ~ 3 × 10<sup>4</sup> Ω·μm<sup>2</sup> [284]. The TMR ratios have further been increased to 330% at RT (700% at 10 K) with RA = 1 × 10<sup>3</sup> Ω·μm<sup>2</sup> in MTJ with Co<sub>2</sub>FeAl/MgO/Co<sub>0.75</sub>Fe<sub>0.25</sub> by utilising the Δ<sub>1</sub>-band connection between Co<sub>2</sub>FeAl and MgO [285]. Using a MgAl<sub>2</sub>O<sub>4</sub> barrier instead of MgO to maintain the Δ<sub>1</sub>-band connection and to make better lattice matching with B<sub>2</sub>-Co<sub>2</sub>FeAl, TMR ratios are found to be increased to 342% at RT (616% at 4 K) with RA = 2.5 × 10<sup>3</sup> Ω·μm<sup>2</sup> [286]. The departure of the TMR ratios from theoretically predicted almost infinity may also be due to the interfacial atomic disorder, due to the presence of a light element of aluminium segregated from the matrix.

For polycrystalline sputtered full Heusler MTJs, on the other hand, much smaller TMR ratios have been reported. MTJ with the structure of Co<sub>2</sub>Cr<sub>0.6</sub>Fe<sub>0.4</sub>Al/

AlO<sub>x</sub>/CoFe shows 16% TMR at RT [73], which is later improved up to 19% at RT by the barrier optimisation [132]. By introducing a MgO underlayer, (001)-textured polycrystalline MTJs on a thermally oxidised Si substrate have been reported. MTJ with the structure of Co<sub>2</sub>FeAl<sub>0.5</sub>Si<sub>0.5</sub>/MgO/Co<sub>2</sub>FeAl<sub>0.5</sub>Si<sub>0.5</sub> shows 125% at RT and 196% at 7 K [287]. Later, an improved TMR of 175% was reported at RT using a Co<sub>2</sub>FeAl/MgO/CoFe structure [288].

By replacing a half of Al with Si in Co<sub>2</sub>FeAl to stabilise the crystallisation, MTJs with an oriented MgO barrier for which TMR ratios of 175% have been achieved at RT when using B<sub>2</sub>-Co<sub>2</sub>FeAl<sub>0.5</sub>Si<sub>0.5</sub> [280]. Using L<sub>21</sub>-Co<sub>2</sub>FeAl<sub>0.5</sub>Si<sub>0.5</sub>, the TMR ratios of 386% at RT and 832% at 9 K with RA = 80 × 10<sup>3</sup> Ω·μm<sup>2</sup> has been reported later [290]. The decrease in the TMR ratio with increasing temperature is much faster than the temperature dependence of the magnetisation T<sup>3/2</sup>, suggesting that a small fraction of atomically disordered phases cannot be ignored in the spin-polarised electron transport at finite temperatures [see Figure 11(b)] [291]. The elimination of such disordered interfacial phases improves the TMR ratios further and realises the half-metallicity at RT.

Theoretical calculations also suggest that the interface states within the half-metallic bandgap at the half-metal/insulator interfaces prevent the highly spin-polarised electron transport [296]. This is because the tunnelling rate is slower than the spin-flip rate, and therefore the interface states for the minority spins are effectively coupled to the metallic spin reservoir of the majority spin states. In order to avoid the spin-flip scattering, a sharp interface without the interface states is crucially required. Ležaić et al. discussed that the spin polarisation of half-metallic Heusler alloys can reduce significantly at temperatures much lower than their Curie temperatures even in bulk due to the change in hybridisation by spin fluctuation [297]. The other theoretical calculations revealed that an exchange stiffness constant of an interface at Co-based Heusler alloys and a MgO barrier is significantly

smaller than that of bulk [298]. Such a situation leads to serious reduction of an effective spin-polarisation at finite temperatures due to enhanced thermal fluctuation of spin moments, inducing the large temperature dependence of a TMR ratio [299]. In addition, large lattice mismatch between Co-based Heusler alloys and MgO, typically 5 ~ 7% for (001) growth, can easily introduce many misfit dislocations at the interface, which can cause suppression of the coherent tunnelling and increase the spin-flip scattering contribution [300]. Thus, introducing a larger exchange stiffness material at the interface, *e.g.*, ultrathin Co-Fe [301], and a smaller lattice-constant barrier, *e.g.*, MgAl<sub>2</sub>O<sub>4</sub> [302], can be a possible solution to improve an RT TMR ratio. These recent theoretical studies suggest that the elimination of interfacial states formed by lattice mismatch and atomic mixing can minimise the temperature dependence of the TMR ratios.

(b) *Co<sub>2</sub>MnZ* Similarly, an MTJ with Co<sub>2</sub>MnAl/Al-O/CoFe shows 40% TMR at RT [110], followed by the further improvement up to 61% at RT (83% at 2 K) [131]. All of these Heusler films in the MTJs have been reported to be B2 structure. By comparing the TMR ratios at RT with those at low temperature, the ratios are found to show very weak temperature dependence as similarly observed for a conventional metallic MTJ as shown in Figure 11.

An MTJ with an epitaxial L<sub>21</sub>-Co<sub>2</sub>MnSi film has been reported to show very large TMR ratios of 70% at RT and 159% at 2 K with RA = 10<sup>6</sup> Ω·μm<sup>2</sup> [122]. These values are the largest TMR ratios obtained in MTJ employing a Heusler alloy film and Al-O barrier. This is purely induced by the intrinsic *P* of the Heusler electrodes. These MTJs with a highly ordered Co<sub>2</sub>MnSi film show strong temperature dependence on the contrary to the less-ordered MTJs as discussed above; 33% at RT and 86% at 10 K [118], and 70% at RT and 159% at 2 K [122]. Such a rapid decrease in the TMR ratio with an increasing temperature is similar to that observed in MTJs with Co<sub>2</sub>(Cr,Fe)Al.

By replacing Al-O with MgO, a fully epitaxial MTJ, consisting of Co<sub>2</sub>MnSi/MgO/Co<sub>2</sub>MnSi, has been reported to achieve much higher TMR ratios, 217% at RT (753% at 2 K) [294] and 236% at RT (1,135% at 4 K), but with larger RA of 3 × 10<sup>7</sup> Ω·μm<sup>2</sup> [303]. Further improvements in the TMR ratio to be 354% at RT (1,995% at 4 K) have been achieved in the same system [304], followed by 366% at RT (2,110% at 4 K) with RA = 10<sup>8</sup> Ω·μm<sup>2</sup> [305]. Partial substitution of Mn with Fe in these MTJs to form Co<sub>2</sub>Mn<sub>0.73</sub>Fe<sub>0.27</sub>Si, TMR ratios are increased to 429% at RT (2,610% at 4 K) with RA = 7 × 10<sup>7</sup> Ω·μm<sup>2</sup> [306], which is the largest TMR ratio reported in a MTJ to date. A similar MTJ with Co<sub>2</sub>MnGe/MgO/Co<sub>2</sub>MnGe has been fabricated to show similar TMR ratios of 220% (650% at 4 K), but with large RA of 2.2 × 10<sup>6</sup> Ω·μm<sup>2</sup> [307]. The other Heusler alloys, such as CeFeMnSi, show much steeper temperature dependence of the TMR ratios, 101 and 521% at RT and 10 K, respectively [308]. The majority spin band with the Δ<sub>1</sub> symmetry near E<sub>F</sub> is calculated to be significantly modified by the Mn-Fe swapping disorder, opening an additional path for tunnelling and reducing the TMR ratio with elevating temperature. Such interfacial disorder may also be responsible for the strong temperature dependence.

(iii) *Alternative tunnelling barriers* For the RA reduction, alternative tunnelling barriers have been investigated. CuIn<sub>0.8</sub>Ga<sub>0.2</sub>Se<sub>2</sub> semiconducting barrier with almost perfect lattice matching with Co<sub>2</sub>FeGa<sub>0.5</sub>Ge<sub>0.5</sub> shows MR ratios of 40 and 100% at RT and 8 K, respectively, with RA of 0.3 ~ 3 Ω·μm<sup>2</sup> [309]. A CuGaSe<sub>2</sub> barrier shows MR ratios of 100 and 246% at RT and 30 K, respectively, with the RA < 1 Ω·μm<sup>2</sup> [310].

#### 5.4.2. Perpendicular magnetic anisotropy

##### (i) Binary Heusler alloys

By replacing Y atoms with X atoms, binary Heusler alloys can be formed. For example, Mn<sub>3</sub>Ga shows ferrimagnetic (FI) behaviour in the tetragonal D<sub>022</sub>-

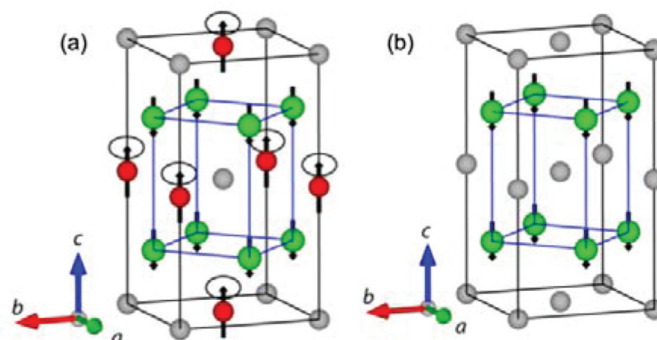


**Figure 12.** (a) The FI structure of D<sub>022</sub> Mn<sub>3</sub>Ga or D<sub>022</sub> Mn<sub>3</sub>Ge exhibiting overall c-axis anisotropy but with some in-plane component indicated by small circles. (b) FM structure of L<sub>10</sub> Mn<sub>3</sub>Ga with Mn atoms coupled ferromagnetically [314]. Reprinted with permission from Hirohata et al. [279]. Copyright 2018. MDPI AG.

phase with perpendicular magnetic anisotropy, as schematically shown in Figure 12(a). The FI  $\text{Mn}_3\text{Ga}$  has been reported to possess a large uniaxial anisotropy of  $1 \times 10^7 \text{ erg/cm}^3$  [311] and high Curie temperature of  $\sim 770 \text{ K}$  [312].  $\text{Mn}_3\text{Ga}$  has been used in an MTJ, consisting of  $\text{Mn}_3\text{Ga}/\text{MgO}/\text{CoFe}$  and has shown 9.8% TMR at 300 K with the perpendicular anisotropy of  $1.2 \times 10^7 \text{ erg/cm}^3$  [313].

The TMR ratio has then been improved by tailoring the interface using Co to be 40% at RT for the MTJ, consisting of  $\text{Mn}_{0.62}\text{Ga}_{0.38}$  (30)/Mg (0.4)/MgO (1.8)/CoFeB (1.2) (thickness in nm) [315,316]. Similar efforts have been devoted on polycrystalline MTJ consisting of  $\text{Mn}_3\text{Ge}/\text{MgO}/\text{CoFeB}$ , which shows a negative TMR ratio of  $-35$  and  $-75\%$  at 300 and 3 K, respectively, and low RA of  $10 \text{ } \Omega \cdot \mu\text{m}^2$  [317].

### (ii) MgO insertion

By inserting  $\text{Co}_2\text{MnSi}$  between Mn-Ga and MgO, the perpendicular anisotropy of the Mn-Ga layer can induce perpendicular anisotropy in the half-metallic  $\text{Co}_2\text{MnSi}$  layer, which is expected to achieve a large TMR ratio. Experimentally, TMR ratios of 10% at RT and 65% at 10 K have been achieved [318], which is smaller than the Mn-Ga/MgO/Mn-Ga junctions, as above. Additionally, the  $\text{Co}_2\text{MnSi}$  magnetisation is in tilted states during the reversal process, which causes the TMR curves to be not well defined.

Similar to the  $\text{CoFeB}/\text{MgO}/\text{CoFeB}$  systems, perpendicular anisotropy has been induced by attaching a MgO tunnel barrier. In a p-MTJ, consisting of  $\text{Co}_2\text{FeAl}/\text{MgO}/\text{Co}_{0.2}\text{Fe}_{0.6}\text{B}_{0.2}$ , a TMR ratio of 53% has been reported at RT [277]. By inserting a 0.1-nm-thick Fe ( $\text{Co}_{0.5}\text{Fe}_{0.5}$ ) layer between the MgO and  $\text{Co}_{0.2}\text{Fe}_{0.6}\text{B}_{0.2}$  layers, the TMR ratio was significantly enhanced to 91% (82%), due to the improved interface. The corresponding RA is  $1.31 \times 10^5 \text{ } \Omega \cdot \mu\text{m}^2$ . By further improving the MTJ quality, consisting of  $\text{Co}_2\text{FeAl}$  (1.2)/MgO (1.8)/Fe (0.1)/CoFeB (1.3) (thickness in nm), it has been reported to show TMR = 132% and RA =  $1 \times 10^6 \text{ } \Omega \cdot \mu\text{m}^2$  at RT [319].

By substituting some of Mg atoms, a  $\text{MgAl}_2\text{O}_4$  [320] and  $\text{MgGa}_2\text{O}_4$  [321] barrier can be formed, of which lattice constant matches perfectly with the Heusler alloy films. These spinel barriers show their corresponding TMR ratios with respect to their thickness. The height of  $\text{MgGa}_2\text{O}_4$  is found to be much lower than that of  $\text{MgAl}_2\text{O}_4$ . A  $\text{Co}_2\text{FeAl}/\text{MgAl}_2\text{O}_4$  epitaxial heterojunction with perpendicular anisotropy has been investigated for the understanding of the origin of the perpendicular magnetic anisotropy [322]. The strong anisotropy at the interface is attributed to (1) the

reduced in-plane magnetocrystalline anisotropy due to the lattice-matching and (2) the promoted hybridization between Fe and O orbitals due to the Al re-distribution near the interface.

### (iii) PMA seed layer

A perpendicularly magnetised seed layer has also been used to induce perpendicular anisotropy onto the Heusler alloy films. For example, MTJ stack with  $L1_0\text{-CoPt}/\text{Co}_2\text{MnSi}/\text{MgO}/\text{FePt}$  has been demonstrated [323], as similarly reported in a conventional  $\text{CoFeB}/\text{MgO}/\text{CoFeB}$  junctions.

## 6. Antiferromagnetic Heusler alloys

For an HDD read head and an MRAM cell, an AF layer has been traditionally used to pin one of the FM magnetisations to achieve a well-defined antiparallel magnetisation configuration. Additionally, AF spintronics has been widely studied based on spin polarisation induced by flowing an electrical current in an AF layer [324]. For these spintronic applications, an  $\text{IrMn}_3$  alloy has been predominantly used due to its corrosion resistance and robustness against device fabrication processes in nanometre-scale in both thickness and in-plane dimensions. However, due to the scarcity of Ir as a platinum group metal, the price of  $\text{IrMn}_3$  has risen over 10 times in the last decade [325].

For the development of a replacement for  $\text{IrMn}_3$ , RT antiferromagnetism needs to be achieved. However, the majority of the AF materials have their Néel temperature  $T_N$  near or below RT. Some oxides (e.g., NiO) and sulphides (e.g.,  $\text{CuFeS}_2$ ) have  $T_N > \text{RT}$  but they have very poor corrosion resistance and hence cannot be used in a device. Manganese alloys (e.g., NiMn and PtMn) and nitrides (e.g., MnN and  $\text{MnSiN}_2$ ) also have  $T_N > \text{RT}$ . However, NiMn has poor corrosion resistance and PtMn has very high crystallisation temperature, indicating that they cannot be used in a device either. Therefore, there is strong demand for a new AF Heusler alloy to be developed.

A list of major AF and compensated ferrimagnetic (CF) Heusler alloys is shown in Table 7. In Heusler alloys, half-Heusler alloys have low Néel temperatures in general. For example,  $\text{CuMnSb}$  [326],  $\text{NdBiFe}$  [327] and  $\text{GdPdBi}$  [328] have their  $T_N$  to be 55, 2.18 and 13 K, respectively. These are not suitable for Ir-Mn replacement in spintronic devices due to their low  $T_N < \text{RT}$  and due to the use of rare materials in the latter two alloys. Therefore, full-Heusler alloys have been focused for the development of AF films with their  $T_N > \text{RT}$ .

As listed in Table 7,  $\text{Fe}_2\text{VAL}$ , where Y and Z elements can be substituted with any other elements as listed in Figure 5, has been predicted to have a tendency to form a spin-glass (form AF ordering in  $\text{Fe}_{2.5}\text{V}_{0.5}\text{Al}$ ) [348,349].  $\text{Mn}_2\text{VAL}$  is analogous to  $\text{Fe}_2\text{VAL}$  but replaces the Fe with

**Table 7.** List of major AF and CF Heusler alloys and their Néel temperatures ( $T_N$ ), Curie temperatures ( $T_C$ ), average blocking temperatures ( $\langle T_B \rangle$ ), exchange biases ( $H_{ex}$ ) and their forms, bulk, epitaxial (epi.) or polycrystalline (poly.) films or calculations (calc.). Simulated results using molecular dynamics (MF) are also shown.

Heusler alloys	$T_N$ [K]	$T_C$ [K]	$\langle T_B \rangle$ [K]	$H_{ex}$ [Oe]	Forms	Refs.
CuMnSb	2				Bulk	[326]
NdBiFe	18				Bulk	[327]
GdPbBi	13				Bulk	[328]
Pt <sub>2</sub> MnGa	350	–			Bulk	[329]
Ru <sub>2</sub> MnGe	300	–			Bulk	[330]
	320	–	126	>81 (100 K)	Simulations	
	365	–			Epi. Films	[331]
Ru <sub>2</sub> MnSi	313	–			Calc.	[332]
	335	–			Calc.	
					Simulations	
Ru <sub>2</sub> MnSn	296	–				
Ru <sub>2</sub> MnSb	195	–				
Ni <sub>2</sub> MnAl	313	–			Bulk (B2)	[333]
	–	375			Bulk (L2 <sub>1</sub> )	
	245	–			Calc. (B2-I)	[334]
	350	–			Calc. (B2-II)	
	–	368			Calc. (L2 <sub>1</sub> )	
	340	–			Calc. (B2-I)	[335]
	372	–			MF Calc.	
	220	–			Calc. (B2-II)	
	352	–			MF Calc.	
	285	–			Calc. (B2-II)	
	310	–		>55 (10 K)	Epi. Films	[336]
Mn <sub>2</sub> VAI	>600	–			Bulk	[337]
	>RT	–	~200	120 (4 K)	Epi. Films	
				20 (RT)		
	360	–			Calc.	
	636	–			MF Calc.	
Mn <sub>2</sub> VSi		–	<100	34 (100 K)	Poly. Films	[338]
Mn <sub>3</sub> Ga	470	–			Bulk	[339]
	648	–	~400	1.5 k (RT)	Epi. Films	[340]
		–	235	430 (120 K)	Poly. Films	[341]
Mn <sub>3.04</sub> Ge <sub>0.96</sub>			390			[342]
						[343]
Mn <sub>3</sub> Ge						[344]
Mn <sub>2.4</sub> Pt <sub>0.6</sub> Ga	–	~90		33 k (2 K)	Bulk	[345]
				0 (90 K)		
Mn <sub>1.8</sub> FeGa	–	~350		12 k (2 K)		[351]
				~300 (RT)		
Mn <sub>2</sub> FeGa						[346]
Mn <sub>2.5</sub> Co <sub>0.3</sub> Ga <sub>1.2</sub>	–		>350	250 (RT)	Poly. films	
MnN	660	–	388	1475 (RT)	Poly. Films	[347]
	570	–			Calc.	
Fe <sub>2</sub> VAI					Calc.	[348]
					Poly. films	[349]
Cr <sub>2</sub> MnSb	342				Calc.	[169]

the very high moment Mn. These alloys can be further engineered by substituting some of Mn atoms with the other high-moment atoms to form (Co,Mn)<sub>2</sub>VAI for instance, which is analogous to the other two families with the exception that the element denoted X is now replaced by a mixture of two high moment atoms. By replacing V with Mn, low-moment-based alloys, e.g., Ni<sub>2</sub>MnAl, are anticipated to have a high compensated moment. By utilising a heavier element as a base of the Heusler alloys, Ru<sub>2</sub>MnAl is expected to have the potential advantage of having both X and Y as the high moment atoms. These families are anticipated to exhibit AF ordering. For RT antiferromagnetism, the AF phase should be stabilised by introducing larger anisotropy and larger AF grain volume. Recently, perpendicularly magnetised FM has also been reported to be pinned by IrMn layer [350]. Hence, the introduction of the additional tetragonal distortion into the cubic Heusler alloys may be necessary for the development of an RT AF.

### 6.1. Heavy-metal-based Heusler alloys

Epitaxially grown Ru<sub>2</sub>MnGe films have a very small lattice mismatch of 0.5% on a MgO(001) substrate with the relationship, Ru<sub>2</sub>MnGe[100](001)||MgO[110](001) ( $a_{Ru_2MnGe} = 0.5985$  nm,  $c_{Ru_2MnGe} = 0.6041$  nm and  $a_{MgO} = 0.5957$  nm). At a substrate temperature  $T_{sub} > 673$  K, the formation of epitaxial films has been reported [331] with the optimum growth temperature to be  $T_{sub} = 773$  K for the L<sub>21</sub> phase formation. For an epitaxial Ru<sub>2</sub>MnGe/Fe bilayer. The mean blocking temperature  $\langle T_B \rangle$  is measured to be 126 K using the York protocol [351].

First principle calculations with advanced classical spin model simulations support the Ru-based bilayers to show exchange bias for the L<sub>21</sub> phase [352]. Due to the strong FM coupling between the interface atoms, the Fe and Mn spins are oriented nearly parallel in the vicinity of their interface, and the direction of these



spins is in-plane following the in-plane magnetic anisotropy. The results confirm that the Ru-based Heusler alloys should be in the  $L2_1$  phase to exhibit AF behaviour. In order to increase the AF anisotropy and the resulting exchange bias  $H_{\text{ex}}$  induced in the neighbouring FM layer, calculations suggest that tetragonal distortion (stretching) can induce large uniaxial anisotropy in  $\text{Ru}_2\text{MnZ}$  due to a combined effect of symmetry breaking and spin-orbit coupling. A similar AF behaviour has been reported for the other heavy-metal-based Heusler alloys, such as  $\text{Pt}_2\text{MnGa}$  [340]. Therefore, for the heavy-metal-based Heusler alloys, high-moment element, *e.g.*, Mn, is necessary to induce AF behaviour. The AF anisotropy can be increased by introducing tetragonal distortion, leading to RT AF behaviour.

## 6.2. Transition-metal-based Heusler alloys

$\text{Ni}_2\text{MnAl}$  films grown on  $\text{MgO}(001)$  have been reported to form the  $L2_1$  and  $B2$  phase for 873 K and RT growth, respectively [337]. Only the latter phase exhibits the exchange bias onto a neighbouring FM layer with  $\langle T_{\text{B}} \rangle \leq 100$  K. Since the  $\text{Ni}_2\text{MnAl}$  layer has a number of crystalline defects causing the random distribution of crystalline boundaries, the formation of a larger grain size may be required to increase thermal stability for RT antiferromagnetism.

Atomistic calculations confirm that no exchange bias occurs [353], however, a partially disordered  $B2$  phase, a small  $H_{\text{ex}}$  has been found, which agrees with experiments as described above. Here, the disorder leads to uncompensated spin structures along the interface. Since the corresponding magnetic anisotropy is rather low (an order of magnitude smaller than that for the Ru-based Heusler alloys),  $H_{\text{ex}}$  is rather small and depends on the grain volume. It is furthermore rather unstable against thermal fluctuations with a maximum  $T_{\text{B}}$  of below 100 K as agreed with the experiment. Therefore, the Heusler alloys based with a transition metal with a small magnetic moment exhibits their AF phase when the high-moment Y atoms form antiparallel configuration between their second-nearest neighbours.

## 6.3 High-moment-metal-based Heusler alloys

As a Heusler alloy based with a transition metal with a high moment,  $\text{Mn}_2\text{VAl}$  films have been grown onto  $\text{MgO}(001)$  single-crystalline substrates with forming the  $L2_1$  and  $A2$  phase for  $T_{\text{sub}} \geq 773$  and  $\leq 673$  K, respectively. By depositing polycrystalline  $\text{Mn}_2\text{VAl}/\text{Fe}$  bilayer,  $H_{\text{ex}}$  of 120 Oe at 10 K has been measured [341], corresponding to  $\langle T_{\text{B}} \rangle \sim 75$  K.

Polarised neutron reflectivity (PNR) measurements confirmed the presence of an AF phase at RT in a polycrystalline  $A2$ -ordered  $\text{Mn}_2\text{VAl}$  bulk sample.

The  $\text{Mn}_2\text{VAl}$  film deposited at 673 K is similarly found to show AF  $A2$  phase at RT, while those deposited at RT and 873 K show the  $A2$  phase without AF ordering and the  $L2_1$  phase, respectively [336].

The ordered  $\text{Mn}_2\text{VAl}$  alloy has a FI ground state stabilised by a rather large V moment-oriented antiparallel to an Mn moment. According to atomistic calculations, the disorder between the V and Al atoms does not influence significantly the magnetic state as compared to the ordered  $L2_1$  state. The fully disordered  $A2$  phase is also studied as a random three-component alloy in terms of single-site coherent potential approximation (CPA), showing NM. Only by increasing the lattice parameter by more than 8%, a spontaneous FM state has been formed. The failure of obtaining an AF ground state (in fact, a magnetic ground state) at the experimental lattice constant indicates that magnetism collapses when a homogeneous atomic disorder is supposed like with the CPA and, most possibly, atomic short-range order (*e.g.*, clustering of Mn atoms) would stabilise the magnetic order in the system.

For the Mn-based Heusler alloys, off-stoichiometric compositions have also been investigated, which confirms the robustness of the Mn-based alloys against their atomic disorder. By taking two FI Heusler alloys,  $\text{Mn}_3\text{Ga}$  and  $\text{Mn}_2\text{PtGa}$ , their compensation point,  $\text{Mn}_{2.4}\text{Pt}_{0.6}\text{Ga}$ , has been calculated and demonstrated experimentally [345].

By further substituting Y elements with Mn, binary Heusler alloys can be formed. One example is hexagonal  $\text{Mn}_3\text{Ge}$  [343].  $H_{\text{ex}}$  of up to 520 Oe is measured at the boundaries between AF and FM domains. A tetragonal  $\text{Mn}_3\text{Ga}$  film has then been investigated to induce AF behaviour [339]. A bilayer of epitaxial  $\text{Mn}_3\text{Ga}$  (10 nm)/ $\text{Co}_{0.9}\text{Fe}_{0.1}$  (2.5 nm) is reported to show  $H_{\text{ex}}$  of 1.5 kOe at RT. Magnetic anisotropy energy and  $\langle T_{\text{B}} \rangle$  are estimated to be  $3 \times 10^6$  erg/cm<sup>3</sup> and  $\sim 400$  K, respectively. Recently,  $H_{\text{ex}}$  of 430 Oe at 120 K in polycrystalline  $\text{Mn}_3\text{Ga}/\text{Co}_{0.6}\text{Fe}_{0.4}$  bilayers, confirming the applicability of such binary Heusler alloys for a device [341]. Similar off-stoichiometric AF Heusler alloys are reported as  $\text{Fe}_2\text{VAl}$  [348,349] and  $\text{Cr}_2\text{MnSb}$  [169].

By further expanding the definition of the Heusler alloys to nitrides [330], MnN has been investigated. MnN films are grown using ultrahigh vacuum sputtering in  $\text{N}_2$  atmosphere to achieve Mn:N = 1:1. A MnN/Fe bilayer has been reported to show  $H_{\text{ex}}$  of 1.4 kOe at RT with  $\langle T_{\text{B}} \rangle = 388$  K [347]. However, the minimum thickness of MnN to induce the AF behaviour is 20 nm, which needs to be at least halved to be competitive against the 6-nm-thick Ir-Mn layer used in spintronic devices.

Therefore, high-moment-metal-based Heusler alloys display AF behaviour possibly due to the clustering of the high-moment metals even in their disordered  $A2$

phase. Magnetic anisotropy is demonstrated to be increased by introducing tetragonal distortion into the unit cell of the alloys. Further engineering in distortion and AF domain size can increase  $\langle T_B \rangle$  and  $H_{\text{ex}}$  of these alloys, allowing the replacement for Ir-Mn alloys used in spintronic devices.

## 7. Major characterisations techniques of antiferromagnetic Heusler alloys

### 7.1. Electrical resistivity

For the Néel temperature measurement, the temperature dependence of electrical resistivity has been utilised to determine  $T_N$  by detecting its gradient change [354]. Above  $T_N$ , the moment alignment becomes random in the AF materials and changes the corresponding resistivity. As an example, a single-crystal of Cr with dimensions  $5 \times 5 \times 1 \text{ mm}^3$  has been measured to confirm the applicability of the resistivity measurements to determine  $T_N$  in a thin-film form [325]. A clear minimum of the order of  $\mu\Omega$  is observed in the resistivity at 311 K. Measuring this change is only possible due to the low resistance of the crystal, e.g., 100-nm-thick epitaxial  $\text{Ni}_2\text{MnAl}$  films grown at elevating temperature [337].

### 7.2. X-ray magnetic linear dichroism

In order to characterise the AF materials microscopically, synchrotron radiation has been widely employed. X-ray magnetic linear dichroism (XMLD) utilises a pair of linearly polarised soft X-ray beams with perpendicular polarisation axes, which is different from a pair of circularly polarised beams used in XMCD as described in Sec. 4.4. Here, XMCD signals are proportional to the average value of a magnetic moment in a domain ( $\langle M \rangle$ ), while XMLD signals are proportional to  $\langle M^2 \rangle$ . For an AF material,  $\langle M \rangle$  is zero as  $M_A = -M_B$  within an AF domain in Eq. (2), resulting in no XMCD signal. However,  $\langle M^2 \rangle$  is a finite value for an AF material, allowing AF domain imaging. For example for an Fe/NiO bilayer, NiO domain structures have been observed by taking a Ni  $L$ -edge, which is strongly affected by the exchange coupling between Fe and NiO (spin image), and by taking the O  $K$ -edge, which is originated from the intrinsic AF anisotropy due to the strong coupling with the Ni  $3d$  orbital (twin image) [355]. For these domain imaging, a large uniform domain ( $> a \text{ few } \mu\text{m}$ ) is required, which makes it difficult to be used for an AF thin films.

### 7.3. Polarised neutron reflection

Polarised neutron reflectivity (PNR) is another synchrotron-based technique to determine magnetic properties of bulk and layered materials [356]. Due to the magnetic moment of neutron beam interacting with magnetic materials to be observed, not only layer structures, such as thickness, density, composition and

interfacial roughness, but also in-plane magnetic moments can be measured. The former structural analysis is similar to X-ray reflectivity (XRR) measurements but with higher accuracy in a shorter scanning period ( $< 1 \text{ min.}$ ). The latter magnetic information can be obtained by detecting the neutron reflection with its spins interacted with those in an AF and/or FM layers.

## 8. Applications of antiferromagnetic Heusler alloys

AF Heusler alloys are extremely attractive due to the absence of rare, expensive or toxic materials in their composition. Furthermore, they are fully compatible with other FM and NM Heusler alloys, with small lattice mismatches, large conduction band overlap and similar interfacial properties. Therefore, AF Heusler alloys are suitable for a wide range of applications, both for AF spintronics or as pinning layers in traditional spintronic devices.

A recent work by Nayak et al. has shown experimentally the existence of the anti-skyrmion in a tetragonal Heusler alloy  $\text{Mn}_{1.4}\text{Pt}_{0.9}\text{Pd}_{0.1}\text{Sn}$  with the  $D_{2d}$  symmetry [357]. Lorentz TEM was used to observe the formation of this new class of skyrmion, which is an alternating form of the previously observed Bloch and Néel skyrmions. These structures are stable at above RT in the presence of a small field (0.2 T) and can be meta-stabilised at lower temperatures in the absence of an applied field.

AF Heusler alloys have attracted great attention in the storage industry as a viable material for read/write heads and for ultra-low damping MRAM. All-Heusler GMR devices have been realised [358], these are yet to reach the necessary MR characteristics and Heusler alloy devices with non-Heusler alloy spacer layers require conditions which are not back-end-of-line (BEOL) compatible. However, many magnetoresistive properties could potentially be realised in an all-Heusler exchange-biased GMR/TMR device. The potential for half-metallic antiferromagnets [359–361] which will have lattice and energy-band matching to the rest of the device stack mean that AF Heusler alloys are an exciting avenue for device applications.

AF spintronics is one of the key avenues of investigation for the improvement of spintronic devices [362,363]: Increases in device density due to zero stray fields, radiation hardness against magnetic interference and ultra-fast magnetisation dynamics. These advantages indicate that AF spintronics can exceed the potential of conventional spintronics. Heusler alloys provide an exciting avenue within this new area due to their desirable properties. More specifically, it is the compensated ferromagnetic Heusler alloys, such as  $\text{Mn}_3\text{Ga}$ , which are of key interest [345,364].

The  $D0_{22}$  tetragonal Heusler alloys can be tuned compositionally to be fully compensated. The

advantages of this are that the dipole field is zero even at the atomic scale. Furthermore, with the tetragonal Heusler alloys the high  $T_C$  -500 K means that the magnetic order is thermally robust. With Mn-Fe-Ga alloys exchange bias fields of greater than 3 T have been established, further paving the way for application in both ferro- and antiferromagnetic spintronics.

## 9. Non-magnetic Heusler alloys

### 9.1. Topological insulators

Topological insulators are one of the Dirac materials which have a topological nontrivial band structure leading to unique quantum phenomena [365]. For example, Qi et al. have studied on a topological insulator  $\beta$ -Bi<sub>4</sub>I<sub>4</sub> by applying high pressure in order to obtain the quasi-one-dimension [366]. Hybrid functional method has been used to calculate the electronic properties to prevent the underestimated band gap within the local density approximation or generalised gradient approximation. The simulations show a weak interaction between the along the AFYM path and strong dispersion along the BF direction indicates a strong interaction within the chain. Therefore, quasi-1D characteristics of  $\beta$ -Bi<sub>4</sub>I<sub>4</sub> are confirmed. Density functional theory calculations show that electronic instability occurs at a critical pressure of 11.5 GPa. An experimental study on resistivity as a function of pressure shows a direct relationship between the resistivity and the bandgap stage (open or close). The resistivity decreases rapidly above the critical pressure and superconductivity is observed in  $\beta$ -Bi<sub>4</sub>I<sub>4</sub>.

A topological surface state has been reported in LuPtBi and YPtBi [369]. Angle-resolved photoemission spectroscopy (ARPES) measurements confirmed the formation of a topological phase with a clear Dirac point at the  $\Gamma$  position, which has been supported by *ab initio* calculations. Similar properties have been reported in ZrIrZ (Z = As, Sb or Bi) [368,369]. Experimental study and theoretical calculation have

been carried out to investigate the structural and magnetotransport properties of LuNiBi single crystals [370]. Further investigation on a topological state in Heusler alloys may be required for the search for a robust topological insulator.

### 9.2. Spin gap-less semiconductors

Some Heusler alloys have been studied due to the unique property such as spin-gapless semiconductor (SGS). This novel material was first proposal by Wang et al. [371]. There are four possible band structures with spin gapless features as shown in Figure 13. These Heusler alloys have potential applications in spintronic devices because of their unique transport properties. For instance, almost no threshold energy is required to excite electrons from the valence to conduction band, the excited electrons have spin polarisation of 100%. Several SGS Heusler alloys such as Fe<sub>2</sub>CoSi [372], Mn<sub>2</sub>CoAl [373–374] CoFeCrGa [375] and Zr<sub>2</sub>MnGa [376] have been studied.

More than 10 FeRu-based quaternary Heusler alloys have been studied by Guo et al. [378–380]. FeRuCrSi is predicted to be a spin gap-less semiconductor with 100% spin polarisation. The total magnetic moment is calculated to be 2.0  $\mu_B$  [377]. Type-II ScMnVGa is a spin gap-less semiconductor in Mn-based Heusler alloys. The absence of a magnetic moment is calculated for ScMnVGa, which represents antiferromagnetic behaviour. This calculation is achieved using first principles calculations based on density functional theory [378].

Xu et al. conducted detailed analysis on the magnetic properties of stoichiometric Mn<sub>2</sub>CoAl Heusler alloys. Saturation magnetisation at 5 K of the annealed stoichiometric and Co-rich Mn<sub>2</sub>CoAl samples are measured to be 2.6 and 2.5  $\mu_B$ /f.u. respectively [379]. Bainsla et al. studied the magnetic behaviour of CoFeCrGa with high Curie Temperature of 620 K [380]. The saturation

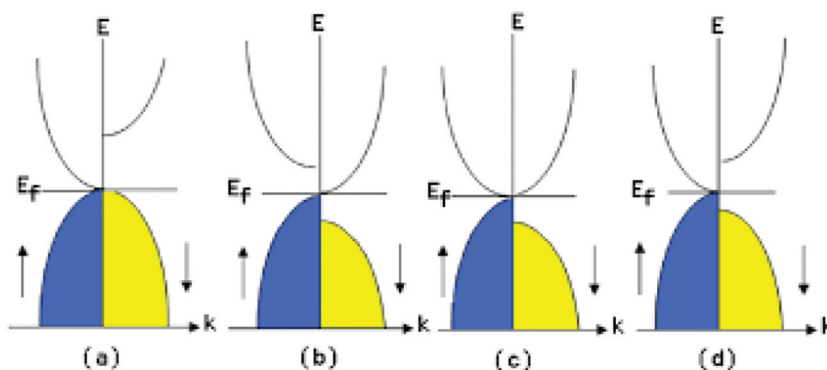


**Figure 13.** Four possible energy band structures for spin gapless semiconductors with parabolic dispersion energy against momentum [382].

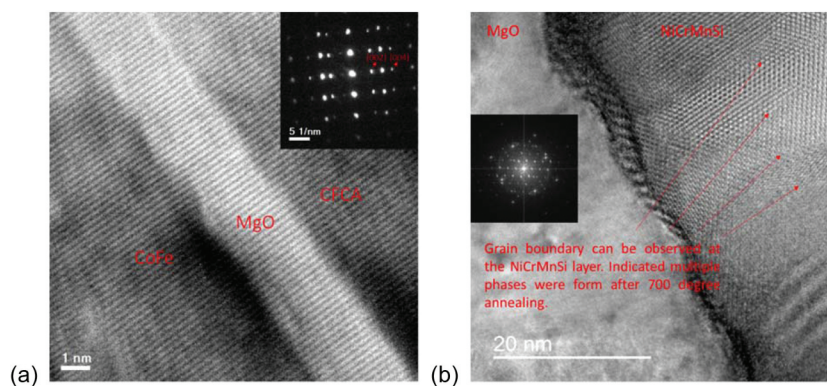


**Figure 14.** Cross-sectional TEM image of MTJ consisting of CoFeCrAl/MgO/CoFe and NiCrMnSi annealed at 973 K. Nanobeam diffraction patterns are also taken to confirm the crystalline ordering. Samples were grown by Mizukami et al. See Ref. [384] for details.

magnetisation of  $\approx 2.1 \mu_B/\text{f.u.}$  is measured under zero applied pressure [375]. This value was in good agreement of  $M_s = 2.0 \mu_B$  based on the generalised Slater-Pauling rule [65]. Fu et al. also studied magnetic properties of CoFeMnSi [381], as it has been predicted as a half-metallic ferromagnetic material [383]. The saturation magnetisation and coercivity are measured to be  $98.6 \text{ emu/g}$  ( $= 3.49 \mu_B/\text{f.u.}$ ) and less than  $25 \text{ Oe}$ , respectively. The SGS Heusler alloys show ferromagnetic behaviour and exhibit soft magnetic behaviour.

These SGS Heusler alloy films have been used as a ferromagnetic layer in MTJs. For example, CoFeCrAl acts as a ferromagnetic layer in MTJ, showing 87% TMR ratio at RT [384]. Thin film sample is grown using magnetron sputtering technique, followed by post-annealing at  $T_{\text{anneal}} = 1,073 \text{ K}$ . Cross-sectional TEM is performed to characterise the CoFeCrAl structure. Nanobeam diffraction confirms the chemical ordering of CoFeCrAl as shown in Figure 14(a) with very few interfacial dislocations. As discussed in Section 5.4., the TMR ratio of MTJ depends on various factors at the interface between ferromagnetic and insulator layers, such as the interface roughness and lattice mismatch [12]. The smooth interface induces a reasonably large TMR ratio. The diffraction spots of CoFeCrAl (002) and (004) are obtained, indicating that the CoFeCrAl exhibits the  $B2$  (instead of  $L2_1$ ) ordering which agreed with the XRD data [384].

As another example, NiCrMnSi is used to examine the change of crystallinity using different annealing temperatures. Figure 14(b) shows cross-sectional TEM and the corresponding fast Fourier transformation (FFT) images NiCrMnSi is deposited on a MgO(001) substrate, followed by *in-situ* annealing at  $T_{\text{sub}} = 973 \text{ K}$ . Diffraction pattern is also observed as an inset in Figure 14(b), indicating NiCrMnSi crystallisation.

## 10. Conclusion and future perspectives

The structural and magnetic properties of Heusler alloy films are explained from the viewpoint of spintronic applications. The crystallographical manipulation as well as spin-structural controllability can be achieved in the films by constituent element substitution. Recent progress in the film growth techniques enables the formation of almost perfectly ordered Heusler alloys. Local atomic disordering in the vicinity of their interface and surfaces prevents to achieve half-metallic electron transport at RT, which has been theoretically predicted for a bulk Heusler alloy. In order to achieve such surface asymmetry, first principles calculations and materials informatics using available databases [385],[386] have been employed to seek relevant combinations of interfacial atomic bonding, a surface termination and a crystalline orientation. Such an atomically controlled Heusler film is highly required for the use as a spin source for future spintronic devices.

## Acknowledgments

The authors would like to thank the financial support by EPSRC-JST Cooperative programme (EP/H026126/1), JST-EC DG RTD Coordinated research project (FP7-NMP3-SL-2013-604398), EPSRC-JSPS Core-to-Core programme (EP/M02458X/1) and JST CREST (JPMJCR17J5). The UK team has been supported by EPSRC grants (EP/I000933/1 and EP/K03278X/1) and Royal Society research grant.

## Disclosure statement

No potential conflict of interest was reported by the authors.

## Funding

This work was supported by the EPSRC-JSPS Core-to-Core programme [EP/M02458X/1]; JST-EC DG RTD Coordinated research project [FP7-NMP3-SL-2013-604398]; EPSRC [EP/

I000933/1 and EP/K03278X/1]; Royal Society research grant; JST CREST [JPMJCR17J5]; EPSRC-JST Cooperative programme [EP/H026126/1].

## ORCID

Atsufumi Hirohata  <http://orcid.org/0000-0001-9107-2330>

## References

- [1] Baibich MN, Broto JM, Fert A, et al. Giant Magnetoresistance of (001)Fe/(001)Cr Magnetic Superlattices. *Phys Rev Lett*. 1988;61:2472.
- [2] Binasch G, Grunberg P, Saurenbach F, et al. Enhanced magnetoresistance in layered magnetic structures with antiferromagnetic interlayer exchange. *Phys Rev B*. 1989;39:4828(R).
- [3] Hirohata A, Takanashi K. Future perspectives for spintronic devices. *J Phys D Appl Phys*. 2014;47:193001.
- [4] Fullerton EE, Schuller IK. The 2007 Nobel Prize in Physics: Magnetism and Transport at the Nanoscale. *ACS Nano*. 2007;1:384.
- [5] Terris BD, Thomson T. Nanofabricated and self-assembled magnetic structures as data storage media. *J Phys D Appl Phys*. 2005;38:R199.
- [6] Bhatti S, Sbiaa R, Hirohata A, et al. Spintronics based random access memory: A review. *Mater Today*. 2017;20:530.
- [7] Parkin SSP, Li ZG, Smith DJ. Giant magnetoresistance in antiferromagnetic Co/Cu multilayers. *Appl Phys Lett*. 1991;58:2710.
- [8] Jullière M. Tunneling between ferromagnetic films. *Phys Lett A*. 1975;54:225.
- [9] Miyazaki T, Tezuka N. Giant magnetic tunneling effect in Fe/Al<sub>2</sub>O<sub>3</sub>/Fe junction. *J Magn Magn Mater*. 1995;139:L231.
- [10] Moodera JS, Kinder LR, Wong TM, et al. Large Magnetoresistance at Room Temperature in Ferromagnetic Thin Film Tunnel Junctions. *Phys Rev Lett*. 1995;74:3273.
- [11] Wei HX, Qin QH, Ma M, et al. 80% tunneling magnetoresistance at room temperature for thin AlO barrier magnetic tunnel junction with CoFeB as free and reference layers. *J Appl Phys*. 2007;101:09B501.
- [12] Butler WH, Zhang X-G, Schulthess TC, et al. Spin-dependent tunneling conductance of Fe|MgO|Fe sandwiches. *Phys Rev B*. 2001;63:054416.
- [13] Mathon J, Umerski A. Theory of tunneling magnetoresistance of an epitaxial Fe/MgO/Fe(001) junction. *Phys Rev B*. 2001;63:220403(R).
- [14] Parkin SSP, Kaiser C, Panchkula A, et al. Giant tunnelling magnetoresistance at room temperature with MgO (100) tunnel barriers. *Nat Mater*. 2004;3:862.
- [15] Yuasa S, Nagahama T, Fukushima A, et al. Giant room-temperature magnetoresistance in single-crystal Fe/MgO/Fe magnetic tunnel junctions. *Nat Mater*. 2004;3:868.
- [16] Ikeda S, Hayakawa J, Ashizawa Y, et al. Tunnel magnetoresistance of 604% at 300K by suppression of Ta diffusion in CoFeB/MgO/CoFeB pseudo-spin-valves annealed at high temperature. *Appl Phys Lett*. 2008;93:082508.
- [17] Hirohata A, Frost W, Samiepour M, et al. Perpendicular Magnetic Anisotropy in Heusler Alloy Films and Their Magnetoresistive Junctions. *Mater*. 2018;11:105.
- [18] Yuasa S. Magnetoresistance and spin-transfer torque in magnetic tunnel junctions. [http://www.ewh.ieee.org/r6/scv/mag/MtgSum/Meeting2012\\_05\\_Presentation.pdf](http://www.ewh.ieee.org/r6/scv/mag/MtgSum/Meeting2012_05_Presentation.pdf).
- [19] Schmidt G, Ferrand D, Molenkamp LW, et al. Fundamental obstacle for electrical spin injection from a ferromagnetic metal into a diffusive semiconductor. *Phys Rev B*. 2000;62:4790(R).
- [20] Nagamine Y, Maehara H, Tsunekawa K, et al. Ultralow resistance-area product of 0.4 Ω(μm)<sup>2</sup> and high magnetoresistance above 50% in CoFeB/MgO/CoFeB magnetic tunnel junctions. *Appl Phys Lett*. 2006;89:162507.
- [21] Ikeda S, Miura K, Yamamoto H, et al. A perpendicular-anisotropy CoFeB–MgO magnetic tunnel junction. *Nat Mater*. 2010;9:721.
- [22] Yakushiji K, Kubota H, Fukushima A, et al. Perpendicular magnetic tunnel junctions with strong antiferromagnetic interlayer exchange coupling at first oscillation peak. *Appl Phys Exp*. 2015;8:083003.
- [23] <https://www.everspin.com/news/everspin-256mb-st-mram-perpendicular-mtj-sampling>.
- [24] Samsung Electronics Starts Commercial Shipment of eMRAM Product Based on 28nm FD-SOI Process. <https://news.samsung.com/global/samsung-electronics-starts-commercial-shipment-of-emram-product-based-on-28nm-fd-soi-process>.
- [25] Takagishi M, Yamada K, Iwasaki H, et al. Magnetoresistance Ratio and Resistance Area Design of CPP-MR Film for 2–5 Tb/in<sup>2</sup> Read Sensors. *IEEE Trans Magn*. 2010;46:2086.
- [26] Fuke HN, Hashimoto S, Takagishi M, et al. Magnetoresistance of FeCo Nanocontacts With Current-Perpendicular-to-Plane Spin-Valve Structure. *IEEE Trans Magn*. 2007;43:2848.
- [27] Galanakis I, Dederichs PH, Eds. CrO<sub>2</sub> predicted as a half-metallic ferromagnet. *Half-Metallic Alloys*. Berlin:Springer ; 2005.
- [28] Schwarz K. CrO<sub>2</sub> predicted as a half-metallic ferromagnet. *J Phys F*. 1986;16:L211.
- [29] Yamase A, Shiratori K. Anomalous Variation of Optical Spectra with Spin Polarization in Double-Exchange Ferromagnet: La<sub>1-x</sub>Sr<sub>x</sub>MnO<sub>3</sub>. *J Phys Soc Jpn*. 1984;53:312.
- [30] Okimoto Y, Katsufuji T, Ishikawa T, et al. Anomalous Variation of Optical Spectra with Spin Polarization in Double-Exchange Ferromagnet: La<sub>1-x</sub>Sr<sub>x</sub>MnO<sub>3</sub>. *Phys Rev Lett*. 1995;75:109.
- [31] Moodera JS, Meservey RH. Spin-polarized tunneling. In: Johnson M, editor. *Magneto-electronics*. Amsterdam, The Netherlands: Elsevier; 2004. p. pp. 163–204.
- [32] Ohno H. Ferromagnetic III–V semiconductors and their hetero-structures. In: Awschalom DD, Loss D, Samarth N, editors. *Semiconductor Spintronics and Quantum Computation*. Berlin, Germany: Springer; 2002. p. pp. 1–30.
- [33] Akinaga H, Manago T, Shirai M. Material Design of Half-Metallic Zinc-Blende CrAs and the Synthesis by Molecular-Beam Epitaxy. *Jpn J Appl Phys*. 2000;39:L1118.
- [34] de Groot RA, Mueller FM, van Engen PG, et al. New Class of Materials: Half-Metallic Ferromagnets. *Phys Rev Lett*. 1983;50:2024.
- [35] Dietl T, Ohno H, Matsukura F, et al. Zener Model Description of Ferromagnetism in Zinc-Blende Magnetic Semiconductors. *Sci*. 2000;287:1019.

- [36] Soulen RJ Jr., Byers JM, Osofsky MS, et al. Measuring the Spin Polarization of a Metal with a Superconducting Point Contact. *Sci.* **1998**;282:85.
- [37] Galanakis I. Theory of Heusler and full-Heusler compounds. In: Felser C, Hirohata A, editors. *Heusler Alloys*. Berlin, Germany: Springer; **2016**. p. pp. 3–36.
- [38] Hirohata A, Kikuchi M, Tezuka N, et al. Heusler alloy/semiconductor hybrid structures. *Curr Opin Solid State Mater Sci.* **2006**;10:93.
- [39] Hirohata A, Sukegawa H, Yanagihara H, et al. Roadmap for Emerging Materials for Spintronic Device Applications. *IEEE Trans Magn.* **2015**;51:0800511.
- [40] Jourdan M, Minár J, Braun J, et al. Direct observation of half-metallicity in the Heusler compound Co<sub>2</sub>MnSi. *Nat Commun.* **2014**;5:3974.
- [41] Hirohata A, Sagar J, Fleet LR, et al. Theory of Heusler and full-Heusler compounds. In: Felser C, Hirohata A, editors. *Heusler Alloys*. Berlin, Germany: Springer; **2016**. p. pp. 219–248.
- [42] Heusler F. Mangan-aluminium-kupferlegierungen. *Verh DPG.* **1903**;5:219.
- [43] Gutfleisch O, Gottschall T, Fries M, et al. Mastering hysteresis in magnetocaloric materials. *Phil Trans R Soc A.* **2016**;374:20150308.
- [44] Yu G-H, Xu Y-L, Liu Z-H, et al. Recent progress in Heusler-type magnetic shape memory alloys. *Rare Met.* **2015**;34:527.
- [45] Webster PJ, Ziebeck KRA. Heusler alloys. In: H. R. J. Wijn C, editor. *Landolt-Börnstein New Series Group III*, Vol. 19. Berlin: Springer; **1988**. p. 75.
- [46] Graf T, Felser C, Parkin SSP. Simple rules for the understanding of Heusler compounds. *Prog Solid State Chem.* **2011**;39:1.
- [47] Winterlik J, Fecher GH, Balke B, et al. Electronic, magnetic, and structural properties of the ferrimagnet Mn<sub>2</sub>CoSn. *Phys Rev B.* **2011**;83:174448.
- [48] Kreiner G, Kalache A, Hausdorf S, et al. New Mn<sub>2</sub>-based Heusler Compounds. *Allg Chem.* **2014**;640:738.
- [49] Dai X, Liu G, Fecher GH, Li Y, and Liu H. et al. New quaternary half metallic material CoFeMnSi. *J Appl Phys.* **2009**;105:07E901.
- [50] Ozdoğan K, Şaşıoğlu E, Galanakis I. Slater-Pauling behavior in LiMgPdSn-type multifunctional quaternary Heusler materials: Half-metallicity, spin-gapless and magnetic semiconductors. *J Appl Phys.* **2013**;113:193903.
- [51] Hirohata A, Sagar J, Lari L, et al. Heusler-alloy films for spintronic devices. *Appl Phys A.* **2013**;111:423.
- [52] Sagar J, Fleet LR, Walsh M, et al. *Appl Phys Lett.* **2014**;105:032401.
- [53] Fleet LR, Cheglakov G, Yoshida K, et al. Over 50% reduction in the formation energy of Co-based Heusler alloy films by two-dimensional crystallisation. *J Phys D Appl Phys.* **2012**;45:032001.
- [54] Frost W, Samiepour M, Hirohata A. Low-temperature crystallisation of Heusler alloy films with perpendicular magnetic anisotropy. *J Magn Magn Mater.* **2019**;484:100.
- [55] Ishikawa H, Umetsu RY, Kobayashi K, et al. Atomic ordering and magnetic properties in Ni<sub>2</sub>Mn(GaxAl<sub>1-x</sub>) Heusler alloys. *Acta Mater.* **2008**;56:4789.
- [56] Tang MB, Zhao JT. Low temperature transport and thermal properties of half-Heusler alloy Zr<sub>0.25</sub>Hf<sub>0.25</sub>Ti<sub>0.5</sub>NiSn. *J Alloys Comp.* **2009**;475:5.
- [57] Palmstrøm C. Epitaxial Heusler Alloys: New Materials for Semiconductor Spintronics. *MRS Bull.* **2003**;28:725.
- [58] Yoshimura K, Miyazaki A, Vijayaraghavan R, et al. Hyperfine field of the Co<sub>2</sub>YZ Heusler alloy (Y = V, Cr, Mn and Fe; Z = Al and Ga). *J Magn Magn Mater.* **1985**;53:189.
- [59] Page A, van der Ven A, Poudeu PFP, et al. Origins of phase separation in thermoelectric (Ti, Zr, Hf)NiSn half-Heusler alloys from first principles. *J Mater Chem A.* **2016**;4:13949.
- [60] Shaughnessy M, Damewood L, Fong CY, et al. Structural variants and the modified Slater-Pauling curve for transition-metal-based half-Heusler alloys. *J Appl Phys.* **2013**;113:043709.
- [61] Rai DP, Shankar SA, Sakhya AP, et al. Electronic and magnetic properties of X<sub>2</sub>YZ and XYZ Heusler compounds: a comparative study of density functional theory with different exchange-correlation potentials. *Mater Res Exp.* **2016**;3:075022.
- [62] Varaprasad BSDCS, Srinivasana A, Takahashi YK, et al. Spin polarization and Gilbert damping of Co<sub>2</sub>Fe(GaxGe<sub>1-x</sub>) Heusler alloys. *Acta Mater.* **2012**;60:6257.
- [63] Ma J, Hegde VI, Munira K, et al. Computational investigation of half-Heusler compounds for spintronics applications. *Phys Rev B.* **2017**;95:024411.
- [64] Şaşıoğlu E, Stabdratskii LM, Bruno P. Above-room-temperature ferromagnetism in half-metallic Heusler compounds NiCrP, NiCrSe, NiCrTe, and NiVAs: A first-principles study. *J Appl Phys.* **2005**;98:063523.
- [65] Kobayashi K, Umetsu RY, Kainuma R, et al. Phase separation and magnetic properties of half-metal-type Co<sub>2</sub>Cr<sub>1-x</sub>FexAl alloys. *Appl Phys Lett.* **2004**;85:4684.
- [66] Xu X, Okada H, Chieda Y, et al. Magnetoresistance and Thermal Transformation Arrest in Pd<sub>2</sub>Mn<sub>1.4</sub>Sn<sub>0.6</sub> Heusler Alloys. *Mater.* **2019**;12:2308.
- [67] Galanakis I, Dederichs PH, Papanikolaou N. Slater-Pauling behavior and origin of the half-metallicity of the full-Heusler alloys. *Phys Rev B.* **2002**;66:174429.
- [68] Alhuwaymel TF, Abdullah RM, Whear O, et al. New Bandgap Measurement Technique for a Half-Metallic Ferromagnet. *IEEE Trans Magn.* **2014**;50:2600504.
- [69] Galanakis I, Mavropoulos P, Dederichs PH. Electronic structure and Slater-Pauling behaviour in half-metallic Heusler alloys calculated from first principles. *J Phys D: Appl Phys.* **2006**;39:765.
- [70] Sanyal B, Eriksson O, Suresh KG, et al. Ferromagnetism in Mn doped half-Heusler NiTiSn: Theory and experiment. *Appl Phys Lett.* **2006**;89:212502.
- [71] Buschow KHJ, van Engen PG. Magnetic and magneto-optical properties of heusler alloys based on aluminium and gallium. *J Magn Magn Mater.* **1981**;25:90.
- [72] Block T, Felser C, Jakob G, et al. Large negative magnetoresistance effects in Co<sub>2</sub>Cr<sub>0.6</sub>Fe<sub>0.4</sub>Al. *J Solid State Chem.* **2003**;176:646.
- [73] Inomata K, Okamura S, Goto R, et al. Large Tunneling Magnetoresistance at Room Temperature Using a Heusler Alloy with the B<sub>2</sub> Structure. *Jpn J Appl Phys.* **2003**;42:L419.
- [74] Skaftouros S, Özdoğan K, Şaşıoğlu E, et al. Generalized Slater-Pauling rule for the inverse Heusler compounds. *Phys Rev B.* **2013**;87:024420.
- [75] Mavropoulos P, Galanakis I, Popescu V, et al. The influence of spinorbit coupling on the band gap of Heusler alloys. *J Phys Condens Matter.* **2004**;16:S5759.
- [76] Hanssen KEHM, Mijnenrends PE. Positron-annihilation study of the half-metallic ferromagnet NiMnSb: Theory. *Phys Rev B.* **1986**;34:5009.

- [77] Hanssen KEHM, Mijnders PE, Rabou LPLM, et al. Positron-annihilation study of the half-metallic ferromagnet NiMnSb: Experiment. *Phys Rev B*. 1990;42:1533.
- [78] Mancoff FB, Bobo JF, Richter OE, et al. Growth and Characterization of Epitaxial NiMnSb/PtMnSb C1b Heusler alloy superlattices. *J Mater Res*. 1999;14:1560.
- [79] Tanaka CT, Nowak J, Moodera JS. Spin-polarized tunneling in a half-metallic ferromagnet. *J Appl Phys*. 1999;86:6239.
- [80] Orgassa D, Fujiwara H, Schulthess TC, et al. First-principles calculation of the effect of atomic disorder on the electronic structure of the half-metallic ferromagnet NiMnSb. *Phys Rev B*. 1999;60:13237.
- [81] Jenkins SJ, King DA. Minority metallic surface states of a half-metallic ferrimagnet. *Surf Sci*. 2001;494: L793.
- [82] Jenkins SJ. Ternary half-metallics and related binary compounds: Stoichiometry, surface states, and spin. *Phys Rev B*. 2004;70:245401.
- [83] Ristoiu D, Nozières JP, Borca CN, et al. The surface composition and spin polarization of NiMnSb epitaxial thin films. *Europhys Lett*. 2000;49:624.
- [84] Turban P, Andrieu S, Kierren B, et al. Growth and characterization of single crystalline NiMnSb thin films and epitaxial NiMnSb/MgO/NiMnSb(001) trilayers. *Phys Rev B*. 2002;65:134417.
- [85] van Roy W, de Boeck J, Brijs B, et al. Epitaxial NiMnSb films on GaAs(001). *Appl Phys Lett*. 2000;77:4190.
- [86] van Roy W, Wójcik M, Jędryka E, et al. Very low chemical disorder in epitaxial NiMnSb films on GaAs(111)B. *Appl Phys Lett*. 2003;83:4214.
- [87] Wu Y, Wu B, Wei Z, et al. Structural, half-metallic and elastic properties of the half-Heusler compounds NiMnM ( $M = \text{Sb, As and Si}$ ) and IrMnAs from first-principles calculations. *Intermetallics*. 2014;53:26.
- [88] van Engen PG, Buschow KHJ, Jongebreur R. PtMnSb, a material with very high magneto-optical Kerr effect. *Appl Phys Lett*. 1983;42:202.
- [89] Clows SK, Miyoshi Y, Bugoslavsky Y, et al. Spin polarization of the transport current at the free surface of bulk NiMnSb. *Phys Rev B*. 2004;69:214425.
- [90] Hordequin C, Pierre J, Currat R. Magnetic excitations in the half-metallic NiMnSb ferromagnet: From Heisenberg-type to itinerant behaviour. *J Magn Magn Mater*. 1996;162:75.
- [91] de Wijs GA, de Groot RA. Towards 100% spin-polarized charge-injection: The half-metallic NiMnSb/CdS interface. *Phys Rev B*. 2001;64:020402(R).
- [92] Galanakis I. Surface properties of the half-and full-Heusler alloys. *J Phys Condens Matter*. 2002;14:6329.
- [93] Block T, Carey MJ, Gurney BA, et al. Band-structure calculations of the half-metallic ferromagnetism and structural stability of full- and half-Heusler phases. *Phys Rev B*. 2004;70:205114.
- [94] Ležaić M, Galanakis I, Bihlmayer G, et al. Structural and magnetic properties of the (001) and (111) surfaces of the half-metal NiMnSb. *J Phys Condens Matter*. 2005;17:3121.
- [95] Galanakis I, Ležaić M, Bihlmayer G, et al. Interface properties of NiMnSb/InP and NiMnSb/GaAs contacts. *Phys Rev B*. 2005;71:214431.
- [96] Johnson PR, Kautzky MC, Mancoff FB, et al. Observation of giant magnetoresistance in a Heusler alloy spin valve. *IEEE Trans Magn*. 1996;32:4615.
- [97] Galanakis I. Orbital magnetism in the half-metallic Heusler alloys. *Phys Rev B*. 2005;71:012413.
- [98] Tsirogiannis C, Galanakis I. Effect of the double-counting functional on the electronic and magnetic properties of half-metallic magnets using the GGA+U method. *J Magn Magn Mater*. 2015;393:297.
- [99] Kautzky MC, Mancoff FB, Bobo J-F, et al. Time dependence of laser-induced thermoelectric voltages in  $\text{La}_{1-x}\text{Ca}_x\text{MnO}_3$   $\text{La}_{1-x}\text{Ca}_x\text{MnO}_3$  and  $\text{YBa}_2\text{Cu}_3\text{O}_{7-\delta}$  thin films. *J Appl Phys*. 1997;81:4026.
- [100] Şaşıoğlu E, Sandratskii LM, Bruno P, et al. Exchange interactions and temperature dependence of magnetization in half-metallic Heusler alloys. *Phys Rev B*. 2005;72:184415.
- [101] Toboła J, Pierre J, Kaprzyk S, et al. Crossover from semiconductor to magnetic metal in semi-Heusler phases as a function of valence electron concentration. *J Phys Condens Matter*. 1998;10:1013.
- [102] Ouardi S, Fecher GH, Felser C. Electronic structure and optical, mechanical, and transport properties of the pure, electron-doped, and hole-doped Heusler compound CoTiSb. *Phys Rev B*. 2012;86:045116.
- [103] Wen Z, Kubota T, Takanashi K. Optimization of half-Heusler PtMnSb alloy films for spintronic device applications. *J Phys D: Appl Phys*. 2018;51:435002.
- [104] Ambrose T, Krebs JJ, Prinz GA. Epitaxial growth and magnetic properties of single-crystal  $\text{Co}_2\text{MnGe}$  Heusler alloy films on GaAs(001). *Appl Phys Lett*. 2000;76:3280.
- [105] Picozzi S, Continenza A, Freeman AJ. First principles study of electronic and magnetic properties of  $\text{Co}_2\text{MnGe}/\text{GaAs}$  interfaces. *J Phys Chem Solids*. 2003;64:1697.
- [106] Fujii S, Sugimura S, Ishida S, et al. Hyperfine fields and electronic structures of the Heusler alloys  $\text{Co}_2\text{MnX}$  ( $X = \text{Al, Ga, Si, Ge, Sn}$ ). *J Phys Condens Matter*. 1990;2:8583.
- [107] Galanakis I. Appearance of half-metallicity in the quaternary Heusler alloys. *J Phys Condens Matter*. 2004;16:3089.
- [108] Ishida S, Fujii D, Kashiwagi S, et al. Search for Half-Metallic Compounds in  $\text{Co}_2\text{MnZ}$  ( $Z = \text{IIIb, IVb, Vb Element}$ ). *J Phys Soc Jpn*. 1995;64:2152.
- [109] Kubota H, Nakata J, Oogane M, et al. Large Magnetoresistance in Magnetic Tunnel Junctions Using Co-Mn-Al Full Heusler Alloy. *Jpn J Appl Phys*. 2004;43:L984.
- [110] Sakuraba Y, Nakata J, Oogane M, et al. Magnetic tunnel junctions using B2-ordered  $\text{Co}_2\text{MnAl}$  Heusler alloy epitaxial electrode. *Appl Phys Lett*. 2006;88:022503.
- [111] Sakuraba Y, Nakata J, Oogane M, et al. Fabrication of  $\text{Co}_2\text{MnAl}$  Heusler Alloy Epitaxial Film Using Cr Buffer Layer. *Jpn J Appl Phys*. 2005;44:6535.
- [112] Yilgin R, Oogane M, Yakata S, et al. Intrinsic Gilbert damping constant in  $\text{Co}_2\text{MnAl}$  Heusler alloy films. *IEEE Trans Magn*. 2005;41:2799.
- [113] Geiersbach U, Bergmann A, Westerholt K. Structural, magnetic and magnetotransport properties of thin films of the Heusler alloys  $\text{Cu}_2\text{MnAl}$ ,  $\text{Co}_2\text{MnSi}$ ,  $\text{Co}_2\text{MnGe}$  and  $\text{Co}_2\text{MnSn}$ . *J Magn Magn Mater*. 2002;240:546.
- [114] Brown PJ, Neumann KU, Webster PJ, et al. The magnetization distributions in some Heusler alloys proposed as half-metallic ferromagnets. *J Phys Condens Matter*. 2000;12:1827.
- [115] Raphael MP, Ravel B, Huang Q, et al. Presence of antisite disorder and its characterization in the

- predicted half-metal  $\text{Co}_2\text{MnSi}$ . Phys Rev B. [2002](#);66:104429.
- [116] Singh LJ, Barber ZH, Miyoshi Y, et al. Structural and transport studies of stoichiometric and off-stoichiometric thin films of the full Heusler alloy  $\text{Co}_2\text{MnSi}$ . J Appl Phys. [2004](#);95:7231.
- [117] Kämmerer S, Thomas A, Hütten A, et al.  $\text{Co}_2\text{MnSi}$  Heusler alloy as magnetic electrodes in magnetic tunnel junctions. Appl Phys Lett. [2004](#);85:79.
- [118] Wang WH, Przybylski M, Kuch W, et al. Magnetic properties and spin polarization of  $\text{Co}_2\text{MnSi}$  Heusler alloy thin films epitaxially grown on  $\text{GaAs}(001)$ . Phys Rev B. [2005](#);71:144416.
- [119] Singh LJ, Barber ZH, Kohn A, et al. Interface effects in highly oriented films of the Heusler alloy  $\text{Co}_2\text{MnSi}$  on  $\text{GaAs}(001)$ . J Appl Phys.. [2006](#);99:013904.
- [120] Picozzi S, Continenza A, Freeman AJ.  $\text{Co}_2\text{MnX}$  ( $X=\text{Si, Ge, Sn}$ ) Heusler compounds: An *ab initio* study of their structural, electronic, and magnetic properties at zero and elevated pressure. Phys Rev B.. [2006](#);99:013904.
- [121] Sakuraba Y, Nakata J, Oogane M, et al. Huge Spin-Polarization of L21-Ordered  $\text{Co}_2\text{MnSi}$  Epitaxial Heusler Alloy Film. Jpn J Appl Phys. [2005](#);44:L1100.
- [122] Hickey MC, Damsgaard CD, Farrer I, et al. Spin injection between epitaxial  $\text{Co}_2\text{Mn}_1.6\text{Ga}$  and an  $\text{InGaAs}$  quantum well. Appl Phys Lett. [2005](#);86:252106.
- [123] Holmes SN, Pepper M. Magnetic and electrical properties of  $\text{Co}_2\text{MnGa}$  grown on  $\text{GaAs}(001)$ . Appl Phys Lett. [2002](#);81:1651.
- [124] Miyamoto K, Kimura A, Iori K, et al. Current-perpendicular-to-the-plane giant magnetoresistance in structures with half-metal materials laminated between  $\text{CoFe}$  layers. J Phys Condens Matter. [2004](#);16:S5797.
- [125] Hoshiya H, Hoshino K. Current-perpendicular-to-the-plane giant magnetoresistance in structures with half-metal materials laminated between  $\text{CoFe}$  layers. J Appl Phys. [2004](#);95:6774.
- [126] Fecher GH, Kandpal HC, Wurmehl S, et al. Design of magnetic materials: the electronic structure of the ordered, doped Heusler compound  $\text{Co}_2\text{Cr}_1-x\text{Fe}_x\text{Al}$ . J Phys Condens Matter. [2005](#);17:7237.
- [127] Antonov VN, Dürr HA, Kucherenko Y, et al. Theoretical study of the electronic and magnetic structures of the Heusler alloys  $\text{Co}_2\text{Cr}_{1-x}\text{Fe}_x\text{Al}$ . Phys Rev B. [2005](#);72:054441.
- [128] Kelekar R, Clemens BM. Epitaxial growth of the Heusler alloy  $\text{Co}_2\text{Cr}_1-x\text{Fe}_x\text{Al}$ . J Appl Phys. [2004](#);96:540.
- [129] Hirohata A, Kurebayashi H, Okamura S, et al. Structural and magnetic properties of epitaxial L 2 1 L 2 1 -structured  $\text{Co}_2(\text{Cr,Fe})\text{Al}$  films grown on  $\text{GaAs}(001)$  substrates. J Appl Phys. [2005](#);97:103714.
- [130] Okamura S, Goto R, Sugimoto S, et al. Structural, magnetic, and transport properties of full-Heusler alloy  $\text{Co}_2(\text{Cr}_1-x\text{Fe}_x)\text{Al}$  thin films. J Appl Phys.. J Appl Phys. [2004](#);96:6561.
- [131] Nagao K, Shirai M, Miura Y. *Ab initio* calculations of spin polarization at  $\text{Co}_2\text{CrAl}/\text{GaAs}$  interfaces. J Phys Condens Matter. [2004](#);16:S5725.
- [132] Galanakis I. Towards half-metallic interfaces:  $\text{Co}_2\text{CrAl}/\text{InP}$  contacts. J Phys Condens Matter. [2004](#);16:8007.
- [133] Zhang M, Liu Z, Hu H, et al. Is Heusler compound  $\text{Co}_2\text{CrAl}$  a half-metallic ferromagnet: electronic band structure, and transport properties. J Magn Magn Mater. [2004](#);277:130.
- [134] Hirohata A, Kurebayashi H, Okamura S, et al. Magnetic properties of L 2 1 L 2 1 -structured  $\text{Co}_2(\text{Cr,Fe})\text{Al}$  films grown on  $\text{GaAs}(001)$  substrates. J Appl Phys. [2005](#);97:10C308.
- [135] Block T, Felser C, Jakob G, et al. Large negative magnetoresistance effects in  $\text{Co}_2\text{Cr}_0.6\text{Fe}_0.4\text{Al}$ . J Solid State Chem.. [2003](#);176:646.
- [136] Clifford E, Venkatesan M, Gunning R, et al. Magnetoresistance in point contacts of the Heusler alloy  $\text{Co}_2\text{Cr}_0.6\text{Fe}_0.4\text{Al}$ . Solid State Commun. [2004](#);131:61.
- [137] Elmers HJ, Fecher GH, Valdaitev D, et al. Element-specific magnetic moments from core-absorption magnetic circular dichroism of the doped Heusler alloy  $\text{Co}_2\text{Cr}_0.6\text{Fe}_0.4\text{Al}$ . Phys Rev B.. [2003](#);69:144413.
- [138] Elmers HJ, Wurmehl S, Fecher GH, et al. Hole injection barriers at polymer anode/small molecule interfaces. Appl Phys. [2004](#);79:557.
- [139] Marukame T, Kasahara T, Matsuda K-I, et al. High tunnel magnetoresistance in epitaxial  $\text{Co}_2\text{Cr}_0.6\text{Fe}_0.4\text{Al}/\text{MgO}/\text{CoFe}$  tunnel junctions. IEEE. [2006](#);99:013904.
- [140] Miura Y, Shirai M, Nagao K. Element-specific magnetic moments from core-absorption magnetic circular dichroism of the doped Heusler alloy  $\text{Co}_2\text{Cr}_0.6\text{Fe}_0.4\text{Al}$  J Appl Phys.. [2004](#);69:144413.
- [141] Kandpal HC, Fecher GH, Felser C, et al. Correlation in the transition-metal-based Heusler compounds  $\text{Co}_2\text{MnSi}$  and  $\text{Co}_2\text{FeSi}$ . Phys Rev B. [2006](#);73:094422.
- [142] Chen X-Q, Podloucky R, Rogl P. *Ab initio* prediction of half-metallic properties of the ferromagnetic Heusler alloys  $\text{Co}_2\text{MSi}$  ( $M=\text{Ti, V, Cr}$ ). J Appl Phys.. [2006](#);100:113901.
- [143] Wurmehl S, Fecher GH, Kandpal HC, et al. Geometric, electronic, and magnetic structure of  $\text{Co}_2\text{FeSi}$ : Curie temperature and magnetic moment measurements and calculations. Phys Rev B. [2005](#);72:184434.
- [144] Gloskovski A, Barth J, Balke B, et al. A spatially resolved investigation of the local, micro-magnetic domain structure of single and polycrystalline  $\text{Co}_2\text{FeSi}$ . J Phys D: Appl Phys. [2007](#);40:1570.
- [145] Balke B, Fecher GH, Felser C. Structural and magnetic properties of  $\text{Co}_2\text{FeAl}_{1-x}\text{Six}$ . Appl Phys Lett. [2007](#);90:242503.
- [146] Nakatani TM, Rajanikanth A, Gercsi Z, et al. Structure, magnetic property, and spin polarization of  $\text{Co}_2\text{FeAl}_x\text{Si}_{1-x}$  Heusler alloys. J Appl Phys. [2007](#);102:033916.
- [147] Ebke D, Schmalhorst J, Liu -N-N, et al. Large tunnel magnetoresistance in tunnel junctions with  $\text{Co}_2\text{MnSi}/\text{Co}_2\text{FeSi}$  multilayer electrode. Appl Phys Lett. [2006](#);89:162506.
- [148] Schneider H, Jakob G, Kallmayer M, et al. Epitaxial film growth and magnetic properties of  $\text{Co}_2\text{FeSi}$ . Phys Rev B. [2006](#);74:174426.
- [149] Hashimoto M, Herfort J, Schönherr H-P, et al. Epitaxial Heusler alloy  $\text{Co}_2\text{FeSi}/\text{GaAs}(001)$ ... hybrid structures. Appl Phys Lett. [2005](#);87:102506.
- [150] Wurmehl S, Kohlhepp JT, Swagten HJM, et al. Probing the random distribution of half-metallic  $\text{Co}_2\text{Mn}_{1-x}\text{Fe}_x\text{Si}$  Heusler alloys. Appl Phys Lett. [2007](#);91:052506.
- [151] Oogane M, Yilgin R, Shinano M, et al. Magnetic damping constant of  $\text{Co}_2\text{FeSi}$  Heusler alloy thin film. J Appl Phys. [2007](#);101:09J501.
- [152] Hashimoto M, Herfort J, Trampert A, et al. Growth, interface structure and magnetic properties of



- Heusler alloy Co<sub>2</sub>FeSi/GaAs(0 0 1) hybrid structures. *J Cryst Growth*. 2007;301-302:592.
- [153] Yilgin R, Sakuraba Y, Oogane M, et al. Anisotropic Intrinsic Damping Constant of Epitaxial Co<sub>2</sub>MnSi Heusler Alloy Films. *Jpn J Appl Phys*. 2007;46:L205.
- [154] Lee SC, Lee TD, Blaha P, et al. Magnetic and half-metallic properties of the full-Heusler alloys Co<sub>2</sub>TiX (X=Al,Ga,Si,Ge,Sn,Sb). *J Appl Phys*. 2005;97:10C307.
- [155] Zhang W, Qian Z, Sui Y, et al. Transport properties and structural phase transition of the Heusler alloy Co<sub>2</sub>TiAl synthesized by the melt-spinning technique. *Physica B*. 2005;367:205.
- [156] Yamasaki A, Imada S, Arai R, et al. Orbital angular momentum and interpretation of core-absorption magnetic circular dichroism on the band picture in Co-based Heusler alloys Co<sub>2</sub>YSn (Y=Ti, Zr, and Nb). *Phys Rev B*. 2002;65:104410.
- [157] Majumdar S, Chattopadhyay MK, Sharma VK, et al. Transport properties of the ferromagnetic Heusler alloy Co<sub>2</sub>TiSn. *Phys Rev B*. 2005;72:012417.
- [158] Dong XY, Dong JW, Xie JQ, et al. Growth temperature controlled magnetism in molecular beam epitaxially grown Ni<sub>2</sub>MnAl Heusler alloy. *J Cryst Growth*. 2003;254:384.
- [159] Dong JW, Chen LC, Palmstrøm, et al. Molecular beam epitaxy growth of ferromagnetic single crystal (001) Ni<sub>2</sub>MnGa on (001) GaAs. *Appl Phys*. 2006;99:013904.
- [160] Dong JW, Chen LC, Xie JQ, et al. Epitaxial growth of ferromagnetic Ni<sub>2</sub>MnGa on GaAs(001) using NiGa interlayers. *J Appl Phys*. 2000;88:7357.
- [161] Dong JW, Lu J, Xie JQ, et al. MBE growth of ferromagnetic single crystal Heusler alloys on (0 0 1)Ga<sub>1-x</sub>In<sub>x</sub>As. *Physica E*. 2001;10:428.
- [162] Godlevsky VV, Rabe KM. Soft tetragonal distortions in ferromagnetic Ni<sub>2</sub>MnGa and related materials from first principles. *Phys Rev B*. 2001;63:134407.
- [163] Lu J, Dong JW, Xie JQ, et al. Molecular-beam-epitaxy growth of ferromagnetic Ni<sub>2</sub>MnGe on GaAs(001). *Appl Phys Lett*. 2003;83:2393.
- [164] Xie JQ, Dong JW, Lu J, et al. Epitaxial growth of ferromagnetic Ni<sub>2</sub>MnIn on (001) InAs. *Appl Phys Lett*. 2001;79:1003.
- [165] Blocklage L, Scholtyssek JM, Merkt U, et al. Spin polarization of Ni<sub>2</sub>MnIn and Ni<sub>80</sub>Fe<sub>20</sub> determined by point-contact Andreev spectroscopy. *J Appl Phys*. 2007;101:09J512.
- [166] Kilian KA, Victora RH. Electronic structure of Ni<sub>2</sub>MnIn for use in spin injection. *J Appl Phys*. 2000;87:7064.
- [167] Galanakis I, Özdoğan K, Şaşıoğlu E, et al. *Ab initio* design of half-metallic fully compensated ferrimagnets: The case of Cr<sub>2</sub>MnZ (Z=P, As, Sb, and Bi). *Phys Rev B*. 2007;75:172405.
- [168] Webster PJ. Magnetic and chemical order in Heusler alloys containing cobalt and manganese. *J Phys Chem Solids*. 1971;32:1221.
- [169] Cullity BD. *Elements of X-Ray Diffraction*. 2nd ed. Addison Wesley, Reading; 1977.
- [170] Takamura Y, Nakane R, Sugahara S. Quantitative analysis of atomic disorders in full-Heusler Co<sub>2</sub>FeSi Co<sub>2</sub>FeSi alloy thin films using x-ray diffraction with CoK $\alpha$  and CuK $\alpha$  sources. *J Appl Phys*. 2010;107:09B111.
- [171] Niculescu V, Raj K, Burch TJ, et al. Correlation of the internal fields, magnetic moments, and site preferences in Fe<sub>3-x</sub>Mn<sub>x</sub>Si alloys. *Phys Rev B*. 1967;13:3167.
- [172] Gabor MS, Belmuguenai M, Petrisor T Jr., et al. Correlations between structural, electronic transport, and magnetic properties of Co<sub>2</sub>FeAl<sub>0.5</sub>Si<sub>0.5</sub> Heusler alloy epitaxial thin films. *Phys Rev B*. 2015;92:054433.
- [173] Yamada S, Yamamoto K, Ueda K, et al. Epitaxial growth of a full-Heusler alloy Co<sub>2</sub>FeSi on silicon by low-temperature molecular beam epitaxy. *Thin Solid Films*. 2010;518:S278.
- [174] Hong S, Pirri C, Wetzel P, et al. Synthesis of epitaxial ternary Co<sub>1-x</sub>Fe<sub>x</sub>Si<sub>2</sub> silicides with CsCl- and CaF<sub>2</sub>-type cubic structures on Si(111) by codeposition techniques. *Phys Rev B*. 1997;55:13040.
- [175] Furukawa N. Unconventional One-Magnon Scattering Resistivity in Half-Metals. *J Phys Soc Jpn*. 2000;69:1954.
- [176] Zhang M, Bruck E, de Boer FR, et al. The magnetic and transport properties of the Co<sub>2</sub>FeGa Heusler alloy. *J Phys D Appl Phys*. 2004;37:2049.
- [177] Srinivas K, Manivel Raja M, Kamat SV. Effect of partial substitution of silicon by other sp-valent elements on structure, magnetic properties and electrical resistivity of Co<sub>2</sub>FeSi Heusler alloys. *J Alloys Comp*. 2015;619:177.
- [178] Lovesey SW, Collins SP. X-ray circular dichroism as a probe of orbital magnetization. *X-Ray Absorption by Magnetic Materials* (Oxford University Press. Oxford; 1996.
- [179] Thole BT, Carra P, Sette F, et al. X-ray circular dichroism as a probe of orbital magnetization. *Phys Rev Lett*. 1992;68:1943.
- [180] Carra P, Thole BT, Altarelli M, et al. X-ray circular dichroism and local magnetic fields. *Phys Rev Lett*. 1993;70:694.
- [181] Chen CT, Idzerda YU, Lin H-J, et al. Experimental Confirmation of the X-Ray Magnetic Circular Dichroism Sum Rules for Iron and Cobalt. *Phys Rev Lett*. 1995;75:152.
- [182] Rai DP, Sandeep MP. Ghimire and R. K. Thapa. Ground state study of Electronic and Magnetic Properties of Co<sub>2</sub>MnZ (Z = Ge, Sn) type Heusler Compounds: A first Principle Study. *J Phys Conf Ser*. 2012;377:012074.
- [183] Miyamoto K, Kimura A, Iori K, et al. Orbital magnetic moment of “half-metallic” Co<sub>2</sub>MnGe. *Physica B*. 2004;351:347.
- [184] Hahn M, Schönhense G, Arbelo Jorge E, et al. Significant spin polarization of Co<sub>2</sub>MnGa Heusler thin films on MgO(100) measured by ultraviolet photoemission spectroscopy. *Appl Phys Lett*. 2011;98:232503.
- [185] Oksenenko VA, Kulagin VA, Kudryavtsev YV, et al. Magnetic properties of Co<sub>2</sub>MnGa Heusler alloy films with different crystalline order. *J Magn Magn Mater*. 2007;316:e407.
- [186] Claydon JS, Hassan S, Damsgaard CD, et al. Element specific investigation of ultrathin Co<sub>2</sub>MnGa/GaAs heterostructures. *J Appl Phys*. 2007;101:09J506.
- [187] Schmalhorst J, Sacher MD, Höink V, et al. Magnetic and chemical properties of Co<sub>2</sub>MnSi Co<sub>2</sub>MnSi thin films compared to the Co<sub>2</sub>MnSi/Al-O interface. *J Appl Phys*. 2006;100:113903.
- [188] Kallmayer M, Conca A, Jourdan M, et al. Correlation of local disorder and electronic properties in the Heusler alloy Co<sub>2</sub>Cr<sub>0.6</sub>Fe<sub>0.4</sub>Al. *J Phys D Appl Phys*. 2007;40:1539.
- [189] Lantri T, Bentata S, Bouadjemi B, et al. Effect of Coulomb interactions and Hartree-Fock exchange on structural, elastic, optoelectronic and magnetic

- properties of Co<sub>2</sub>MnSi Heusler: A comparative study. *J Magn Magn Mater.* **2016**;419:74.
- [190] Wurmehl S, Fecher GH, Kroth K, et al. Electronic structure and spectroscopy of the quaternary Heusler alloy Co<sub>2</sub>Cr<sub>1-x</sub>Fe<sub>x</sub>Al. *J Phys D Appl Phys.* **2006**;39:803.
- [191] Wilde L, Schumann J, Thomas J, et al. Microstructure of Co<sub>2</sub>CrxFe<sub>1-x</sub>Al thin films for magneto-electronic applications. *Thin Solid Films.* **2007**;515:6781.
- [192] Okabayashi J, Sukegawa H, Wen Z, et al. Large anisotropic Fe orbital moments in perpendicularly magnetized Co<sub>2</sub>FeAl Heusler alloy thin films revealed by angular-dependent x-ray magnetic circular dichroism. *Appl Phys Lett.* **2013**;103:102402.
- [193] Soni S, Dalela S, Sharma SS, et al. Study of electronic structure and magnetic properties of epitaxial Co<sub>2</sub>FeAl Heusler Alloy Thin Films. *J Alloys Comp.* **2016**;674:295.
- [194] Kallmayer M, Schneider H, Jakob G, et al. Interface magnetization of ultrathin epitaxial Co<sub>2</sub>FeSi(110)/Al<sub>2</sub>O<sub>3</sub> films. *J Phys D Appl Phys.* **2007**;40:1552.
- [195] Ramude M, Manivel Raja M, Basumartary H, et al. Investigations on structural, magnetic and calorimetric properties of Co<sub>2</sub>FeSi<sub>1-x</sub>B<sub>x</sub> (x = 0–0.5) Heusler alloys: Role of boron. *J Magn Magn Mater.* **2019**;490:165528.
- [196] Tedrow PM, Meservey R. Spin-polarized electron tunneling. *Phys Rep.* **1994**;238:173.
- [197] Shigeta I, Murayama O, Hisamatsu T, et al. Measurements of spin polarization of Ru<sub>2-x</sub>Fe<sub>x</sub>CrSi Heusler alloys by Andreev reflection. *Phys C.* **2010**;470: S806.
- [198] Matsuda K, Hiroi M, Kawakami M. Magnetic properties of Heusler alloys Ru<sub>2-x</sub>Fe<sub>x</sub>CrSi. *J Phys Condens Matter.* **2005**;17:5889.
- [199] Matsuda K, Hiroi M, Kawakami M. Magnetic properties of Heusler alloys Ru<sub>2-x</sub>Fe<sub>x</sub>CrSi. *J Phys Condens Matter.* **2005**;17:5889.
- [200] Shigeta I, Kubota T, Sakuraba Y, et al. Temperature and field induced spin reorientation and dielectric properties in YCr<sub>0.88</sub>Fe<sub>0.12</sub>O<sub>3</sub> single crystal. *Appl Phys Lett.* **2018**;111:072402.
- [201] Alhuwaymel TF, Carpenter R, Yu CNT, et al. Direct band-gap measurement on epitaxial Co<sub>2</sub>FeAl<sub>0.5</sub>Si<sub>0.5</sub> Heusler-alloy films. *J Appl Phys.* **2015**;117:17D131.
- [202] Schmitt J, Gibbs Z, Schnyder G, et al. Resolving the true band gap of ZrNiSn half-Heusler thermoelectric materials. *Mater Horiz.* **2014**;2:68.
- [203] Aliev FG, Kozyrkov VV, Moshchalkov VV, et al. Narrow band in the intermetallic compounds MNiSn (M=Ti, Zr, Hf). *Z Phys B: Condens Matter.* **1990**;80:353.
- [204] Slonczewski JC. Current-driven excitation of magnetic multilayers. *J Magn Magn Mater.* **1996**;159:L1.
- [205] Kambersky V. On the Landau–Lifshitz relaxation in ferromagnetic metals. *Can J Phys.* **1970**;48:2906.
- [206] Oogane M, Wakitani T, Yakata S, et al. Magnetic Damping in Ferromagnetic Thin Films. *Jpn J Appl Phys.* **2006**;45:3889.
- [207] van Kampen M, Jozsa C, Kohlhepp JT, et al. All-Optical Probe of Coherent Spin Waves. *Phys Rev Lett.* **2002**;88:227201.
- [208] Mizukami S, Watanabe D, Oogane M, et al. Low damping constant for Co<sub>2</sub>FeAl Heusler alloy films and its correlation with density of states. *J Appl Phys.* **2009**;105:07D306.
- [209] Lee H, Wang Y-HA, Mewes CKA, et al. Magnetization relaxation and structure of CoFeGe alloys. *Appl Phys Lett.* **2009**;95:082502.
- [210] Oogane M, Kubota T, Kota Y, et al. Gilbert magnetic damping constant of epitaxially grown Co-based Heusler alloy thin films. *Appl Phys Lett.* **2010**;96:252501.
- [211] Andrieu S, Neggache A, Hauet T, et al. Direct evidence for minority spin gap in the Co<sub>2</sub>MnSi Heusler compound. *Phys Rev B.* **2016**;93:094417.
- [212] Bainsla L, Yilgin R, Tsujikawa M, et al. Low magnetic damping for equiatomic CoFeMnSi Heusler alloy. *J Phys D: Appl Phys.* **2018**;51:495001.
- [213] Oogane M, MacFadden AP, Fukuda K, et al. Low magnetic damping and large negative anisotropic magnetoresistance in half-metallic Co<sub>2-x</sub>Mn<sub>1+x</sub>Si Heusler alloy films grown by molecular beam epitaxy. *Appl Phys Lett.* **2018**;112:262407.
- [214] Sebastian T, Ohdaira Y, Kubota T, et al. Low-damping spin-wave propagation in a micro-structured Co<sub>2</sub>Mn<sub>0.6</sub>Fe<sub>0.4</sub>Si Heusler waveguide. *Appl Phys Lett.* **2012**;100:112402.
- [215] Sebastian T, Bracher T, Pirro P, et al. Nonlinear Emission of Spin-Wave Caustics from an Edge Mode of a Microstructured Co<sub>2</sub>Mn<sub>0.6</sub>Fe<sub>0.4</sub>Si Waveguide. *Phys Rev Lett.* **2013**;110:067201.
- [216] Kubota T, Tsunegi S, Oogane M, et al. Half-metallicity and Gilbert damping constant in Co<sub>2</sub>Fe<sub>x</sub>Mn<sub>1-x</sub>Si Heusler alloys depending on the film composition. *Appl Phys Lett.* **2009**;94:122504.
- [217] Mizukami S, Tsunegi S, Kubota T, et al. Ultrafast demagnetization for Ni<sub>80</sub>Fe<sub>20</sub> and half-metallic Co<sub>2</sub>MnSi heusler alloy films. *J Phys Conf Ser.* **2010**;200:042017.
- [218] Oogane M, Kubota T, Naganuma H, et al. Magnetic damping constant in Co-based full heusler alloy epitaxial films. *J Phys D Appl Phys.* **2015**;48:164012.
- [219] Sterrwerf C, Paul S, Khodadadi B, et al. Low Gilbert damping in Co<sub>2</sub>FeSi and Fe<sub>2</sub>CoSi films. *J Appl Phys.* **2016**;120:083904.
- [220] Yadav A, Chaudhary S. Structural and dynamical magnetic response of co-sputtered Co<sub>2</sub>FeAl heusler alloy thin films grown at different substrate temperatures. *J Appl Phys.* **2014**;115:133916.
- [221] Cui Y, Lu J, Schafer S, et al. Magnetic damping and spin polarization of highly ordered B2 Co<sub>2</sub>FeAl thin films. *J Appl Phys.* **2014**;116:073902.
- [222] Takahashi YK, Miura Y, Choi R, et al. Increased magnetic damping in ultrathin films of Co<sub>2</sub>FeAl with perpendicular anisotropy. *Appl Phys Lett.* **2017**;110:252409.
- [223] Dubowik J, Goscianska I, Zleski K, et al. Epitaxial Growths and Magnetization Dynamics of Ni<sub>2</sub>MnSn Heusler Alloy Films. *Acta Phys Pol A.* **2012**;121:1121.
- [224] Gladden LF. Nuclear magnetic resonance in chemical engineering: principles and applications. *Chem Eng Sci.* **1994**;49:3339.
- [225] Veeman WS. Nuclear magnetic resonance, a simple introduction to the principles and applications. *Geoderma.* **1997**;80:225.
- [226] Wurmehl S, Kohlhepp JT, Swagten HJM, et al. Probing the random distribution of half-metallic Co<sub>2</sub>Mn<sub>1-x</sub>Fe<sub>x</sub>Si Heusler alloys. *Appl Phys Lett.* **2007**;91:052506.
- [227] Wurmehl S, Kohlhepp J. Nuclear magnetic resonance studies of materials for spintronic applications. *J Phys D Appl Phys.* **2008**;41:173002.

- [228] Wurmehl S, Wojcik M. Structural order in Heusler compounds. In: Felser C, Hirohata A, editors. *Heusler Alloys*. Berlin, Germany: Springer; 2016. p. pp. 87–109.
- [229] Williams JM. Mössbauer effect in the Heusler alloy  $\text{Co}_2\text{MnSn}$ . *J Phys C*. 1968;1:473.
- [230] Brooks JS, Williams JM, Webster PJ. The nuclear magnetic moments of the Mössbauer isotopes  $^{57}\text{Fe}$  and  $^{119}\text{Sn}$ . *J Phys D: Appl Phys*. 1973;6:1403.
- [231] Yamada S, Hamaya K, Yamamoto K, et al. Significant growth-temperature dependence of ferromagnetic properties for  $\text{Co}_2\text{FeSi}/\text{Si}(111)$  prepared by low-temperature molecular beam epitaxy. *Appl Phys Lett*. 2010;96:082511.
- [232] Kasahara K, Yamamoto K, Yamada S, et al. Highly ordered  $\text{Co}_2\text{FeSi}$  Heusler alloys grown on  $\text{Ge}(111)$  by low-temperature molecular beam epitaxy. *J Appl Phys*. 2010;107:09B105.
- [233] Tanikawa K, Oki S, Yamada S, et al. Effect of Co-Fe substitution on room-temperature spin polarization in  $\text{Co}_{3-x}\text{Fe}_x\text{Si}$  Heusler-compound films. *Phys Rev B*. 2013;88:014402.
- [234] Tanaka MA, Maezaki D, Ishii T, et al. Interface magnetism of  $\text{Co}_2\text{FeGe}$  Heusler alloy layers and magnetoresistance of  $\text{Co}_2\text{FeGe}/\text{MgO}/\text{Fe}$  magnetic tunnel junctions. *J Appl Phys*. 2014;116:163902.
- [235] Nakatani N, Imai S, Tanaka MA, et al. Deposition temperature dependence of interface magnetism of  $\text{Co}_2\text{FeGe}$ -Heusler-alloy/ $\text{Ag}$  films studied with  $^{57}\text{Fe}$  Mössbauer spectroscopy. *J Magn Magn Mater*. 2018;464:71.
- [236] Mibu K, Tanaka MA, Hamaya K. Mössbauer analysis in Heusler alloys. In: Felser C, Hirohata A, editors. *Heusler Alloys*. Berlin, Germany: Springer; 2016. p. pp. 341–352.
- [237] Rashba EI. Theory of electrical spin injection: Tunnel contacts as a solution of the conductivity mismatch problem. *Phys Rev B*. 2000;62:R16267.
- [238] Datta S, Das B. Electronic analog of the electro-optic modulator. *Appl Phys Lett*. 1990;56:665.
- [239] Jedema FJ, Filip AT, van Wees BJ. Electrical spin injection and accumulation at room temperature in an all-metal mesoscopic spin valve. *Nature*. 2000;410:345.
- [240] Kimura T, Hashimoto N, Yamada S, et al. Room-temperature generation of giant pure spin currents using epitaxial  $\text{Co}_2\text{FeSi}$  spin injectors. *NPG Asia Mater*. 2012;4:e9.
- [241] Kokado S, Tsunoda M, Harigaya K, et al. Anisotropic Magnetoresistance Effects in Fe, Co, Ni,  $\text{Fe}_4\text{N}$ , and Half-Metallic Ferromagnet: A Systematic Analysis. *J Phys Soc Jpn*. 2012;81:024705.
- [242] Sakuraba Y, Kokado S, Hirayama Y, et al. Quantitative analysis of anisotropic magnetoresistance in  $\text{Co}_2\text{MnZ}$  and  $\text{Co}_2\text{FeZ}$  epitaxial thin films: A facile way to investigate spin-polarization in half-metallic Heusler compounds. *Appl Phys Lett*. 2014;104:172407.
- [243] Kwon B, Sakuraba Y, Sukegawa H, et al. Anisotropic magnetoresistance and current-perpendicular-to-plane giant magnetoresistance in epitaxial  $\text{NiMnSb}$ -based multilayers. *Jpn J Appl Phys*. 2016;119:023902.
- [244] Wen Z, Kubota T, Yamamoto T, et al. Fully epitaxial C1b-type  $\text{NiMnSb}$  half-Heusler alloy films for current-perpendicular-to-plane giant magnetoresistance devices with a  $\text{Ag}$  spacer. *Sci Rep*. 2015;5:18387.
- [245] Sato T, Kokado S, Tsujikawa M, et al. Signs of anisotropic magnetoresistance in  $\text{Co}_2\text{MnGa}$  Heusler alloy epitaxial thin films based on current direction. *Appl Phys Exp*. 2019;12:103005.
- [246] Bass J. CPP magnetoresistance of magnetic multilayers: A critical review. *J Magn Magn Mater*. 2016;408:244.
- [247] Caballero JA, Park YD, Childress JR. Magnetoresistance of  $\text{NiMnSb}$ -based multilayers and spin valves. *J Vac Sci Technol A*. 1998;16:1801.
- [248] Caballero JA, Reilly AC, Hao Y, et al. Effect of deposition parameters on the CPP-GMR of  $\text{NiMnSb}$ -based spin-valve structures. *J Magn Magn Mater*. 1999;198-199:55.
- [249] Wen Z, Kubota T, Yamamoto T, et al. Enhanced current-perpendicular-to-plane giant magnetoresistance effect in half-metallic  $\text{NiMnSb}$  based nanojunctions with multiple  $\text{Ag}$  spacers. *Appl Phys Lett*. 2016;108:232406.
- [250] Ambrose T, Krebs JJ, Prinz GA. Magnetotransport properties of single crystal  $\text{Co}_2\text{MnGe}/\text{NM}/\text{Co}_2\text{MnGe}$  trilayers epitaxially grown on  $\text{GaAs}(001)$ . *J Appl Phys*. 2001;89:7522.
- [251] Jogo A, Nagasaka K, Ibusuki T, et al. Current-perpendicular spin valves with high-resistivity ferromagnetic metals for ultrahigh-density magnetic recording. *J Magn Magn Mater*. 2007;309:80.
- [252] Maat S, Carey MJ, Childress JR. Magnetotransport properties and spin-torque effects in current perpendicular to the plane spin valves with  $\text{Fe}$  magnetic layers. *J Appl Phys*. 2007;101:093905.
- [253] Yakushiji K, Saito K, Mitani S, et al. Current-perpendicular-to-plane magnetoresistance in epitaxial  $\text{Co}_2\text{MnSi}/\text{Cr}/\text{Co}_2\text{MnSi}$  trilayers. *Appl Phys Lett*. 2006;88:222504.
- [254] Kodama K, Furubayashi T, Sukegawa H, et al. Current-perpendicular-to-plane giant magnetoresistance of a spin valve using  $\text{Co}_2\text{MnSi}$  Heusler alloy electrodes. *J Appl Phys*. 2009;105:07E905.
- [255] Furubayashi T, Kodama K, Sukegawa H, et al. Current-perpendicular-to-plane giant magnetoresistance in spin-valve structures using epitaxial  $\text{Co}_2\text{FeAl}_{0.5}\text{Si}_{0.5}/\text{Ag}/\text{Co}_2\text{FeAl}_{0.5}\text{Si}_{0.5}$  trilayers. *Appl Phys Lett*. 2008;93:122507.
- [256] Iwase T, Sakuraba Y, Bosu S, et al. Large Interface Spin-Asymmetry and Magnetoresistance in Fully Epitaxial  $\text{Co}_2\text{MnSi}/\text{Ag}/\text{Co}_2\text{MnSi}$  Current-Perpendicular-to-Plane Magnetoresistive Devices. *Appl Phys Exp*. 2009;2:063003.
- [257] Nakatani TM, Furubayashi T, Kasai S, et al. Bulk and interfacial scatterings in current-perpendicular-to-plane giant magnetoresistance with  $\text{Co}_2\text{Fe}(\text{Al}_{0.5}\text{Si}_{0.5})$  Heusler alloy layers and  $\text{Ag}$  spacer. *Appl Phys Lett*. 2010;96:212501.
- [258] Takahashi YK, Srinivasan A, Varaprasad B, et al. Bulk and interfacial scatterings in current-perpendicular-to-plane giant magnetoresistance with  $\text{Co}_2\text{Fe}(\text{Al}_{0.5}\text{Si}_{0.5})$  Heusler alloy layers and  $\text{Ag}$  spacer. *Appl Phys Lett*. 2011;98:152501.
- [259] Du Y, Furubayashi T, Sasaki TT, et al. Large magnetoresistance in current-perpendicular-to-plane pseudo spin-valves using  $\text{Co}_2\text{Fe}(\text{Ga}_{0.5}\text{Ge}_{0.5})$  Heusler alloy and  $\text{AgZn}$  spacer. *Appl Phys Lett*. 2015;107:112405.
- [260] Li Y, Xia J, Wang G, et al. High-performance giant-magnetoresistance junction with B2-disordered Heusler alloy based  $\text{Co}_2\text{MnAl}/\text{Ag}/\text{Co}_2\text{MnAl}$  trilayer. *J Appl Phys*. 2015;118:053902.
- [261] Sato J, Oogane M, Naganuma H, et al. Large Magnetoresistance Effect in Epitaxial  $\text{Co}_2\text{Fe}_{0.4}\text{Mn}_{0.6}\text{Si}$

- Ag/Co<sub>2</sub>Fe<sub>0.4</sub>Mn<sub>0.6</sub>Si Devices. Appl Phys Exp. 2011;4:113005.
- [262] Sakuraba Y, Ueda M, Miura Y, et al. Large Magnetoresistance Effect in Epitaxial Co<sub>2</sub>Fe<sub>0.4</sub>Mn<sub>0.6</sub>Si/Ag/Co<sub>2</sub>Fe<sub>0.4</sub>Mn<sub>0.6</sub>Si Devices. Appl Phys Lett. 2012;101:252408.
- [263] Jung JW, Sakuraba Y, Sasaki TT, et al. Enhancement of magnetoresistance by inserting thin NiAl layers at the interfaces in Co<sub>2</sub>FeGa<sub>0.5</sub>Ge<sub>0.5</sub>/Ag/Co<sub>2</sub>FeGa<sub>0.5</sub>Ge<sub>0.5</sub> current-perpendicular-to-plane pseudo spin valves. Appl Phys Lett. 2016;108:102408.
- [264] Kubota T, Ina Y, Wen Z, et al. Current perpendicular-to-plane giant magnetoresistance using an L 1 2 Ag 3 Mg spacer and Co<sub>2</sub>Fe<sub>0.4</sub>Mn<sub>0.6</sub>Si Heusler alloy electrodes: Spacer thickness and annealing temperature dependence. Phys Rev Mater. 2017;1:044402.
- [265] Kubota T, Wen Z, Takanashi K. Current-perpendicular-to-plane giant magnetoresistance effects using Heusler alloys. J Magn Magn Mater. 2019;492:165667.
- [266] Fukuzawa H, Koi K, Tomita H, et al. NOL specular spin-valve heads using an ultrathin CoFe free layer. J Magn Magn Mater. 2001;235:208.
- [267] Nakatani T, Li S, Sakuraba Y, et al. Advanced CPP-GMR Spin-Valve Sensors for Narrow Reader Applications. IEEE Trans Magn. 2018;54:3300211.
- [268] Manchon A, Ducruet C, Lombard L, et al. Analysis of oxygen induced anisotropy crossover in Pt/Co/MOX trilayers. J Appl Phys. 2008;104:043914.
- [269] Koo JW, Mitani S, Sasaki TT, et al. Large perpendicular magnetic anisotropy at Fe/MgO interface. Appl Phys Lett. 2013;103:192401.
- [270] Mizukami S, Sakuma A, Sugihara A, et al. Mn-based hard magnets with small saturation magnetization and low spin relaxation for spintronics. Scr Mater. 2016;118:70.
- [271] Frost W, Hirohata A. Perpendicular Anisotropy in Heusler Alloy Layers Induced by a V Seed Layer. IEEE Trans Magn. 2016;52:4400604.
- [272] Mizukami S, Wu F, Sakuma A, et al. Long-Lived Ultrafast Spin Precession in Manganese Alloys Films with a Large Perpendicular Magnetic Anisotropy. Phys Rev Lett. 2011;106:117201.
- [273] Wu F, Mizukami S, Watanabe D, et al. Epitaxial Mn<sub>2.5</sub>Ga thin films with giant perpendicular magnetic anisotropy for spintronic devices. Appl Phys Lett. 2009;94:122503.
- [274] Wen Z, Sukegawa H, Mitani S, et al. Perpendicular magnetization of Co<sub>2</sub>FeAl full-Heusler alloy films induced by MgO interface. Appl Phys Lett. 2011;98:242507.
- [275] Wen Z, Sukegawa H, Kasai S, et al. Magnetic Tunnel Junctions with Perpendicular Anisotropy Using a Co<sub>2</sub>FeAl Full-Heusler Alloy. Appl Phys Exp. 2012;5:063003.
- [276] Cui Y, Khodadadi B, Schäfer S, et al. Interfacial perpendicular magnetic anisotropy and damping parameter in ultra thin Co<sub>2</sub>FeAl films. Appl Phys Lett. 2013;102:162403.
- [277] Sukegawa H, Paul Hadorn J, Wen Z, et al. Perpendicular magnetic anisotropy at lattice-matched Co<sub>2</sub>FeAl/MgAl<sub>2</sub>O<sub>4</sub>(001) epitaxial interfaces. Appl Phys Lett. 2017;110:112403.
- [278] Frost W, Hirohata A. Heusler alloys with bcc tungsten seed layers for GMR junctions. J Magn Magn Mater. 2018;453:182.
- [279] Hirohata A, Frost W, Samiepour M, et al. Perpendicular Magnetic Anisotropy in Heusler Alloy Films and Their Magnetoresistive Junctions. Mater. 2018;11:105.
- [280] Serway RA. Principles of Physics. 2nd ed. Brooks Cole: Fort Worth, TX, USA;1997. 602.
- [281] Jung WD, Schmidt FA, Danielson GC. Thermal conductivity of high-purity vanadium. Phys Rev B. 1977;15:659.
- [282] Marukame T, Yamamoto M. Tunnel magnetoresistance in fully epitaxial magnetic tunnel junctions with a full-Heusler alloy thin film of Co<sub>2</sub>Cr<sub>0.6</sub>Fe<sub>0.4</sub>Al and a MgO tunnel barrier. J Appl Phys. 2007;101:083906.
- [283] Wang W, Sukegawa H, Shan R, et al. Giant tunneling magnetoresistance up to 330% at room temperature in sputter deposited Co<sub>2</sub>FeAl/MgO/CoFe magnetic tunnel junctions. Appl Phys Lett. 2009;95:182502.
- [284] Scheike T, Sukegawa H, Inomata K, et al. Chemical ordering and large tunnel magnetoresistance in Co<sub>2</sub>FeAl/MgAl<sub>2</sub>O<sub>4</sub>/Co<sub>2</sub>FeAl(001) junctions. Appl Phys Exp. 2016;9:053004.
- [285] Wang W, Sukegawa H, Shan R, et al. Large tunnel magnetoresistance in Co<sub>2</sub>FeAl<sub>0.5</sub>Si<sub>0.5</sub>/MgO/Co<sub>2</sub>FeAl<sub>0.5</sub>Si<sub>0.5</sub> magnetic tunnel junctions prepared on thermally oxidized Si substrates with MgO buffer. Appl Phys Lett. 2008;93:182504.
- [286] Wen Z, Sukegawa H, Kasai S, et al. Tunnel Magnetoresistance and Spin-Transfer-Torque Switching in Polycrystalline Co<sub>2</sub>FeAl Full-Heusler-Alloy Magnetic Tunnel Junctions on Amorphous Si/SiO<sub>2</sub> Substrates. Phys Rev Appl. 2014;2:024009.
- [287] Tezuka N, Ikeda N, Sugimoto S, et al. 175% tunnel magnetoresistance at room temperature and high thermal stability using Co<sub>2</sub>FeAl<sub>0.5</sub>Si<sub>0.5</sub> full-Heusler alloy electrodes. Appl Phys Lett. 2006;89:252508.
- [288] Tezuka N, Ikeda N, Mitsunashi F, et al. Improved tunnel magnetoresistance of magnetic tunnel junctions with Heusler Co<sub>2</sub>FeAl<sub>0.5</sub>Si<sub>0.5</sub> electrodes fabricated by molecular beam epitaxy. Appl Phys Lett. 2009;94:162504.
- [289] Hirohata A, Otani Y. Heusler alloys: experimental approach towards room-temperature half-metallicity. In: Hirohata A, Otani Y, editors. Epitaxial Ferromagnetic Films and Spintronic Applications. Kerala, India: Research Signpost; 2009. p. 224–225.
- [290] Hakamata S, Ishikawa T, Marukame T, et al. Improved tunnel magnetoresistance characteristics of magnetic tunnel junctions with a Heusler alloy thin film of Co<sub>2</sub>MnGe and a MgO tunnel barrier. J Appl Phys. 2007;101:09J513.
- [291] Marukame T, Kasahara T, Hakamata S, et al. Highly spin-polarized tunneling in fully epitaxial Co<sub>2</sub>Cr<sub>0.6</sub>Fe<sub>0.4</sub>Al/MgO/Co<sub>50</sub>Fe<sub>50</sub> magnetic tunnel junctions with exchange biasing. Appl Phys Lett. 2007;90:012508.
- [292] Tsunegi S, Sakuraba Y, Oogane M, et al. Large tunnel magnetoresistance in tunnel junctions with Co<sub>2</sub>MnSi/Co<sub>2</sub>FeSi multilayer electrode. Appl Phys Lett. 2008;93:112506.
- [293] Hu B, Moges K, Honda Y, et al. Temperature dependence of spin-dependent tunneling conductance of magnetic tunnel junctions with half-metallic Co<sub>2</sub>MnSi electrodes. Phys Rev B. 2016;94:094428.
- [294] Mavropoulos P, Ležaić M, Blügel S. Half-metallic ferromagnets for magnetic tunnel junctions by *ab initio* calculations. Phys Rev B. 2005;72:174428.

- [295] Ležaić M, Mavropoulos P, Enkovaara J, et al. Thermal Collapse of Spin Polarization in Half-Metallic Ferromagnets. *Phys Rev Lett.* **2006**;97:026404.
- [296] Sakuma A, Toga Y, Tsuchiura H. Theoretical study on the stability of magnetic structures in the surface and interfaces of Heusler alloys, Co<sub>2</sub>MnAl and Co<sub>2</sub>MnSi. *J Appl Phys.* **2009**;105:07C910.
- [297] Miura Y, Abe K, Shirai M. Effects of interfacial noncollinear magnetic structures on spin-dependent conductance in Co<sub>2</sub>MnSi/MgO/Co<sub>2</sub>MnSi magnetic tunnel junctions: A first-principles study. *Phys Rev B.* **2011**;83:214411.
- [298] Sukegawa H, Wang W, Shan R, et al. Spin-polarized tunneling spectroscopy of fully epitaxial magnetic tunnel junctions using Co<sub>2</sub>FeAl<sub>0.5</sub>Si<sub>0.5</sub> Heusler alloy electrodes. *Phys Rev B.* **2009**;79:184418.
- [299] Tsunegi S, Sakuraba Y, Oogane M, et al. Enhancement in tunnel magnetoresistance effect by inserting CoFeB to the tunneling barrier interface in Co<sub>2</sub>MnSi/MgO/CoFe magnetic tunnel junctions. *Appl Phys Lett.* **2009**;94:252503.
- [300] Scheike T, Sukegawa H, Furubayashi T, et al. Lattice-matched magnetic tunnel junctions using a Heusler alloy Co<sub>2</sub>FeAl and a cation-disorder spinel Mg-Al-O barrier. *Appl Phys Lett.* **2014**;105:242407.
- [301] Ishikawa T, Liu H, Taira T, et al. Influence of film composition in Co<sub>2</sub>MnSi/Co<sub>2</sub>MnSi electrodes on tunnel magnetoresistance characteristics of Co<sub>2</sub>MnSi/MgO/Co<sub>2</sub>MnSi magnetic tunnel junctions. *Appl Phys Lett.* **2009**;95:232512.
- [302] Liu H, Honda Y, Taira T, et al. Giant tunneling magnetoresistance in epitaxial Co<sub>2</sub>MnSi/MgO/Co<sub>2</sub>MnSi magnetic tunnel junctions by half-metallicity of Co<sub>2</sub>MnSi and coherent tunneling. *Appl Phys Lett.* **2012**;101:132418.
- [303] Hu B, Moges K, Honda Y, et al. Temperature dependence of spin-dependent tunneling conductance of magnetic tunnel junctions with half-metallic Co<sub>2</sub>MnSi electrodes. *Phys Rev B.* **2012**;94:094428.
- [304] Liu H, Kawami T, Moges K, et al. Influence of film composition in quaternary Heusler alloy Co<sub>2</sub>(Mn,Fe)Si thin films on tunnelling magnetoresistance of Co<sub>2</sub>(Mn,Fe)Si/MgO-based magnetic tunnel junctions. *J Phys D Appl Phys.* **2015**;48:164001.
- [305] Yamamoto M, Ishikawa T, Taira T, et al. Effect of defects in Heusler alloy thin films on spin-dependent tunnelling characteristics of Co<sub>2</sub>MnSi/MgO/Co<sub>2</sub>MnSi and Co<sub>2</sub>MnGe/MgO/Co<sub>2</sub>MnGe magnetic tunnel junctions. *J Phys Condens Matter.* **2010**;22:164212.
- [306] Bainsla L, Suzuki KZ, Tsujikawa M, et al. Magnetic tunnel junctions with an equiatomic quaternary CoFeMnSi Heusler alloy electrode. *Appl Phys Lett.* **2018**;112:052403.
- [307] Kasai S, Takahashi YK, Cheng P-H, et al. Large magnetoresistance in Heusler-alloy-based epitaxial magnetic junctions with semiconducting Cu(In<sub>0.8</sub>Ga<sub>0.2</sub>)Se<sub>2</sub> spacer. *Appl Phys Lett.* **2016**;109:032409.
- [308] Mukaiyama K, Jung JW, Sepehri-Amin H, et al. Over 100% magnetoresistance ratio at room temperature in magnetic tunnel junctions with CuGaSe<sub>2</sub> spacer layer. *Appl Phys Lett.* **2019**;114:172402.
- [309] Bang H-W, Yoo W, Choi Y, et al. Perpendicular magnetic anisotropy properties of tetragonal Mn<sub>3</sub>Ga films under various deposition conditions. *Curr Appl Phys.* **2016**;16:63.
- [310] Winterlik J, Balke B, Fecher GH, et al. Structural, electronic, and magnetic properties of tetragonal Mn<sub>3-x</sub>Ga: Experiments and first-principles calculations. *Phys Rev B.* **2008**;77:054406.
- [311] Kubota T, Miura Y, Watanabe D, et al. Magnetoresistance Effect in Tunnel Junctions with Perpendicularly Magnetized D022-Mn<sub>3-δ</sub>Ga Electrode and MgO Barrier. *Appl Phys Exp.* **2011**;4:043002.
- [312] Kurt H, Coey JMD. Magnetic and electronic properties of thin films of Mn-Ga and Mn-Ge compounds with cubic, tetragonal and hexagonal crystal structures. In: Felser C, Hirohata A, editors. *Heusler Alloys*. Berlin, Germany: Springer; **2016**. p. pp. 3–36.
- [313] Ma QL, Kubota T, Mizukami S, et al. Magnetoresistance effect in L10-MnGa/MgO/CoFeB perpendicular magnetic tunnel junctions with Co interlayer. *Appl Phys Lett.* **2012**;101:032402.
- [314] Suzuki KZ, Ranjbar R, Okabayashi J, et al. Perpendicular magnetic tunnel junction with a strained Mn-based nanolayer. *Sci Rep.* **2016**;6:30249.
- [315] Jeong J, Ferrante Y, Faleev SV, et al. Termination layer compensated tunnelling magnetoresistance in ferrimagnetic Heusler compounds with high perpendicular magnetic anisotropy. *Nat Commun.* **2016**;7:10276.
- [316] Mao S, Lu J, Zhao X, et al. MnGa-based fully perpendicular magnetic tunnel junctions with ultrathin Co<sub>2</sub>MnSi interlayers. *Sci Rep.* **2017**;7:43064.
- [317] Wen Z, Sukegawa H, Furubayashi T, et al. A 4-Fold-Symmetry Hexagonal Ruthenium for Magnetic Heterostructures Exhibiting Enhanced Perpendicular Magnetic Anisotropy and Tunnel Magnetoresistance. *Adv. Mater.* **2014**;26:6483.
- [318] Sukegawa H, Xiu H, Ohkubo T, et al. Tunnel magnetoresistance with improved bias voltage dependence in lattice-matched Fe/spinel MgAl<sub>2</sub>O<sub>4</sub>/Fe(001) junctions. *Appl Phys Lett.* **2010**;96:212505.
- [319] Sukegawa H, Kato Y, Belmoubarik M, et al. MgGa<sub>2</sub>O<sub>4</sub> spinel barrier for magnetic tunnel junctions: Coherent tunneling and low barrier height. *Appl Phys Lett.* **2017**;110:122404.
- [320] Hadorn JP, Sukegawa H, Ohkubo T, et al. Microstructural evolution of perpendicular magnetization films with an ultra-thin Co<sub>2</sub>FeAl/MgAl<sub>2</sub>O<sub>4</sub>(001) structure. *Acta Mater.* **2018**;145:306.
- [321] Hiratsuka T, Kim G, Sakuraba Y, et al. Fabrication of perpendicularly magnetized magnetic tunnel junctions with L10-CoPt/Co<sub>2</sub>MnSi hybrid electrode. *J Appl Phys.* **2010**;107:09C714.
- [322] Jungwirth T, Marti X, Wadley P, et al. Antiferromagnetic spintronics. *Nat Nanotech.* **2016**;11:231.
- [323] Hirohata A, Huminiuc T, Sinclair J, et al. Development of antiferromagnetic Heusler alloys for the replacement of iridium as a critically raw material. *J Phys D Appl Phys.* **2017**;50:443001.
- [324] Endo K. Magnetic Studies of Clb-Compounds CuMnSb, PdMnSb and Cu<sub>1-x</sub>(Ni or Pd)<sub>x</sub>MnSb. *J Phys Soc Jpn.* **1970**;29:643.
- [325] Müller RA, Desilets-Benoit A, Gauthier N, et al. Magnetic structure of the antiferromagnetic half-Heusler compound NdBiPt. *Phys Rev B.* **2015**;92:184432.

- [326] Jesus CBR, Rosa PFS, Garitezi TM, et al. Electron spin resonance of the half-Heusler antiferromagnet GdPdBi. *Solid State Commun.* **2014**;177:95.
- [327] Singh S, D'Souza SW, Nayak J, et al. Room-temperature tetragonal non-collinear Heusler antiferromagnet Pt<sub>2</sub>MnGa. *Nat Commun.* **2016**;7:12671.
- [328] Mizusaki S, Douzono A, Ohnishi T, et al. Effect of Fe substitution on magnetic properties of antiferromagnetic Heusler alloy Ru<sub>2</sub>MnGe. *J Alloys Comp.* **2012**;510:141.
- [329] Balluff J, Meinert M, Schmalhorst J-M, et al. Exchange bias in epitaxial and polycrystalline thin film Ru<sub>2</sub>MnGe/Fe bilayers. *J Appl Phys.* **2016**;118:243907.
- [330] Khmelevskiy S, Simon E, Szunyogh L. Antiferromagnetism in Ru<sub>2</sub>MnZ (Z=Sn,Sb,Ge,Si) full Heusler alloys: Effects of magnetic frustration and chemical disorder. *Phys Rev B.* **2015**;91:094432.
- [331] Acet M, Duman E, Wassermann EF. Coexisting ferro- and antiferromagnetism in Ni<sub>2</sub>MnAl Heusler alloys. *J Appl Phys.* **2002**;92:3867.
- [332] Galanakis I, Şaşıoğlu E. Structural-induced antiferromagnetism in Mn-based full Heusler alloys: The case of Ni<sub>2</sub>MnAl. *Appl Phys Lett.* **2011**;98:102514.
- [333] Yanes Díaz R, Simon E, Szunyogh L, et al. private communications.
- [334] Tsuchiya T, Kobayashi R, Kubota T, et al. Mn<sub>2</sub>VAl Heusler alloy thin films: appearance of antiferromagnetism and exchange bias in a layered structure with Fe. *J Phys D Appl Phys.* **2018**;51:065001.
- [335] Tsuchiya T, Kubota T, Sugiyama T, et al. Exchange bias effects in Heusler alloy Ni<sub>2</sub>MnAl/Fe bilayers. *J Phys D Appl Phys.* **2016**;49:235001.
- [336] Wu H, Vallejo-Fernandez G, Hirohata A. Growth and characterisation of ferromagnetic and antiferromagnetic Fe V Al Heusler alloy films. *J Phys D Appl Phys.* **2017**;50:375001.
- [337] Krén E, Kádár G. Neutron diffraction study of Mn<sub>3</sub>Ge. *Solid State Commun.* **1970**;8:1653.
- [338] Kurt H, Rode K, Tokuc H, et al. Exchange-biased magnetic tunnel junctions with antiferromagnetic  $\epsilon$ -Mn<sub>3</sub>Ge. *Appl Phys Lett.* **2012**;101:232402.
- [339] Wu H, Sudoh I, Xu R, et al. Large exchange bias induced by polycrystalline Mn<sub>3</sub>Ge antiferromagnetic films with controlled layer thickness. *J Phys D: Appl Phys.* **2018**;51:215003.
- [340] Kadar G, Kren E. Neutron diffraction study of Mn<sub>3</sub>Ge. *Int J Magn.* **1971**;1:143.
- [341] Quian JF, Nayak AK, Kreiner G, et al. Exchange bias up to room temperature in antiferromagnetic hexagonal Mn<sub>3</sub>Ge. *J Phys D Appl Phys.* **2014**;47:305001.
- [342] Ogasawara T, Kim J-Y, Ando Y, et al. Structural and antiferromagnetic characterization of noncollinear D019 Mn<sub>3</sub>Ge polycrystalline film. *J Magn Magn Mater.* **2019**;473:7.
- [343] Nayak AK, Nicklas M, Chadov S, et al. Design of compensated ferrimagnetic Heusler alloys for giant tunable exchange bias. *Nat Mater.* **2015**;14:679.
- [344] Ogasawara T, Tsunoda M, Ando Y, et al. In-plane and perpendicular exchange bias effect induced by an antiferromagnetic D019 Mn<sub>2</sub>FeGa thin film. *J Magn Magn Mater.* **2019**;484:307.
- [345] Meinert M, Bükér B, Graulich D, et al. Large exchange bias in polycrystalline MnN/CoFe bilayers at room temperature. *Phys Rev B.* **2015**;92:144408.
- [346] Singh DJ, Mazin I. Electronic structure, local moments, and transport in Fe<sub>2</sub>VAl. *Phys Rev B.* **1998**;57:14352.
- [347] Huminiuc T, Whear O, Takahashi T, et al. Growth and characterisation of ferromagnetic and antiferromagnetic Fe<sub>2+x</sub>V<sub>y</sub>Al Heusler alloy films. *J Phys D Appl Phys.* **2018**;51:325003.
- [348] Chen JY, Thiyagarajah N, Xu HJ, et al. Perpendicular exchange bias effect in sputter-deposited CoFe/IrMn bilayers. *Appl Phys Lett.* **2014**;104:152405.
- [349] O'Grady K, Fernandez-Outon LE, Vallejo Fernandez G. A new paradigm for exchange bias in polycrystalline thin films. *J Magn Magn Mater.* **2010**;322:883.
- [350] Yanes Díaz R, Jackson J, Udvardi L, et al. Exchange Bias Driven by Dzyaloshinskii-Moriya Interactions. *Phys Rev Lett.* **2013**;111:217202.
- [351] Yanes Díaz R, Simon E, Keller S, et al. Interfacial exchange interactions and magnetism of Ni<sub>2</sub>MnAl/Fe bilayer. *Phys Rev B.* **2017**;96:064435.
- [352] Fukamichi K. *Antiferromagnets.* Tokyo: Kyoritsu; **2014**.
- [353] Kinoshita T, Wakita T, Sun H-L, et al. Antiferromagnetic Domain Structure Imaging of Cleaved NiO(100) Surface Using Nonmagnetic Linear Dichroism at O K Edge: Essential Effect of Antiferromagnetic Crystal Distortion. *J Phys Soc Jpn.* **2004**;73:2932.
- [354] Bland JAC, Heinrich B, *Eds.* Large exchange bias induced by polycrystalline Mn<sub>3</sub>Ge antiferromagnetic films with controlled layer thickness. *Ultrathin Magnetic Structures I.* Berlin: Springer; **1994**. p. pp. 305–343.
- [355] Nayak AK, Kumar V, Ma T, et al. Magnetic antiskyrmions above room temperature in tetragonal Heusler materials. *Nature.* **2017**;548:561.
- [356] Nikolaev K, Kolbo P, Pokhil T, et al. "All-Heusler alloy" current-perpendicular-to-plane giant magnetoresistance. *Appl Phys Lett.* **2009**;94:222501.
- [357] van Leuken H, de Groot R. Half-Metallic Antiferromagnets. *Phys Rev Lett.* **1995**;74:1171.
- [358] Gao G, Yao K. Antiferromagnetic half-metals, gapless half-metals, and spin gapless semiconductors: The D03-type Heusler alloys. *Appl Phys Lett.* **2013**;103:232409.
- [359] Li J, Liu H, Zhang Z, et al. Obtaining half-metallic ferrimagnetism and antiferromagnetism by doping Mn and Fe for D03-type Heusler compound Cr<sub>3</sub>Si. *J Alloys Compd.* **2014**;597:8.
- [360] Blatz V, Manchon A, Tsoi M, et al. Antiferromagnetic spintronics. *Rev Mod Phys.* **2018**;90:015005.
- [361] Jungwirth T, Sinova J, Marti X, et al. The multiple directions of antiferromagnetic spintronics. *Nat Phys.* **2018**;14:200.
- [362] Sahoo R, Wollmann L, Selle S, et al. Compensated Ferrimagnetic Tetragonal Heusler Thin Films for Antiferromagnetic Spintronics. *Adv Mater.* **2016**;28:8499.
- [363] Qi X-L, Zhang S-C. Topological insulators and superconductors. *Rev Mod Phys.* **2011**;83:1057.
- [364] Qi Y, Shi W, Werner P, et al. Pressure-induced superconductivity and topological quantum phase transitions in a quasi-one-dimensional topological insulator: Bi<sub>4</sub>I<sub>4</sub>NPG. *Quantum Mat.* **2018**;3:1.
- [365] Liu ZK, Yang LX, Wu S-C, et al. Observation of unusual topological surface states in half-Heusler compounds LnPtBi (Ln=Lu, Y). *Nat Commun.* **2016**;7:12924.
- [366] Zhang M, Wei J, Wang G. Thermoelectric and topological properties of half-Heusler compounds ZrIrX (As, Sb, Bi). *Phys Lett A.* **2018**;382:673.
- [367] Barman CK, Alam A. Topological phase transition in the ternary half-Heusler alloy ZrIrBi. *Phys Rev B.* **2018**;97:075302.

- [368] Chen J, Li H, Ding B, et al. Structural and magneto-transport properties of topological trivial LuNiBi single crystals. *J Alloy Compd.* **2019**;784:822.
- [369] Wang XL. Proposal for a New Class of Materials: Spin Gapless Semiconductors. *Phys Rev Lett.* **2008**;100:156404.
- [370] Du Y, Xu GZ, Zhang XM, et al. Crossover of magnetoresistance in the zero-gap half-metallic Heusler alloy Fe<sub>2</sub>CoSi. *Europhys Lett.* **2013**;103:37011.
- [371] Ouardi S, Fecher GH, Felser C, et al. Realization of Spin Gapless Semiconductors: The Heusler Compound Mn<sub>2</sub>CoAl. *Phys Rev Lett.* **2013**;110:100401.
- [372] Galanakis I, Özdoğan K, Şaşıoğlu E. Spin-filter and spin-gapless semiconductors: The case of Heusler compounds. *AIP Adv.* **2016**;6:055606.
- [373] Bainsla L, Mallick AI, Raja MM, et al. Origin of spin gapless semiconductor behavior in CoFeCrGa: Theory and Experiment. *Phys Rev B.* **2015**;92:045201.
- [374] Patel PD, Shinde S, Gupta SD, et al. The first principle calculation of structural, electronic, magnetic, elastic, thermal and lattice dynamical properties of fully compensated ferrimagnetic spin-gapless heusler alloy Zr<sub>2</sub>MnGa. *Comput Condens Matter.* **2018**;15:61.
- [375] Guo X, Ni Z, Liang Z, et al. Magnetic semiconductors and half-metals in FeRu-based quaternary Heusler alloys. *Comput Mater Sci.* **2018**;154:442.
- [376] Fan L, Chen F, Li C, et al. Promising spintronics: Mn-based Heusler alloys Mn<sub>3</sub>Ga, Mn<sub>2</sub>YGa (Y = V, Nb, Ta), ScMnVGa. *J Magn Magn Mater.* **2020**;497:166060.
- [377] Birsan A, Kuncser V. First principle investigations of the structural, electronic and magnetic properties of predicted new zirconium based full-Heusler compounds, Zr<sub>2</sub>MnZ (Z=Al, Ga and In). *J Magn Magn Mater.* **2016**;406:282.
- [378] Xu XD, Chen ZX, Sakuraba Y, et al. Microstructure, magnetic and transport properties of a Mn<sub>2</sub>CoAl Heusler compound. *Acta Mater.* **2019**;176:33.
- [379] Bainsla L, Mallick AI, Manivel Raja M, B. S., D. C. S. Varaprasad, Y. K. Takahashi, A. Alam, K. G. Suresh and K. Hono. et al. Spin gapless semiconducting behavior in equiatomic quaternary CoFeMnSi Heusler alloy. *Phys Rev B.* **2015**;91:104408.
- [380] Fu H, Li Y, Ma L, et al. Structures, magnetism and transport properties of the potential spin-gapless semiconductor CoFeMnSi alloy. *J Magn Magn Mater.* **2019**;473:16.
- [381] Bhatt H, Mukadam MD, Meena SS, et al. Fe<sub>2-x</sub>CoxMnSi (x = 0, 1 and 2) Heusler alloys: Structural, magnetic and atomic site disorder properties. *AIP Conf Proc.* **2015**;1665:130048.
- [382] Tsuchiya T, Roy T, Elphick K, et al. Magnetic tunnel junctions with a B<sub>2</sub>-ordered CoFeCrAl equiatomic Heusler alloy. *Phys Rev Mater.* **2019**;3:084403.
- [383] <http://heusleralloys.mint.ua.edu>.
- [384] Sanvito S, Oses C, Xue J, et al. *Sci Adv.* **2017**;3:e1602241.